Tuning the Electronic Properties of Nanoscale Semiconductors

by

Andrew Copple

A Dissertation Presented in Partial Fulfillment
of the Requirements for the Degree
Doctor of Philosophy

Approved July 2016 by the
Graduate Supervisory Committee:

Xihong Peng, Chair
Candace Chan
Andrew Chizmeshya
Fernando Ponce

ARIZONA STATE UNIVERSITY

August 2016

ABSTRACT

Nanoscale semiconductors with their unique properties and potential applications

have been a focus of extensive research in recent years. There are many ways in which

semiconductors change the world with computers, cell phones, and solar panels, and

nanoscale semiconductors having a promising potential to expand the efficiency, reduce

the cost, and improve the flexibility and durability of their design. In this study,

theoretical quantum mechanical simulations were performed on several different

nanoscale semiconductor materials, including graphene/phosphorene nanoribbons and

group III-V nanowires. First principles density functional theory (DFT) was used to study

the electronic and structural properties of these nanomaterials in their fully relaxed and

strained states. The electronic band gap, effective masses of charge carriers, electronic

orbitals, and density of states were most commonly examined with strain, both from

intrinsic and external sources. For example, armchair graphene nanoribbons (AGNR)

were found to have unprecedented band gap-strain dependence. Phosphorene

nanoribbons (PNRs) demonstrate a different behavior, including a chemical scissors

effect, and studies revealed a strong relationship between passivation species and band

gap tunability. Unlike the super mechanical flexibility of AGNRs and PNRs which can

sustain incredible strain, modest yet large strain was applied to group III-V nanowires

such as GaAs/InAs. The calculations showed that a direct and indirect band gap transition

occurs at some critical strains and the origination of these gap transitions were explored

in detail. In addition to the pure nanowires, GaAs/InAs core/shell heterostructure

nanowires were also studied. Due to the lattice mismatch between GaAs and InAs, the

intrinsic strain in the core/shell nanowires demonstrates an interesting behavior on tuning

the electronic properties. This interesting behavior suggests a mechanical way to exert compressive strain on nanowires experimentally, and can create a finite quantum confinement effect on the core.

DEDICATION

This work is dedicated to the loving family and friends who have seen me through these difficult years of research and teaching. I am also thankful to God for the strength that He has given me through this greatest challenge I have yet experienced in life, and would like to dedicate this also to the Father through whom this was possible.

ACKNOWLEDGMENTS

TABLE OF CONTENTS

LIST OF TABLES

LIST OF FIGURES

Chapter I. INTRODUCTION
A. Motivation

Electronic devices, such as computers, solar cells, cell phones, light emitting diodes

(LEDs), and many other devices in the modern world rely on the newest technology

available in semiconductors.[1-5] As demand for faster, smaller, and more efficient devices

increases, the interest in nanoscale semiconductors rises, creating a vast field of research

on this particular subset of condensed matter physics.[5, 6] A principle goal of this field is to

find materials that allow for devices with smaller size, faster processing speed, greater

efficiency, longer lifespan and lower cost. In an attempt to achieve this goal, numerous

researchers in the field produce experimental and theoretical research on semiconductors.

This study focuses on semiconductor research, through theoretical calculations, to

explore these novel materials and seek out applications in nanoelectronics and renewable

energies, as well as to gain a fundamental understanding of the materials' properties at

the atomic level. This work utilizes an *ab initio* quantum mechanical approach to

theoretical calculations.

The *ab initio* quantum mechanical approach used in all calculations in this study is

performed using density functional theory (DFT). The motivation behind the theoretical

density functional theory simulations of semiconductors is an efficient predictive

calculation of favorable electronic properties for technological manipulation within

devices. DFT simulations are far less expensive than other first principles methods such

as the ones based on electron wavefunctions,[7] both of which are significantly cheaper

than experimentation, especially in regards to predicting and manipulating properties of

semiconductors in nanoscale. The study of both structural and electronic properties of semiconductors benefits the technological demands of this era.

There are many approaches to simulating semiconductor materials with the current knowledge of condensed matter. Molecular dynamics, statistical mechanics, and DFT are all approaches with different advantages and disadvantages, typically trading accuracy for computing costs. Even within DFT, there are multiple options on approximations and solution methods that change how the problem is solved, how expensive the simulation is, and what materials are best studied with a certain approach. For example, localized orbital approach is more appropriate for molecular, non-repeating studies, while periodic boundary condition plane-wave methods are more appropriate for crystals without defects or doping. And the GW approximation (Green's function with screened Coulomb interaction) is a great example of great accuracy in the band gap with huge computational cost, forcing limitations that significantly reduce the maximum size of the unit cell. This study focuses on a DFT approach with periodic boundary conditions and pseudopotentials, which allows for reasonable (about 300 atoms) unit cell size for reduced dimensionality structures.

The specific properties of semiconductors studied in this work include band gap tunability, predictions of new nanostructure configurations, effective masses of charge carriers including electrons and holes, density of states (DOS), band structure, and the work function of nanostructure semiconductors. These properties are essential for engineering the next improvements to solar cells, LEDs, lasers, and other device applications. An additional goal of this research is to help explain phenomena observed by experimental research into nanoscale semiconductors, after the materials have already

been synthesized.[5] Unlike with traditional simulations which focus on materials of the future, this work focuses on specifically matching structural and electrical properties of specific samples from experimental groups to help explain the data found by these groups. There are many amazing, unique features of nanoscale semiconductors, including their incredible strain capacity, their unique structural stability, and the more prominent observable quantum confinement effect in their smaller structures. The high strain capacity of graphene,[8] the lowering of formation energy for wurtzite GaAs in nanowires,[9] and the band gap growth by the size of nanowires from quantum confinement are unique and interesting properties of nanoscale semiconductor structures.[10, 11]

DFT is a effective method to study these semiconductor nanostructures. With unit cells between dozens and hundreds of atoms, the scale of structural analysis is well within the limits of DFT. The usefulness of DFT in structural and electronic properties of semiconductor materials is also well documented, and the deficiencies in band gap calculations can be corrected using more advanced calculation methods such as hybrid functional analysis, where necessary. The ease with which strain can be applied to systems is beneficial as well. Calculations of semiconductor electronic properties like band structure, electronic orbitals, DOS, work function, and other measurements, which are all influenced by factors like size, edge passivation, and strain, are relatively simple to simulate with DFT calculations. This work includes intrinsic and extrinsic strain, size effects of nanowires and electronic states, and multiple edge passivation methods, and how they alter the electronic properties of the nanoscale semiconductors, and DFT is a remarkable tool for these studies. For example, intrinsic strain is strain introduced to the system through heterostructure interfaces, while extrinsic strain is artificially applied

using the periodic boundary conditions in this DFT methodology. However, it is necessary to first introduce the methodology behind these DFT simulations before delving into the results of this work.

B. The Schrödinger Equation

One could argue that everything within quantum mechanics lies within a many bodied, relativistic, time dependent Schrödinger Equation.

$$i\frac{d}{dt}\Psi(\boldsymbol{r},t) = \hat{H}\Psi(\boldsymbol{r},t) \tag{I.1}$$

In this perspective, it will truly forever remain unknown, since mathematically it is not possible to solve problems where more variables exist than equations. However, for the sake of progress in science, certain assumptions are made to make predictions as close to reality as possible. First, scientists can reduce the problem to time independent solutions of the Schrödinger Equation. It is well-known that one can easily expand into time dependent solutions to the Schrödinger Equation using linear combinations of time independent solutions. Looking to the time independent solutions to the Schrödinger Equation, we find (in atomic units) equation (I.2).

$$E\Psi = \hat{H}\Psi = \sum_i^N -\frac{1}{2}\nabla_i^2\,\Psi + \sum_A^M -\frac{1}{2M_A}\nabla_A^2\,\Psi$$

$$+\left(\sum_i^N\sum_{j>i}^N\frac{1}{r_{ij}} - \sum_i^N\sum_A^M\frac{Z_A}{r_{iA}} + \sum_A^M\sum_{B>A}^M\frac{Z_AZ_B}{R_{AB}}\right)\Psi \tag{I.2}$$

In the above Hamiltonian H, M_A is the ratio of the mass of nucleus A to the mass of an electron, Z_A is the atomic number of nucleus A, r_{iA} is the distance between the electron i and nucleus A, r_{ij} and R_{AB} are the distances between two electrons (i and j) and

4

between two nuclei (A and B) respectively. Still, this is a many bodied system that has electron and nuclei potentials, kinetic energies, and interactions between all particles within. Reducing the problem further, the Born-Oppenheimer approximation assumes that the nuclei of the system are so massive with respect to electrons that they can be treated as stationary, allowing factorization of the wave function of electrons and nuclei to be split into different steps in finding a solution to the total Schrödinger Equation. For now, the focus will be on the electronic part of the problem, as seen in (I.3).

$$\hat{H}_{elec}\Psi = \sum_i^N -\frac{1}{2}\nabla_i^2 \Psi + \sum_i^N \sum_{j>i}^N \frac{1}{r_{ij}}\Psi - \sum_i^N \sum_A^M \frac{Z_A}{r_{iA}}\Psi \qquad (I.3)$$

Even here there is still a many electron equation with many interacting terms that are difficult if not impossible to solve. It is at this point that DFT is applied to the problem, to continue reducing the complexity of the problem into something solvable. There are other methods such as Hartree-Fock (HF) method which also can solve the problem[11], and HSE methods which merge DFT and HF methods will be mentioned briefly later.

<center>C. Density Functional Theory</center>

The Born-Oppenheimer approximation does much to simplify the equation, removing 2 of the 5 terms in the Hamiltonian in equation I.2, by treating the nuclei as stationary relative to the electrons. The kinetic energy of the nuclei is treated as zero, and the Coulomb potential from the nuclei becomes a constant value. Density Functional Theory (DFT) attempts to solve the remaining many electron time-independent Schrödinger Equation by replacing the main focus of the Schrodinger Equation, the wave function, with an electron density, $n(\boldsymbol{r})$.

$$n(\boldsymbol{r}) = \sum_i^N |\psi_i(\boldsymbol{r})|^2 \tag{I.4}$$

In choosing to represent this many body problem using an electron cloud density as given by the Kohn-Sham Method,[13] the number of variables in this problem are greatly reduced, and separating the interactions between electrons is possible. It also provides a relatively simple method of energy minimization, as dictated by the Hohenberg-Kohn theorem.[14]

$$\delta\big[E(n) - \mu\big(\textstyle\int n(\boldsymbol{r})dr - N\big)\big] = 0 \tag{I.5}$$

In the above equation, μ is the Lagrange multiplier, and N is the number of electrons. Since it is known that the external potential yields a unique wave function, and that the electron density is essentially the wavefunction squared, it remains to show the one-to-one relationship between the electron density and the external potential. There is a one-to-one relationship between the external potential and the electron density, shown below. The argument is made by contradiction. Assume that two different external potentials $v(\boldsymbol{r})$ and $v'(\boldsymbol{r})$ corresponding to two separate ground state wave functions Ψ and Ψ' yield the same electron density $n(\boldsymbol{r})$; if this is the case, then the relationship between $v(\mathbf{r})$ and $n(\boldsymbol{r})$ is not one-to-one. Through the variational principle (Rayleigh-Ritz) it would seem that the following equations (I.6) and (I.7) are true when two wave functions with different external potentials yield the same electron density.

$$E = \langle\Psi|\hat{H}|\Psi\rangle < \langle\Psi'|\hat{H}|\Psi'\rangle = E' + \int d^3r\, n(\boldsymbol{r})[v(\boldsymbol{r}) - v'(\boldsymbol{r})] \tag{I.6}$$

$$E' = \langle\Psi'|\hat{H}'|\Psi'\rangle < \langle\Psi|\hat{H}'|\Psi\rangle = E + \int d^3r\, n(\boldsymbol{r})[v'(\boldsymbol{r}) - v(\boldsymbol{r})] \tag{I.7}$$

However, if you add (I.6) and (I.7) together they yield the result,

$$E + E' < E' + E \qquad (I.8)$$

which is a contradiction, meaning that $n(\boldsymbol{r})$ has a one-to-one relation with $v(\boldsymbol{r})$.

Once it is shown that the relationship is one-to-one, the next step is to simplify the individual electronic Hamiltonians with a separation of interactions.

$$h_s \psi_s = -\frac{1}{2} \nabla^2 \psi_s + v_{eff}(\boldsymbol{r}) \psi_s = \varepsilon_s \psi_s \qquad (I.9)$$

In the equation above, h_s is the electronic Hamiltonian of a single electron, v_{eff} is the effective potential of the system, and ε_s the eigenvalue for this electron. By treating the electrons as non-interacting, fictitious particles in an effective potential, the system can be reduced to the individual fictitious electron Hamiltonians of the system to find the overall electronic wave function. In treating the electrons as non-interacting, fictitious particles in an effective potential, we find that the energy is given by (I.10).

$$E[n] = T_s[n] + \int n(\boldsymbol{r}) v_{ext}(\boldsymbol{r}) d\boldsymbol{r} + J[n] + E_{xc}[n] \qquad (I.10)$$

In the equation above, T_s is the kinetic energy of the fictitious non-interacting electrons, v_{ext} is the external potential acting on the electron density, $J[n]$ is the Coulomb interaction term, and $E_{xc}[n]$ is the exchange-correlation energy term. Since we are using T_s as the kinetic energy instead of the actual kinetic energy, it is possible to calculate exactly. Going into more detail, the exchange correlation energy term is shown in equation (I.11).

$$E_{xc}[n] \equiv T[n] - T_s[n] + V_{ee}[n] - J[n] \qquad (I.11)$$

In the above equation, $T[n]$ is the true kinetic energy of the electrons, $V_{ee}[n]$ is the electron-electron interaction potential, and $J[n]$ is the classical Coulomb electron interaction energy. The choice of fictitious, non-interacting "electrons" in effective

potential results in an addition of the kinetic energy difference terms as well as the Coulomb interaction to the exchange correlation energy term. Because all potential terms are functions of the electron density, by providing an initial electron density guess, the effective potential can be calculated, and be used to recursively energy minimize the electron density.

In practice, there are many ways that this exchange energy is described. Local density approximation (LDA), generalized-gradient approximation (GGA), and hybrid functionals (specifically HSE06 for this work) are all used to describe this term. The most basic approach is with LDA, so it will be discussed first. The exchange-correlation terms are split into exchange and correlation, such that $E_{xc} = E_x + E_c$. In LDA calculations it is assumed that a uniform electron gas is a good representation for the electron density. The generalized-gradient approximation adds to the complexity of LDA with a gradient of the electron density, expanding terms to allow for a non-uniform electron density. Finally, the hybrid functionals used in this work combine GGA (PBE) approaches with Hartree-Fock functionals. A mixing term a is used to change the ratio of HF to PBE, in order to increase the accuracy of the band gap or other important properties of the material expected from previously known experimental data.

<div align="center">D. Pseudopotentials</div>

While full electron codes do exist today that are much cheaper than in the past, when this work was completed many were comparatively expensive in relation to the code used in Vienna *ab initio* Simulation Package (VASP). Thus, with the large supercells studied in this work, pseudopotentials that treat the core electrons as part of the nuclei are very useful in reducing the computational cost of the simulation. In creating stationary ions

rather than nuclei, the number of electrons in the electron density is reduced. With this ionic choice, the code can focus on the optimization of the valence electrons that contribute the bulk of the bonding and structural behavior in many elements of the periodic table. It should be noted however that overlap in core and valence electrons is lost to this particular approach, and so often times several options are given with higher number of electrons treated as part of the valence electrons, especially d- and f-orbitals.

In this particular work, it is most common that ultra-soft pseudo-potentials (USPP) or projected augmented wave (PAW) PBE potentials are used. Our choice of USPP for the graphene studies is further explained within that section, and our use of PAW PBE potentials for GaAs and InAs nanowires stemmed mostly from their higher accuracy with their structural lattice parameters in bulk. Other choices of pseudopotentials come from recommendations from VASP.

E. The Self-Consistent Method

After applying DFT to iteratively solve the electronic Schrodinger equation, the system is perturbed in the direction of the gradient of the forces acting on the ions, per specifications chosen by the author of this work in the relaxation settings of VASP. When starting with initial ion locations and an initial electron density guess, the system first calculates the Kohn-Sham effective potential, and then uses this to calculate the wave function, and thus a new electron density. Once this has been solved, the Hohenberg-Kohn theorem is used to regenerate the ionic structure, with any changes usually specific to the type of DFT calculation being performed, and then an additional update is made to the electron density, which then repeats the electronic relaxation again. The electronic relaxation must energy-minimize with every new ionic step, but the ionic steps only

check for energy minimization with each additional completion of an electronic cycle. Once the energy cutoff parameter is met for the ionic system, the calculation is finished. After this calculation is completed, the electronic properties of the structure are generated from the resulting electron density and nuclei configuration.

F. Electronic Property Analysis

In this study, many electronic properties are studied in the same manner across several different chapters. To avoid repetition, certain properties will be discussed in detail here. The most basic electronic property discussed in each of the following chapters is the band gap. However, it should be noted that an approximate treatment of the exchange terms leads to errors in the electron-hole interaction, resulting in a poor description of band gaps. While the actual band gap value often is a poor match with experiment, it is often seen that the trend with strain still models well, so that calculating the band gap is still useful. In this study, the band gap is defined as follows.

$$E_g = E_{CBM} - E_{VBM} \tag{I.12}$$

In this equation, E_g is the band gap, E_{CBM} is the energy level of the conduction band minimum (CBM), and E_{VBM} is the energy level of the valence band maximum (VBM). It is also worth describing direct vs indirect gaps here. Direct gaps occur where the VBM and CBM occur at the same position in k-space. Indirect gaps occur when the VBM and CBM are located in different spaces in k-space. Each type of band gap has different advantages for specific semiconductor applications.

The next common electronic property studied is the effective mass of charge carriers.

$$m^* = \hbar^2 \left(\frac{d^2\varepsilon}{dk^2} \right)^{-1} \tag{I.13}$$

10

The effective mass m* is related to the electron by the curvature of the band structure at the lowest unoccupied molecular orbital (LUMO), and is related to the hole by the curvature at the highest occupied molecular orbital (HOMO). The next common electronic property studied was the work function from a DFT perspective.

In a DFT study using VASP, thermodynamic effects are ignored. Therefore, our definition of work function is slightly different from the work function shown experimentally. Our work function is defined as the energy required to excite an electron from the fermi energy up to the vacuum level of our simulation, rather than from the fermi level to the zero energy definition in experimental work. While the two values are equal at absolute zero, experimentally the fermi level is easier to realize because of thermodynamic effects, while the opposite is true for DFT since thermodynamic effects are not considered.

Finally, this work commonly relates strain dependent energy states of structures with bonding and anti-bonding behavior within the structure. Based upon the Heitler-London's exchange energy model, the different energy shifts with strain are associated with this bonding or anti-bonding behavior.[15] The energies of the bonding and anti-bonding states are given by the following two equations.

$$E_{bonding} = 2E_0 + \frac{e^2}{R} + \frac{K + H}{1 + S^2} \tag{I.14}$$

$$E_{antibonding} = 2E_0 + \frac{e^2}{R} + \frac{K - H}{1 - S^2} \tag{I.15}$$

E_0 is the energy for an isolated atom, K represents the classical Coulomb energy between the electron-electron and electron-ion interactions, the exchange integral term is H, and S is the overlap integral of the orbitals between different atomic sites. For systems

with s-orbital bonding (which occurs a few times in this work), S is usually much smaller than 1 (and thus $S^2 \ll 1$), making H the likely dominant term in determining the linear anti-bonding or bonding energy shifts with strain. The exchange H is given by (I.16).

$$H = \iint \psi_a^*(r_1)\psi_b^*(r_2)\left(\frac{1}{r_{12}} - \frac{1}{r_{2a}} - \frac{1}{r_{1b}}\right) \times \psi_b(r_1)\psi_a(r_2)dr_1 dr_2 \qquad \text{(I.16)}$$

In the equation above, the first inverted distance term r_{12} represents the non-classical electron-electron interaction, whereas the following r_{2a} and r_{1b} terms represent the electron-ion interactions. Depending on the localization of the electron orbitals, the movement of the ions through strain can have a different energy shift from the difference in these distance terms. Alternative models have been proposed that more specifically target nanostructures, such as the Huang *et al.* work.[16] This concludes the summary of the most common electronic properties analyzed multiple times in the following chapters.

Chapter II. GRAPHENE NANORIBBONS

A. Engineering the Work Function

DFT is particularly useful for the study of semiconductors, especially those that are crystalline with relatively small unit cells. Thus, when experimental studies confirmed the existence of graphene, a single layer of graphite,[17] the DFT research of graphene expanded significantly, with new simulations of graphene and ways to manipulate the material for more useful properties than the standard experimentally generated sheet. Ideas such as adding strain, partial or complete passivation layers, or terminating the edges of the graphene with passivation to create nanoribbons were all intensively studied.[3-4] This work focused specifically on the passivation type and strain of armchair graphene nanoribbons (AGNR) as shown in the following published work.[18]

Graphene is a single atomic layer carbon sheet in a honeycomb lattice. Due to its exceptionally high crystalline quality, graphene demonstrates a unique linear dispersion relation and the charge carriers behave as massless fermions.[18] Experiments on graphene have shown the charge mobility exceeded 15,000 cm^2/(Vs) even under ambient conditions.[19] Graphene has been considered as a promising material for many advanced applications in future electronics.[18, 19] Engineering of the structure and electronic properties of graphene is essential for these applications. Recently, tunability of the work function has drawn particular attention.[20-31] For example, in an electronic device using graphene as an active channel layer, the work function of graphene determines the band alignment[21] and directly affects the charge injection between graphene and metallic contact.[22, 23] Graphene is also considered as transparent electrode[21, 24] and cathode

materials[25] in optoelectronic devices. The work function will be critical for maximized energy conversion efficiency. Its atomically thin nature makes vertically standing graphene a promising candidate as a field emitter.[26] A lower work function can dramatically enhance the emitting current.[26] Different approaches have been investigated to modulate the work function, such as employing an external electric field,[27] chemical[21] and metal doping,[22, 28] substrate orientation,[20, 29] and a self-assembled monolayer.[30]

As a practical issue, strain is almost inevitable in fabricated graphene structures, manifesting as the formation of ridges and buckling.[32, 33] Graphene possesses superior mechanical stability. It can sustain a tensile strain up to 30% demonstrated by Kim *et al*.[34] A number of studies have investigated the effect of strain on the electronic properties of graphene and graphene nanoribbons,[35-42] such as the band gap and mobility. To advance graphene based technology, it is essential to examine how strain affects the work function of graphene and graphene nanoribbons. In addition, functional group decoration/passivation is another factor that can be practically involved in the preparation process of graphene. In fact, an extensive effort has been made to employ functional species for tailoring the properties of graphene.[41, 43-49] The combined effect of strain and decoration/passivation on the work function of graphene is also of great interest to investigate.

In the present work, first principles density-functional theory[13] calculations were conducted to investigate the work function of edge passivated armchair graphene nanoribbons (AGNRs) modulated by external uniaxial strains and surface species decoration. Two groups of edge passivation (H and O) and three types of surfaces species (H, F, and OH) have been studied. It has been demonstrated that the strain can effectively

tune the work function of graphene nanoribbons by primarily shifting the Fermi level. Sufficient strain on edge-O passivated AGNRs yields a structural or direct-indirect band gap transition, which can produce a significant change in the work function. Furthermore, it was found that the work function varies with the type and coverage of surface function group. Surface dipoles here have less effect on the work function compared with the surface states introduced by the functional group.

First principles density-functional theory[13] calculations were carried out using Vienna ab-initio Simulation Package.[50, 51] The local density approximation (LDA)[13] was applied. The generalized gradient approximation (GGA)[52] was also used to check the work function of graphene, using both PW-91, and PBE potentials. It was found that the work function predicted by LDA and GGA is 4.48 eV and 4.49 eV, respectively. Both values are in good agreement with other theoretical[22, 35] and experimental[53] studies. The pseudo-potential plane wave approach was employed. The kinetic energy cutoff of the plane wave basis was set to be 450.0 eV. Core electrons of atoms were described using Vanderbilt ultra-soft pseudo-potentials, with ENMAX value of 287 eV.[54] The reciprocal space was sampled using $4 \times 1 \times 1$ Monkhorst-Pack grid[55] centered at the Γ point. A total of 21 K-points were included in the band structure calculations along Γ (0, 0, 0) to X (0.5, 0, 0). The Gaussian smearing method was used to describe partial occupancies of orbitals, with width of the smearing set at 0.05 eV. The total energy in the self-consistent scheme was converged to within 0.01 meV. Atoms were fully relaxed until force and stress components are less than 0.02 eV/Å and 1.0 kbar, respectively. The initial lattice constant along the armchair direction (i.e. x-axis) in a ribbon was set to 4.22 Å, taken from the 2D graphene sheet. The lattice constant of all AGNRs was fully optimized through the

technique of energy minimization. The vacuum distance between the ribbon and its replicas is about 30 Å (y direction) and 16 Å (z direction) to eliminate interaction between ribbon replicas due to periodic boundary conditions.
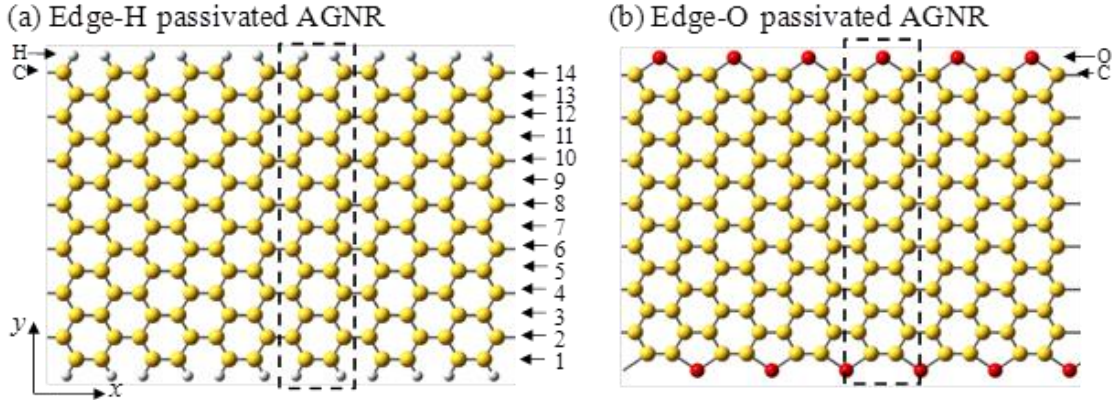
Figure II.1 The images of AGNRs with edge carbon atoms passivated by (a) H and (b) O. The dashed rectangles indicate unit cells. The width of a ribbon is closely related to the number of carbon atoms in the y-direction. The images show the AGNRs with a width of 14 C atoms.

This work first studied the effect of uniaxial strain on the electronic properties such as the band structure, work function, and core level shift of the AGNRs. Two types of edge passivation, H and O, were studied, as shown in Figure II.1. The width of an AGNR is measured as the distance between two carbon atoms on both edges, which is related to the number of C atoms along the zigzag direction (i.e. the y direction in Figure II.1 (a)). It is known that, due to quantum confinement effects, AGNRs can be classified into three families according to the width of the AGNR in which the number of C atoms in the zigzag direction falling in the categories of 3n, 3n+1, and 3n+2, where n is a positive integer.[56, 57] In this work, three widths of AGNRs were chosen, 13.4 Å, 14.6 Å, and 15.8 Å, corresponding to the number of C atoms of 12, 13, and 14, respectively, in the zigzag direction. Shown in Figures II.1(a) and (b) are AGNRs with a width of 14 C atoms. This work also investigated AGNRs with widths of 12 and 13 C atoms, representing the other two families.

16

The structures of the ribbons were fully optimized through energy minimization. Based on the relaxed structure with an optimized lattice constant, uniaxial strain within the range of ±16% was applied by scaling the lattice constant. The positive values of strain refer to uniaxial tensile strain, while negative values correspond to compression. Note that the y and z coordinates of the ribbon are further relaxed at a given strain.

The work function of an AGNR is defined as the energy difference between the vacuum and Fermi levels,

$$\phi = V_{vacuum} - E_{fermi} \tag{II.1}$$

In numerical calculations, the Fermi level is determined by integrating the density of states from the lowest energy level to an energy level (i.e. Fermi energy) which gives a total number of electrons in the unit cell. Specifically, in this work, the Fermi level of the semiconducting AGNRs was set to be the middle of the band gap. The vacuum potential V_{vacuum} is read from the plot of planar-average electrostatic potential energy along the z direction (i.e. pick the value in the middle of vacuum from the plot). All electronic energies of a ribbon in this study are referenced to its vacuum potential energy.

The work function of the AGNRs was studied as a function of uniaxial strain. Both edge-H and edge-O passivation were investigated for AGNRs with different widths. As an example, the strain dependence of the work function in the AGNRs with a width of 14 C atoms is plotted in Figure II.2. It was found that the work function increases with tensile strain and decreases with compressive strain. This observation is similar to the result obtained with a strained 2D graphene sheet.[50]
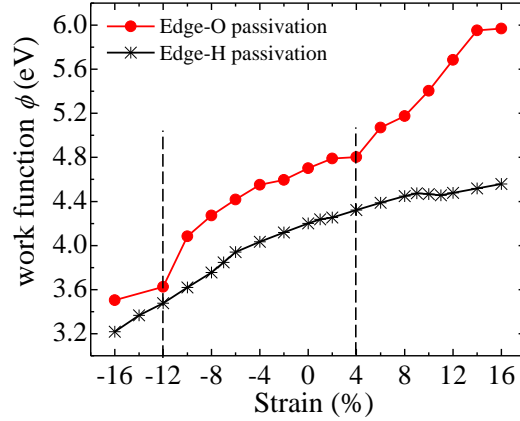
Figure II.2 The work function of the AGNRs with a width of 14 C atoms as a function of uniaxial strain. The vertical lines indicate the strains at which the structural/electronic transitions occur.

Since the work function is determined by two energy levels, E_{fermi} and V_{vacuum}, it is worth examining the strain dependence of these two terms. Figure II.3 (a) shows the Fermi and vacuum levels as a function of strain for the edge-H passivated AGNR. It shows that the strain has a dominating effect in shifting the Fermi level while only having a minimal effect on the vacuum potential energy. For example, the change of the Fermi energy within the strain range considered in this study is 1.59 eV, while the variation of the vacuum level is only 0.13 eV, which suggests that the variation of the work function is mainly contributed by the shift of the Fermi level.
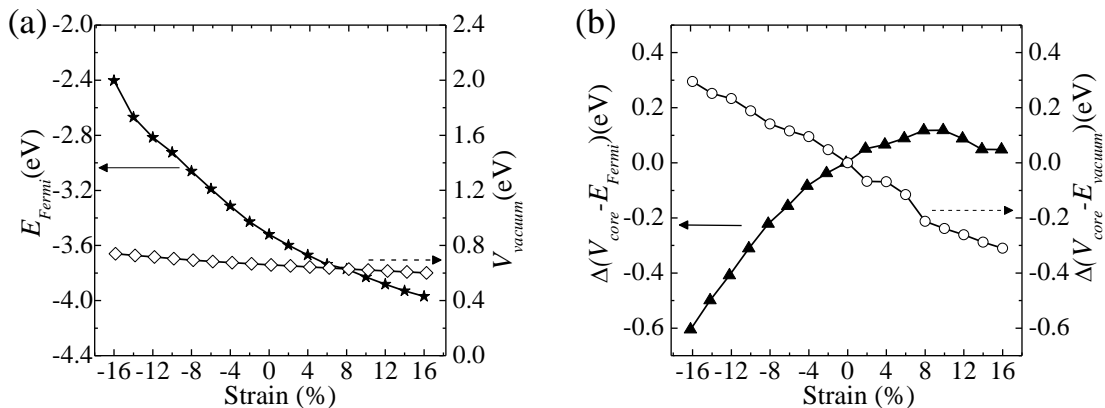
Figure II.3 (a) the variation of Fermi and vacuum levels with strain; (b) the normalized core level shift relative to the Fermi energy and vacuum level under strain for the edge-H passivated AGNR with a width of 14 C atoms.

As shown above, the variation of the work function is also correlated to the core level shift of carbon atoms in the AGNR. To see this, the work function is rewritten as the following formula[58, 59] by inserting the average electrostatic potential energy at carbon ionic cores V_{core},

$$\phi = (V_{core} - E_{Fermi}) - (V_{core} - V_{vacuum}) \tag{II.2}$$

The first term is used for determining the core level shift in a solid film. The second term corresponds to the core level shift relative to the vacuum level.

Both terms in Equation II.2 can be referenced to their values of the relaxed AGNR and plotted in Figure II.3 (b), where

$$\Delta(V_{core} - E_{Fermi}) = (V_{core} - E_{Fermi})_\varepsilon - (V_{core} - E_{Fermi})_0 \tag{II.3}$$

$$\Delta(V_{core} - V_{vacuum}) = (V_{core} - V_{vacuum})_\varepsilon - (V_{core} - V_{vacuum})_0 \tag{II.4}$$

The referenced core level shift relative to the vacuum level in Equation 4 decreases with tensile strain, and increases with compressive strain. Its variation with strain is nearly linear. The change of this shift with strain is mainly due to the electrostatic potential variation with the modulated distance between ionic cores and valence electrons.[60] When the ribbon is under a tensile strain, the valence electrons are further apart from the ionic cores, so the electrostatic potential contributed by valence electrons to the ionic cores is reduced. This causes the potential energy of the ionic cores to decrease.

The core level shift relative to the Fermi energy in Equation 3, however, demonstrates a different behavior with strain, shown in Figure II.3 (b). From the curve, it is observable that this shift is reduced significantly to a smaller value in the compressed strain while the tensile strain barely affects the value. Here, the change in the electrostatic potential

due to the variation of the distance between the ionic cores and valence electrons may have been dominated by the shift of the Fermi energy in the compressed AGNR. In the expanded AGNR, this variation may have been nearly canceled by the shift of the Fermi energy.

In addition, this work studied the AGNRs with different widths, such as 12 and 13 carbon atoms in the zigzag direction. The general trends presented in Figure II.2 and Figure II.3 are also valid for those widths. The distinct trend of core level shift relative to the Fermi energy under tensile and compressive strain make the traditional electron spectroscopy tools such as X-ray photoelectron spectroscopy valuable for characterizing the strain in graphene.[61, 62] This is attractive practically since the strain can be easily introduced into the monolayer graphene structures during preparation processes.

In Figure II.2, it is also found that the work function of the edge-O passivated AGNRs is higher than that of the edge-H passivated nanoribbons under a moderate strain. At a strain larger than ~ 4%, the difference in the work function between these two types of edge passivation increases, while this difference starts to reduce under a compressive strain (~ -12%). As shown below, the deviation of the work function trend under large compressive/tensile strains is correlated to structural/electronic transition of the edge-O passivated AGNRs.

It is interesting to observe electronic and structural transitions in the edge-O passivated AGNRs under large uniaxial tensile and compressive strain, respectively. When a large tensile strain is applied, the band gap of the AGNRs shrinks to zero.[41] For example, the ribbon with a width of 14 C atoms demonstrates a zero-gap at +8% strain. In order to closely examine the gap variation with strain, the band structures of the edge-O

passivated AGNR under different values of strain are presented in Figure II.4. Under

+4% strain, the band gap experiences a transition from direct to indirect. With increasing

tensile strain, the indirect gap decreases to zero at +8% strain. Beyond +8% strain, no gap

exists. This electronic evolution with strain is mainly due to edge defects produced by

tensile strain.[41] The direct-indirect gap transition is also related to the significantly higher

work function of the edge-O AGNR at large tensile strain (see Figure II.2).
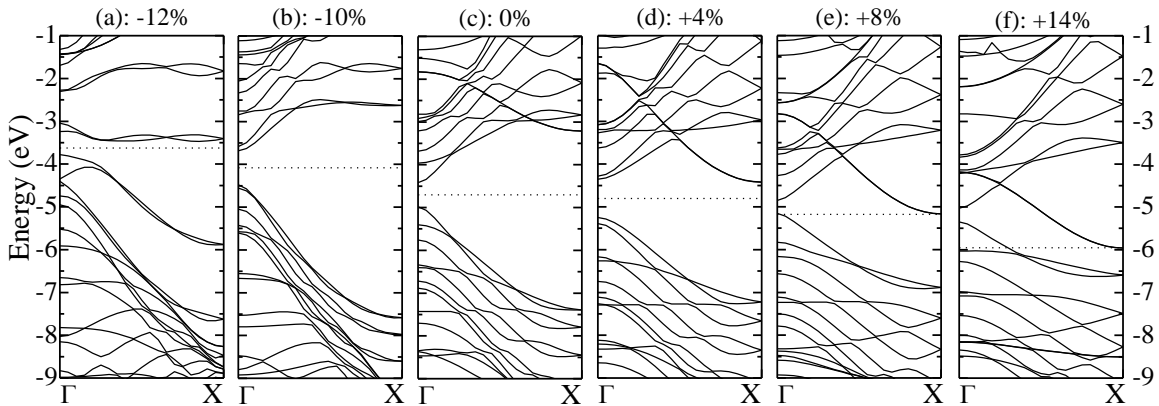
Figure II.4 The band structure of the edge-O passivated AGNR with a width of 14 C atoms under different values of uniaxial strain. The energies are referenced to the vacuum level. The band gap experiences a transition from direct to indirect at +4% strain, and shrinks to zero at +8% strain and beyond. A structural transformation occurs at -12% strain, producing a largely deviated band structure.

On the other hand, the band structure of the AGNR under -12% strain is largely

deviated from the relaxed one. It was found that a structural transformation occurs at this

strain and larger compression. To illustrate the structure transition, the geometries of the

relaxed and -12% strained AGNRs are shown in Figures II.5 (a) and (b). The pentagon

formed by the edge O and four neighboring C in Figure II.5 (a) transfers to a heptagon

under -12% strain in Figure II.5 (b). And the hexagon formed by six C atoms (labeled 2,

4, 6, 1', 3', and 5' in Figure II.5 (a)) transforms to a quadrilateral in Figure II.5 (b).

Besides these rearrangements near the edges of the ribbon, the bond lengths of horizontal

carbon pairs (i.e. C3-C4, C5-C6, C9-C10, C11-C12, C13-C14, C15-C16, etc.) are distinct

in the relaxed and -12% strained AGNRs. For example, in the relaxed ribbon, the pairs of

C3-C4, C9-C10, and C13-C14 form the C-C bond with bond lengths ~1.4 Å, while pairs

of C5-C6, C11-C12, and C15-C16 do not form bonds with C-C distances ~2.7 Å.

However, it is opposite in the -12% strained ribbon, where the latter pairs all form C-C

bonds while the former pairs are apart, shown in Figure II.5 (b). The detailed bond

lengths of these two structures are listed in Table II.I. A similar structure transformation

was also found at the -12% strain in the edge-O passivated ribbon with widths of 12 and
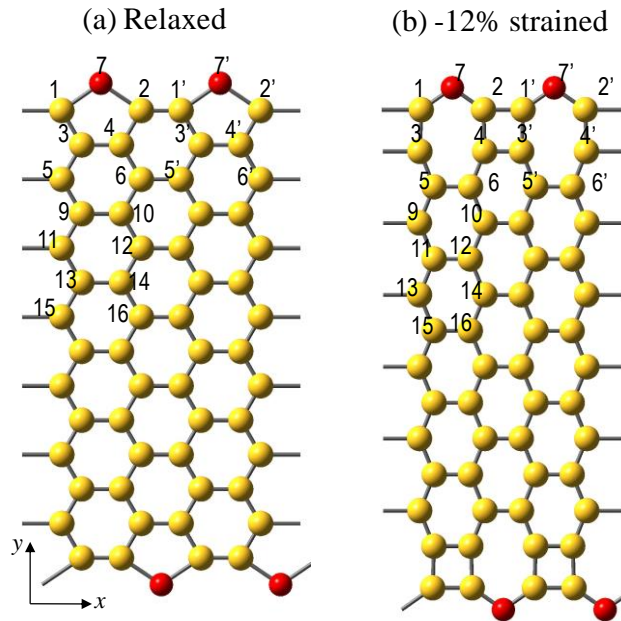
13 C atoms.

Figure II.5 The structures of the (a) relaxed and (b) -12% strained AGNRs with a width of 14 C atoms in two adjacent simulation cells. Note that a structural transformation occurs at -12% strain. The horizontal C-C pairs, such as C3-C4, C5-C6, C9-C10, C11-C12, and C13-C14, have totally different bond distances when compared with the relaxed ribbon. Edge defects such as carbon quadrilaterals form in the -12% strained ribbon.

Table II.I The selected bond lengths in the relaxed and -12% strained AGNRs with a width of 14 C atoms. The number notation of atoms is indicated in Figure II.5.

Bond	Length for relaxed AGNR (Å)	Length for -12% strained AGNR (Å)	Difference (Å)
C3-C4	1.42	2.30	0.88
C3'-C4	2.68	1.31	-1.37
C5-C6	2.73	1.29	-1.44
C5'-C6	1.37	2.31	0.95
C1-C2	2.47	2.20	-0.27
C1'-C2	1.63	1.40	-0.23
C1-C3	1.39	1.47	0.09
C3-C5	1.40	1.35	-0.05
C1-O7	1.50	1.35	-0.15
C2-O7	1.50	1.35	-0.15

Recently tailoring the properties of graphene by surface functional groups has attracted a tremendous interest.[41, 43-49] Here the effects of three types of surfaces species (H, F, and OH) on structural and electron properties of AGNRs are investigated. The starting ribbon is a geometrically relaxed edge-H passivated AGNR with a width of 14 C atoms, as shown in Figure II.6 (a). Based on this ribbon, different surface species, such as H, F, and OH, is decorated on the ribbon surface on either one side or both sides. The number of the decorating surface species varies as 2, 4, 6 and 8, with each addition of one surface atom corresponding to an increment of 3.57% surface coverage (i.e. 1/28, 28 is the number of carbon atoms in the unit cell). For example, Figure II.6 (b) and (c) show the geometrically relaxed ribbons with four and eight H atoms (represented by 4H and 8H) decorated on one side of the ribbon, respectively. It is clear that the ribbons were bent for these cases due to the lattice distortion by the surface decorated species on the same side.[43] The bent geometry compromises the local stress induced by the lattice distortion. Figure II.6 (d) shows the relaxed structure of eight H atoms on both sides of

the ribbon (4 H on each side). The ribbon is not bent and nearly planar. For other species,

F and OH, the relaxed ribbons are similar to those shown in Figure II.6 (b) - (d).
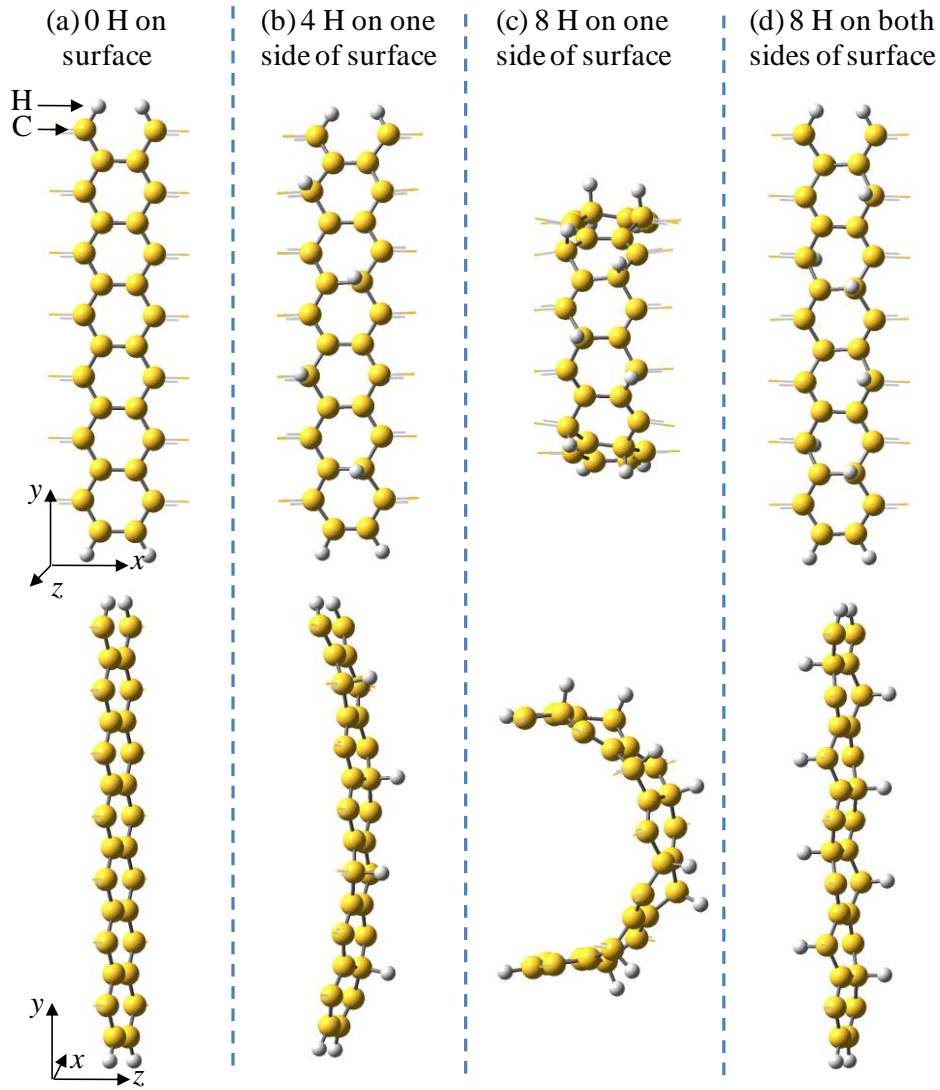
Figure II.6 The AGNRs surface decorated by H atoms. (a) no H atoms on the surface; (b) 4 H atoms on one side; (c) 8 H atoms on one side; (d) 8 H atoms on both sides (4 H each side). Each addition of one H corresponds to an increment of 3.57% surface coverage. The top and bottom rows represent different views indicated by the coordinate axes.

For all AGNRs with different surface species, their structures were fully relaxed

through energy minimization. The lattice constant of the AGNRs were also optimized so

that the force and stress components on each atom were converged to within 0.02 eV/Å

and 1.0 kbar, respectively. The optimized lattice constants were reported in Figure II.7

(a). It shows that the edge-O passivated ribbon without surface species has the shortest

lattice constant of 4.10 Å. For the edge-H passivated ribbon, the lattice constant increases to 4.25 Å. The lattice constant slightly increases with the number of surface H species decorated on the ribbon, to 4.30 Å with eight surface H atoms. A similar effect was also found in the surface species F and OH. In addition, for the same number of surface species, there is no significant difference in the lattice constant between the cases of one-side and two-side decoration.
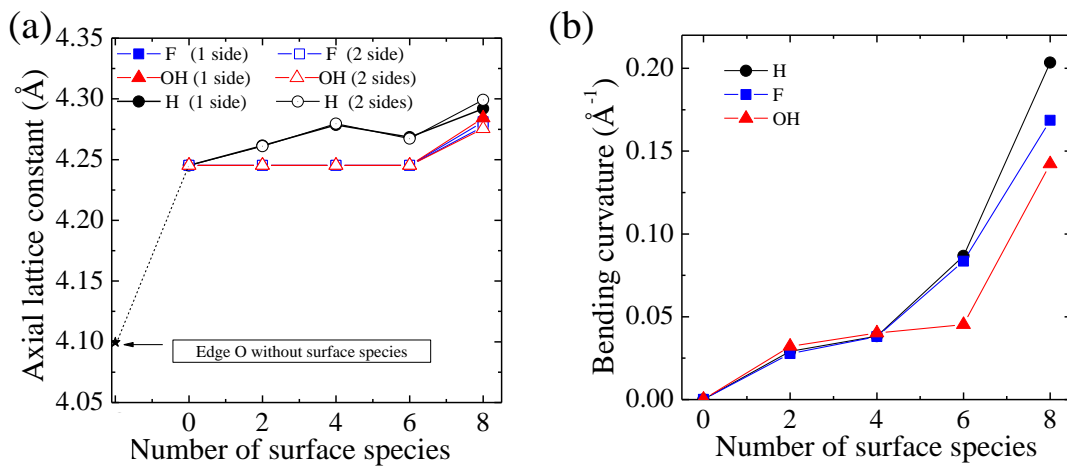
Figure II.7 (a) The relaxed lattice constant and (b) the bending curvature of the AGNRs with different surface functional species.

As shown in Figure II.6 (b) and (c), the relaxed ribbons are bent if the species were decorated on one side of the ribbon. Increasing the density of the surface species will increase the ribbon bending curvature (defined as 1/R, where R is the radius of the bending ribbon). The bending curvature of the AGNRs as a function of surface species coverage is plotted in Figure II.7 (b). It is clear that the curvature increases rapidly with increasing number of surface species. For example, the curvature of the ribbon with 4H and 8H surface species are 0.038 Å^{-1} and 0.203 Å^{-1}, respectively, which have corresponding curvature radii of 26.12 Å and 4.92 Å, respectively. In addition, the AGNRs with widths of 12 and 13 C atoms in the zigzag direction were explored. Our

calculations showed that there is no distinct difference in the predicted curvature for the

AGNRs with different widths. Our calculated bending structures and curvatures of

AGNRs were consistent with that of first-principles molecular dynamics simulation

conducted by Yu and Liu.[43]
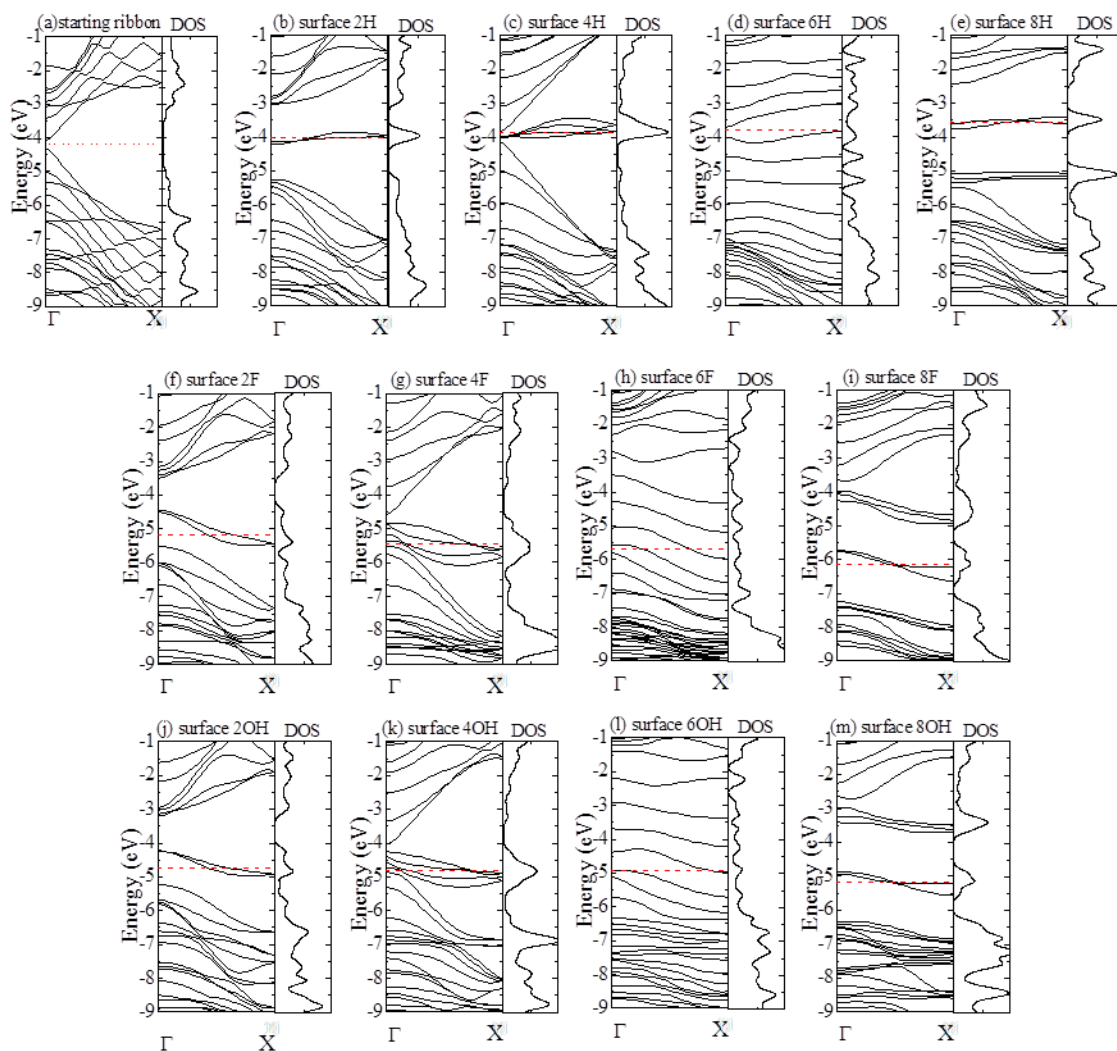
Figure II.8 The band structure and the corresponding density of states of the AGNRs with different surface functional species decorated on one side of the ribbon surface. The starting ribbon is the edge-H passivated AGNR with a width of 14 C atoms in which no surface species were decorated. The notation "surface 2H" denotes two H atoms are decorated on the ribbon surface.

Electronic properties were investigated for the AGNRs with different surface species.

As an example, band structures and the corresponding density of states (DOS) for the

AGNRs with one-side surface species decoration are plotted in Figure II.8. As a

reference, the band structure and DOS for the starting ribbon (i.e. the edge-H passivated ribbon without surface species) is also presented in Figure II.8 (a). All energies are referenced to the vacuum level. The Fermi level is represented by the horizontal dashed line. It was known that the edge-H passivated AGNR is a semiconductor, shown in Figure II.8 (a). However, introduction of the surface species, such as H, F and OH, bring surface states near the Fermi level. Increasing the coverage density of the surface species, the band structures and DOS are deviated farther from that of the starting ribbon. For example, Figures II.8 (b), (f) and (j) display the band structures and DOS for 2H, 2F, and 2OH surface species, respectively. Two surface states were brought in near the Fermi level. However, the energy bands and DOS in which energies are far away from the Fermi level are similar to that of Figure II.8 (a). When the number of surface species increases from two to four, more surface states appear near the Fermi level, and the DOS is further modified, as shown in Figures II.8 (c), (g), and (k). Continuing to increase the number of the surface species to six and eight significantly altered the band structure and DOS.

This work also studied the band structures and DOS for the AGNRs with surface species decorated on both sides of the ribbon. It is interesting to note that the band structures and DOS are very similar to those of one-side decoration. For example, the band structure and DOS for the AGNR with each side decorated by one H atom is very close to the one in Figure II.8 (b).

The calculated work function of the AGNRs is reported as a function of the number of surface species in Figure II.9. Generally, different surface species affect the work function in a different manner. For example, adding surface H to the ribbon decreases its

work function, while adding surface F or OH increases the work function. Therefore, the surface species can be classified into two groups, one increasing the work function (such as F and OH), and the other reducing it (such as H).
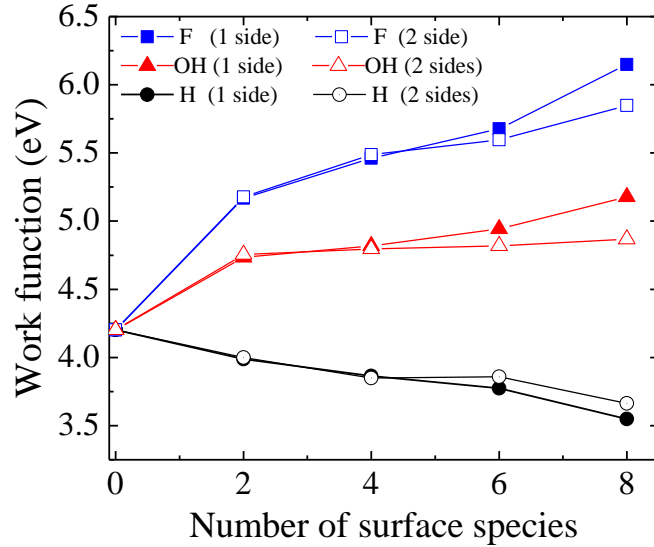
Figure II.9 The work function of the AGNRs with different surface functional species.

The work function shift by the surface decoration could come from two sources: (i) molecular dipoles formed between the decorated species and the ribbon surface; (ii) charge rearrangements induced by the chemical bond formation between the decorated species and the ribbon surface.[63-65] This study argued that the work function shift here is primarily due to the latter. This can be seen from the surface states introduced near the Fermi level in the band structures (Figure II.8). These surface states come from the transition of carbon atoms from sp^2 to sp^3 hybridization.[47] F and OH with a higher electronegativity could introduce deeper states while H with a lower electronegativity could introduce shallower states. For example, the surface bands introduced by 2F and 2OH surface species are in the range of -4.5 ~ -5.5 eV, and -4.2 ~ -5.0 eV, respectively (see Figures II.8 (f) and (j)). However, the surface band introduced by 2H species is in the range of -3.9 ~ -4.2 eV, which is much shallower, shown in Figure II.8 (b).

28

The contribution of the molecular dipole from surface decoration can be evaluated from the work function difference between one side and two side decoration. In one side decoration, the molecular dipole will introduce an additional potential change to the vacuum level,[63, 66] while in the two-side decoration, molecular dipoles on the two faces will tend to cancel each other. From Figure II.9, it is found that work function difference between one side and two side decorations is small, which suggests the introduced surface dipole plays a minor role here. The molecular dipole C+-F-/C+-OH enhances the potential barrier to the vacuum level.[63, 66] For the H group, however, the molecular dipole C--H+ reduces this potential barrier. Another possible factor contributing to the work function difference between one side and two side decoration is the deviation in the ribbon geometries, which indicates the existence of the different local strain at these two cases. For example, for the 8H surface species, the two-side decoration yields a nearly planar ribbon, while the one-side decoration produces a largely bent structure, shown in Figures II.6 (d) and (c).

In summary, using first principles density-functional theory calculations, it was found that (1) the work function of AGNRs increases with tensile strain, and decreases with compressive strain, regardless of the type of edge passivation O and H; (2) the core level shift relative to the Fermi energy decreases with compressive strain, while tensile strain only affect it slightly; (3) the edge-O passivated AGNRs experiences a direct-to-indirect band gap transition under sufficient tensile strain and a structural transformation occurs with a large compressive strain; (4) F and OH surface decoration increases the work function while H decoration decreases the work function of AGNRs; (5) one-side and

29

two-side surface species decoration brings only relatively small difference in the work function, given the same number of surface species.

As a final note, the topic of proper credit for work should be revisited here. This work is a collaboration between Xihong Peng, Fu Tang, and Andrew Copple. The author of this dissertation mainly focused on L13 AGNRs with main focus on band gap and work function with strain and passivation species changes.

B. AGNR Additional And Future Work

In addition to this work, studies were made on the edge effects of Sulfur and Fluorine passivation on L13 AGNRs. While the results were very similar to Oxygen and Hydroxyl group passivation, respectively, the band gap vs strain pattern is displayed below. The only noteworthy differences to be found were the unique relaxed lattice parameters (4.18Å and 4.32Å, respectively), and the critical strain for direct-indirect band gap for Sulfur (+15.5%).
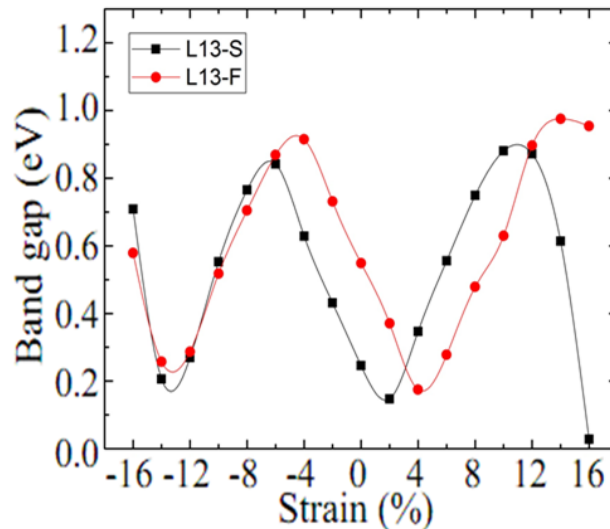
Figure II.10 The L13 S and F passivated AGNR band gaps are shown. While their strain behavior is very similar to previously studied O and OH passivated AGNRs, they do exhibit different relaxed lattice constants, meaning that there are still unique traits specific to these passivation methods.

In addition, future work on this system should include larger nanoribbon widths to show reduction of edge effects on the system, as well as strains that are not along the axis of the ribbon, or are not uniform in behavior. In addition, more extensive study could be done with chiral and defect-filled ribbons, especially with the greater ribbon widths.

Chapter III. PHOSPHORENE NANOSHEETS AND NANORIBBONS

A. Phosphorene, a New 2D Material

Two dimensional (2D) layered crystal materials have attracted extensive research efforts in recent years, such as graphene[17, 71] and molybdenum disulfide,[72] for their potential applications in future electronics. Most recently, researchers have successfully fabricated new 2D few-layer black phosphorus[67-70] and found that this material is chemically inert and has great transport properties. It was reported that it has a carrier mobility up to 1000 cm^2/V·s[4] and an on/off ratio up to 10[67, 68] was achieved for the phosphorene transistors at room temperature. In addition, this material shows a finite direct band gap at the center of Brillouin zone[67, 68, 73-75] (in contrast to the vanishing gap in graphene), which creates potential for additional applications in optoelectronics.

Tailoring electronic properties of semiconductor nanostructures has been critical for their applications. Strain has long been used to tune electronic properties of semiconductors.[76, 77] As a practical issue, strain is almost inevitable in fabricated monolayer nanostructures, manifesting as the formation of ridges and buckling.[32, 33] But a more interesting case comes from intentionally introduced and controlled strains. Methods for introducing strain include lattice mismatch, functional wrapping,[78, 79] material doping,[80, 81] and direct mechanical application.[82] It was found that nanostructures maintain integrity under a much higher strain than their bulk counterpart,[83, 84] which dramatically expands the strength of applicable strain to nanostructures. In particular, 2D layered materials, such as graphene and MoS$_2$, possess superior mechanical flexibility and can sustain a spectacularly large strain ($\geq$ 25%).[85-87] This work calculated the stress-strain relation in phosphorene and found that it can withstand a tensile strain up to 30%.

32

Compared to other 2D materials such as graphene, phosphorene demonstrates superior flexibility with an order of magnitude smaller Young's modulus.[88] This is especially useful in practical large-magnitude-strain engineering of this material.

As already demonstrated by several research groups, strain shows remarkable effects in modifying the electronic properties of phosphorene. For example, Rodin *et al.*,[73] using density functional theory and tight-binding models, predicted an anisotropic dispersion relation with a direct band gap for phosphorene. They analyzed the localized orbital composition of the band edge states and suggested a semiconductor-to-metal transition with compression. Liu *et al.*[68] briefly reported the sensitive dependence of the band gap on in-layer stress and a critical compressive strain of 3% to trigger the direct-to-indirect band gap transition. Fei and Yang[89] theoretically predicted that the preferred conducting direction in phosphorene can be rotated by 90 degrees with an appropriate biaxial or uniaxial strain based on the anisotropic behavior of the material.[68, 73, 90]

However, a full picture of detailed and systematic analysis of the strain effect on the band structure is still missing. For example, what is the elastic limit for phosphorene? Where is the conduction/valence band edge located when the band gap becomes indirect? Is there any additional critical strain to trigger the band gap transition? What is the mechanism/origination for this direct-indirect band gap transition? In present work, these questions are answered by providing tension-strain relation and a full analysis of strain effects on the band structure of phosphorene. By revealing the evolution of band structure with strain, it is clear to see the shift of the band edges and gap transitions. Several critical strains have been identified to trigger the direct-indirect transition. In addition, with sufficient large tensile (+11.3%) or compressive (-10.2%) strain, the indirect band

gap was found to become direct again. Five strain zones with distinct band structure were identified. This detailed analysis on the direct-indirect band gap transition is crucial for optical applications of phosphorene. For example, our group predicted a similar direct-indirect band gap transition in GaAs nanowires with uniaxial strains[91, 92] and the gap transition was observed in a recent experiment[93] in which the luminescence of GaAs nanowires can be switched on and off under the influence of a uniaxial stress.

In this work, the mechanism for the gap transition is discussed in detail by examining the bond nature of near-band-edge electronic orbitals. This mechanism has been applied successfully in many other semiconductor nanostructures.[18, 91, 92, 94-100] Effective masses of charge carriers (thus carrier mobility) were also found to be drastically tuned by strain.

The first principles DFT[101] calculations were carried out using the Perdew-Burke-Ernzerhof (PBE) exchange-correlation functional[101] along with the projector-augmented potentials[102, 103] for the self-consistent total energy calculations and geometry optimization. Both standard DFT with generalized gradient approximation (GGA) and hybrid functional[104, 105] methods were adopted to investigate the strain effect on the electronic properties of phosphorene. In the hybrid HSE06 method,[104, 105] the exchange-correlation functional uses a mixing parameter to incorporate Hartree-Fock (HF) exact exchange functional and the PBE functional. In this study, the fraction of the HF exchange was set to be the default value $\alpha = 0.25$. Both methods of the DFT-PBE and HSE06 give consistent results of the strain effects on the electronic band structures, including the direct-indirect band gap transition and the gap variation trends with strain.

The calculations were performed using VASP.[50, 51] The kinetic energy cutoff for the plane wave basis set was chosen to be 350 eV. The reciprocal space was meshed at 14 ×

10×1 using the Monkhorst-Pack method. The energy convergence criteria for electronic and ionic iterations were set to be 10^{-5} eV and 10^{-4} eV, respectively. Such parameter settings ensure the calculations were converged within 5 meV in total energy per atom. To simulate a monolayer of phosphorene, a unit cell with periodic boundary condition was used. A vacuum space of at least 16 Å was applied to minimize the interaction between layers. In band structure calculations, 21 points were collected along each high symmetry line in reciprocal space.

Unlike a flat structure of graphene, the single layer black phosphorus has a puckered honeycomb structure with each phosphorus atom covalently bonded with three adjacent atoms (see Figure III.1). The initial structure of phosphorene was obtained from black phosphorus.[106] Our calculated lattice constants for bulk black phosphorus are $a = 3.308$ Å, $b = 4.536$ Å, and $c = 11.099$ Å, and are in good agreement with experimental values[106] and other theoretical calculations.[68, 90] The relaxed lattice constants for a monolayer of phosphorene are $a = 3.298$ Å, and $b = 4.627$ Å.
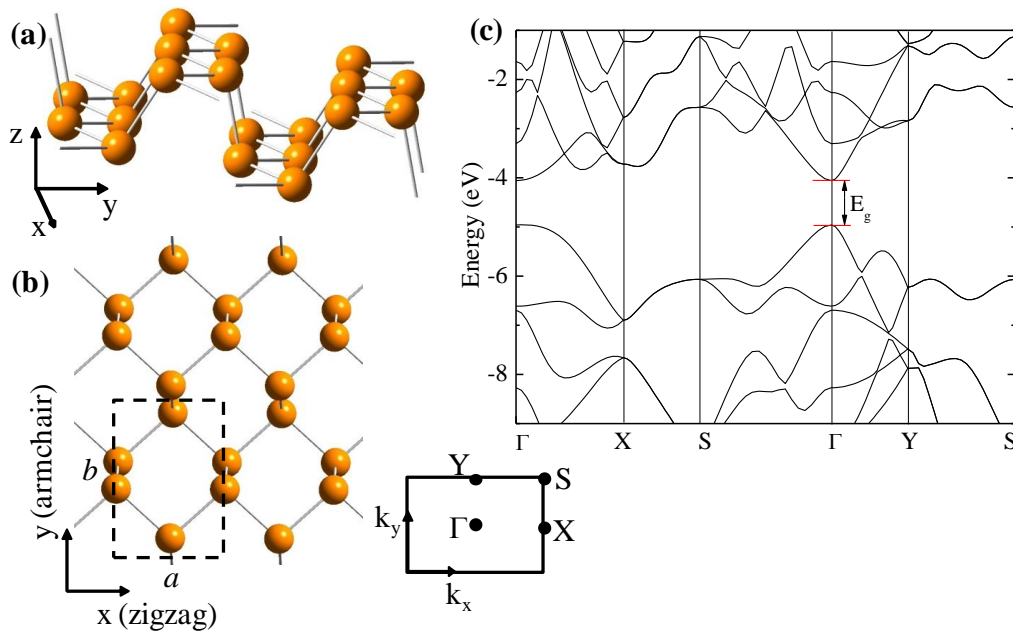
35

Starting with the relaxed phosphorene, strain within the range of $\pm 12\%$ was applied in either the x (zigzag) or y (armchair) direction to explore its effects on the band structure. The applied strain is defined as $\varepsilon_x = \frac{a_x - a_{x0}}{a_{x0}}, \varepsilon_y = \frac{a_y - a_{y0}}{a_{y0}}$, where $a_x \left(a_y\right)$ and $a_{x0} \left(a_{y0}\right)$ are the lattice constants along the x (y) direction for the strained and relaxed structures, respectively. The positive values of strain refer to expansion, while negative corresponds to compression. With each axial strain applied, the lattice constant in the transverse direction was fully relaxed through the technique of energy minimization to ensure the force in the transverse direction is a minimum.

Generally, a compression applied in an axial direction results in an expansion in the transverse direction. The applied axial strains in the x (y) direction and the transverse strain response in the y (x) direction are reported in Figure III.2 (a). The Poisson's ratio, $\nu = -\frac{d\varepsilon_{transverse}}{d\varepsilon_{axial}}$, was found to be 0.7 and 0.2 for the axial strain applied in the zigzag and armchair directions, respectively. These significantly different Poisson's ratios further indicate the anisotropic nature of phosphorene. Figure III.2 (b) presents the change in the total energy of phosphorene as a function of the applied axial strain. The deeper energy surface for ε_x suggests that strain is more difficult to apply in the zigzag than the armchair direction.

To estimate the elastic limit of phosphorene, this work calculated the stress (force per unit length)[107] of phosphorene as a function of tensile strain, using the method described in the references.[108, 109] This method of calculating stress-strain relation was originally introduced for three dimensional crystals. In a 2D monolayer phosphorene, the stress

36

calculated from the Hellmann-Feynman theorem was modified to be the force per unit length.[107] The tensile strain is applied in either the zigzag or armchair direction. Our calculated stress-strain relation is presented in Figure III.2 (c). It shows that phosphorene can sustain a stress up to 10 N/m and 4 N/m in the zigzag and armchair directions, respectively. The corresponding tensile strain limits are 27% and 30% along the zigzag and armchair axes, respectively. This predicted elastic strain limit is close to that found in other 2D materials such as graphene and MoS_2,[85-87] suggesting that phosphorene is highly flexible and may have potential applications in flexible displays.
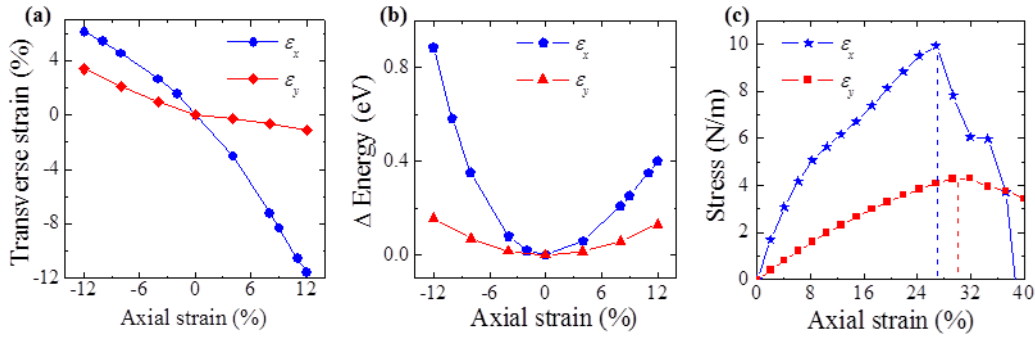
Figure III.2. (a) The applied axial strains in the x and y axes and their transverse strain response in the y and x directions, respectively. (b) The change in the total energy as a function of the applied strain. (c) The stress as a function of tensile load for phosphorene. Phosphorene can withstand a critical tensile strain up to 30% in the armchair direction. The different behaviors along the x and y directions in (a)-(c) indicate the anisotropic nature of phosphorene.

Our DFT predicted band gap for 2D phosphorene is 0.91 eV, which is in agreement with other theoretical work.[68, 75] It is well known that DFT underestimates the band gap of semiconductors, and the advanced GW method can provide improved predictions. The GW gap for phosphorene calculated by Yang's group[75] is about 2.0 eV. However, the present work is mainly focused on the strain effect on the band structure and the advanced hybrid functional method HSE06 gives results of the strain effects on the electronic band structures consistent with that of the DFT-PBE method. In addition, previous studies[95] on Si nanoclusters showed that the energy gap calculated by DFT

obeys a similar strain-dependency as the optical gap predicted by the advanced

configuration interaction method and the quasi-particle gap. Therefore, it is expected that

DFT can correctly predict the general trends of strain effect on the band structure and

near-gap states in phosphorene.

By comparing the band structure of phosphorene at different values of axial strains,

this study found that strain has a remarkable effect on the band structure along two

particular K directions, Γ to X (0.5, 0, 0) and Γ to Y (0, 0.5, 0), respectively. For

simplification, this work only plotted the band structure along these two directions in

Figures III.3 and III.4.
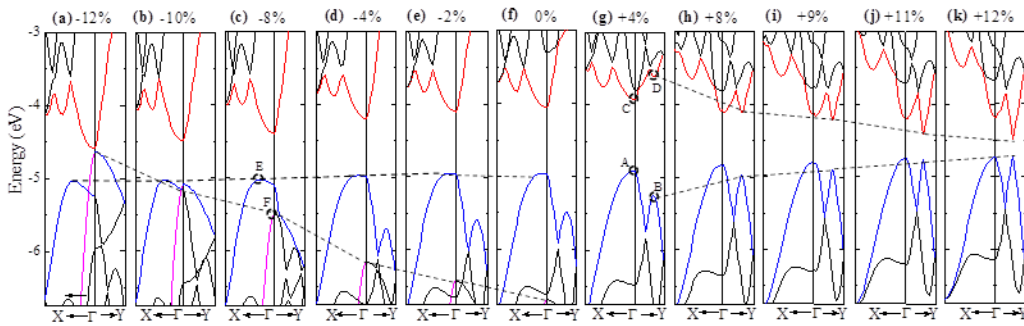
Figure III.3. The strain ε_x (applied in the zigzag direction) manipulated direct-indirect band gap transition in 2D phosphorene. Positive strain indicates expansion while negative corresponds to compression. All energies are referenced to vacuum level. Starting from the relaxed structure, the band gap experiences a direct-indirect-direct transition with both tensile and compressive strain. The direct/indirect nature of the band gap is the result of the competition among the energies of near-band-edge states A – F. The dashed lines are guide for eye for the energy shifts of states B, D, E, F.

Figure III.3 presents the effect of strain ε_x (applied in the zigzag direction) on the

band structure. Figure III.3 (f) is for the relaxed phosphorene with a direct band gap at Γ.

With an increase of tensile strain, the band gap becomes indirect, then transitions back to

direct. For example, at $\varepsilon_x = +9\%$, it shows an indirect band gap with the conduction band

minimum (CBM) shifted from Γ to K1 (0, 0.3, 0) while the valence band maximum

(VBM) remains at Γ. At $\varepsilon_x = +12\%$, it gives a direct gap with both the CBM and VBM at

K1 (0, 0.3, 0). Similarly, with an increase in compression, the gap first transitions to indirect and then back to direct. For instance, at $\varepsilon_x = $ -8%, the gap is indirect with the CBM remains at Γ while the VBM shifted to K2 (0.15, 0, 0). When $\varepsilon_x = $ -12%, it shows a direct gap with both the CBM and VBM at Γ.

Figure III.3 clearly demonstrates that the direct/indirect nature of the band gap is the result of the competition of the energies of several near-band-edge states. With an increase in tensile strain, the energy of the conduction band (CB) at K1 (0, 0.3, 0), labeled as state D in Figure III.3 (g), reduces rapidly and becomes equal to that of state C (CB at Γ, i.e. the original CBM) when $\varepsilon_x = $ +8%. With the strain higher than +8%, state D has a lower energy than C, thus D becomes the CBM. Similar behavior occurs with the valence band (VB). The energy of state B at K1 (0, 0.3, 0) increases faster than A (VB at Γ, i.e. the original VBM). At $\varepsilon_x = $ +12%, B has a higher energy than A, and thus represents the VBM.

On the side of compression, the CBM is always located at Γ (state C). However, the VBM demonstrates an interesting transition. First, at $\varepsilon_x = $ -2%, the VB at K2 (0.15, 0, 0), labeled as state E in Figure III.3 (c), shows an equal energy with A (i.e. VB at Γ). With increased compression, the energy of state E is higher than that of A, indicating a direct-to-indirect gap transition. At $\varepsilon_x = $ -12%, the energy of a sub-VB (the pink band) state F at Γ has a higher energy than E and becomes the VBM, showing a direct band gap at Γ.
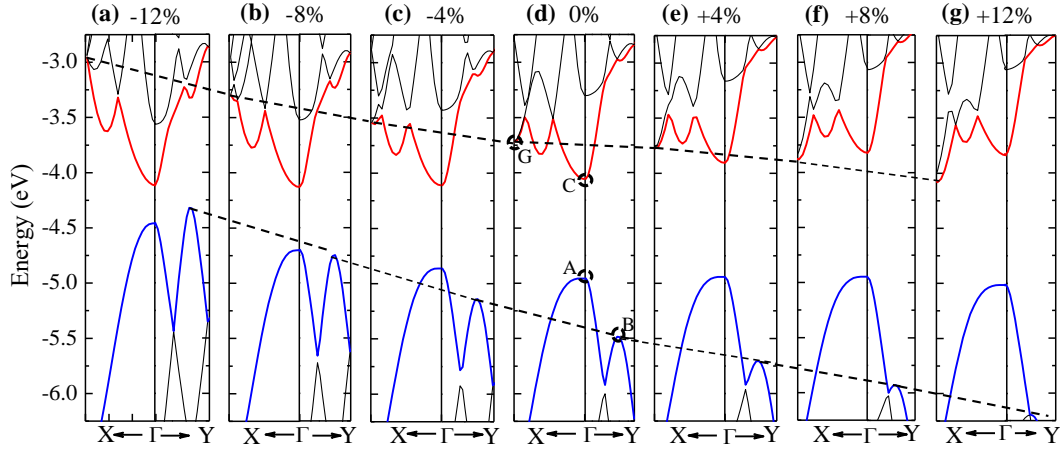
Figure III.4. The strain ε_y (applied in the armchair direction) manipulated direct-indirect band gap transition in phosphorene. All energies are referenced to vacuum level. The band gap shows a direct-indirect transition with expansion/compression. The direct/indirect nature of the gap results from the energy competition of near-band-edge states A, B, C, and G. The dashed lines are a guide for viewing the energy shifts of states B and G.

Figure III.4 shows the effect of strain ε_y (applied in the armchair direction) on the band structure of phosphorene. It demonstrates that both expansion and compression can convert the band gap to indirect. For instance, at $\varepsilon_y = +8\%$ and $+12\%$, the gap is indirect with the VBM at Γ while the CBM shifted from Γ to X. At the side of negative strain, the gap is indirect at $\varepsilon_y = -12\%$ with the VBM at K1 (0, 0.3, 0). It is clear that two VB states A and B compete for the VBM and two CB states C and G (CB at X) exchange dominance for the CBM. The energy shift of states B and G with strain are more prominent than their competing states A and C, respectively.
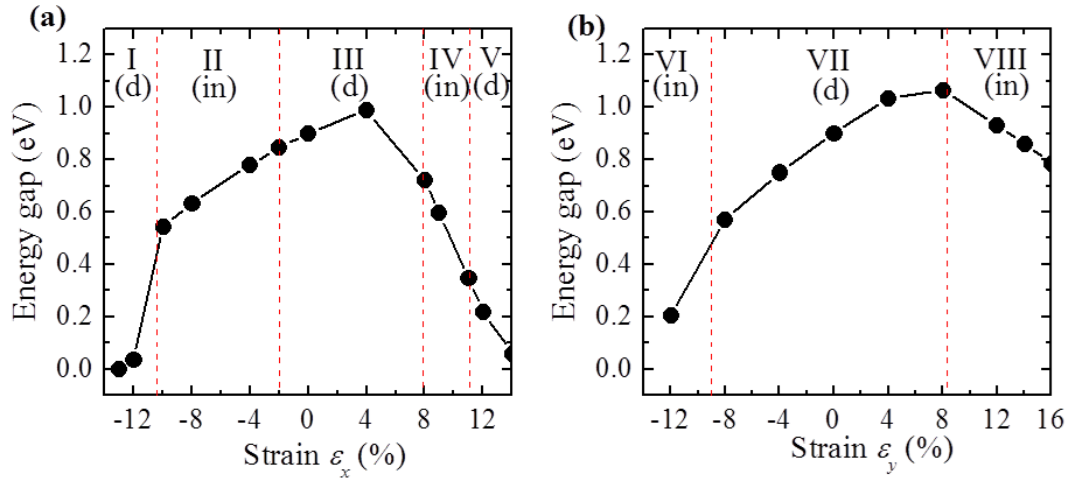
Figure III.5. The band gap of 2D phosphorene as a function of strain ε_x applied in the zigzag (left) and ε_y in the armchair (right) directions, respectively. Five (three) strain zones were identified for ε_x (ε_y) based on its distinct band structures. Zones I, II, III, IV, and V in (a) are corresponding to the direct (d), indirect (in), direct, indirect, and direct gap, respectively. The critical strain for the gap transition are -10.2%, -2%, +8%, and +11.3%. The gap closes up at $\varepsilon_x =$ -13%. Zones VI, VII, and VIII in (b) present the indirect, direct, and indirect gap, respectively and the critical strains of the zone borders are $\varepsilon_y =$ -9% and +6.8%.

The band gap is defined as the energy difference between the CBM and VBM. From Figures III.3 and III.4, the gap strongly depends on strain. In Figure III.5, the gap is plotted as a function of both strains ε_x and ε_y.

For the strain applied along the zigzag direction in Figure III.5 (a), the band gap is initially increased with tensile strain from a value of 0.91 eV for the relaxed structure and reaches the maximal value of 0.99 eV at +4% strain, then drops rapidly with further increased expansion. At $\varepsilon_x = +12\%$, the band gap is reduced to 0.22 eV. To see if the gap reduces to zero with further increased tensile strain, this work explored even larger strain +13% up to +16% with a 1% increment. The gap was not found to close. It reaches a minimal value of 0.06 eV at +14% strain, and then opens up again for larger strain.

On the side of negative strain ε_x, the gap reduces, mainly resulting from the downward shift of the CBM (see Figure III.3). At $\varepsilon_x = -12\%$, the gap sharply drops to 0.04 eV from the value of 0.55 eV at -10% strain. This is due to the fact that the VBM

was replaced by a newly raised sub-valence band (state F). To explore if the band gap reduces to zero with a larger compression, this work explored -13% strain and found that the DFT gap indeed closed up.

In Figure III.5 (a), five strain zones were identified based on their distinct band structure. Zone I is for a direct band gap within the strain range -12% to -10.2%, in which the CBM is represented by state C and the VBM is given by state F. Zone II corresponds to an indirect band gap from -10.2% to -2%, where the VBM is state E. Zone III is a direct gap at Γ from -2% to +8%. Zone IV is an indirect gap from +8% to +11.3%, where the CBM is at (0, 0.3, 0). Zone V shows a direct band gap with both the CBM and VBM at (0, 0.3, 0). The critical strains of -10.2%, -2%, +8% and +11.3% are the zone boundaries that are determined in the next section.

Figure III.5 (b) presents the band gap as a function of strain applied in the armchair direction. The reduced gap value with compression mainly results from the downward shift of the CBM and upward change of the VBM (see Figure III.4). The drop of the gap value at +12% is a consequence of the CBM being replaced by the CB at X (state G). Three unique strain zones are characterized. Zone VI is for an indirect band gap from -12% to -9% where the VBM is located at (0, 0.3, 0). Zone VII is for direct band gap at Γ from -9% to +6.8%. Zone VIII shows an indirect band gap in the strain range +6.8% to +12%, in which the CBM is at X.

Since DFT at the GGA level is known to underestimate the band gap of semiconductors, it is important to test the robustness of the calculated strain effects on the band structures of phosphorene. This work used the advanced hybrid functional HSE06 to calculate the band structures of phosphorene under different values of axial strain in

the zigzag direction and the results are presented in Figure III.6. Comparing the HSE06 predicted band structures in Figure III.6 (a)-(e) with that of the DFT in Figure III.3, one can conclude that both methods give consistent results of the strain effects on the band structures. For example, the direct band gap of the material without strain (0%) converts to indirect under +9% strain and then becomes direct again with +12% strain. On the side of compression, the gap is indirect and direct under -8% and -12% strains, respectively. This work also used the HSE06 method to calculate the band structures of phosphorene under different values of strain in the armchair direction and found that they are in great agreement with those obtained from the standard DFT.
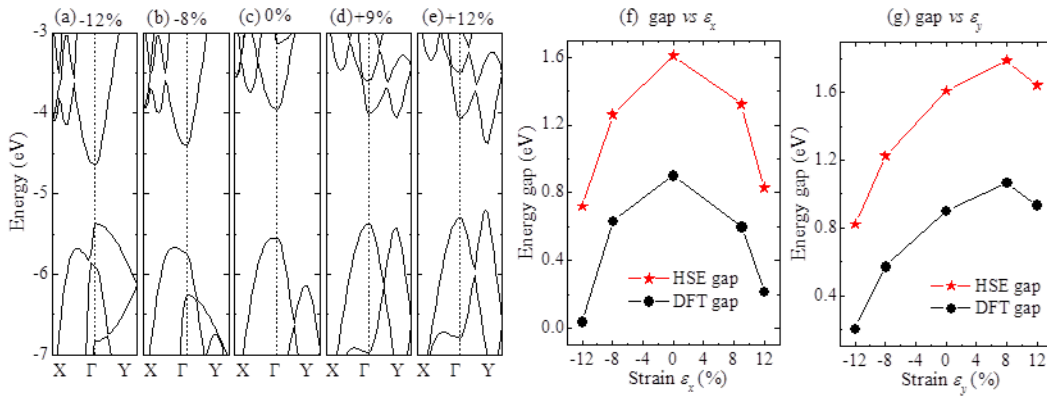
Figure III.5. (a) - (e) The hybrid functional HSE06 predicted band structures of 2D phosphorene with different values of strain ε_x in the zigzag direction. Starting with the relaxed structure, the band gap experiences a direct-indirect-direct transition with both tensile and compressive strain, which is in great agreement with that predicted by the standard DFT. (f)-(g) the band gaps predicted by the standard DFT and HSE06 for both strains ε_x and ε_y. Although DFT underestimates the band gap, its calculated gap-strain variation trend is consistent with that of HSE.

The band gaps predicted by the DFT and HSE06 as a function of strains ε_x and ε_y are presented in Figure III.6 (f) and (g). It is clear that the HSE06 has a better prediction on the band gap value. The HSE06 calculated band gap for the relax phosphorene is 1.61 eV, which is 0.7 eV higher than the DFT gap. However, both methods of the DFT and HSE06 calculated the same gap variation trends with strain. Therefore, it is observable that DFT correctly predicts the general trends of strain effects on the band structure and near-gap

43

states in phosphorene, including the direct-indirect band gap transition and the gap variation trends with strain.

To determine the critical strain in which the direct-indirect band gap transition occurs, the energies of the near-band-edge states A-G were plotted (labeled in Figures III.3 and III.4) as a function of strain in Figure III.7. As seen from Figures III.3 and III.4, these are the states which compete for the CBM and VBM, thus their energies determine the direct/indirect nature of the gap. In Figure III.7, the energies of the states display a nearly linear function with strain. For instance, the energy of state B increases with a positive strain ε_x while decreases with a negative strain ε_x. In contrast, states D and F show opposite trends. The energy of state E remains unaffected by strain. This linear shift of energy is not unique to phosphorene. It is also observed in other semiconducting nanostructures.[18, 91, 92, 94-100, 110-113]
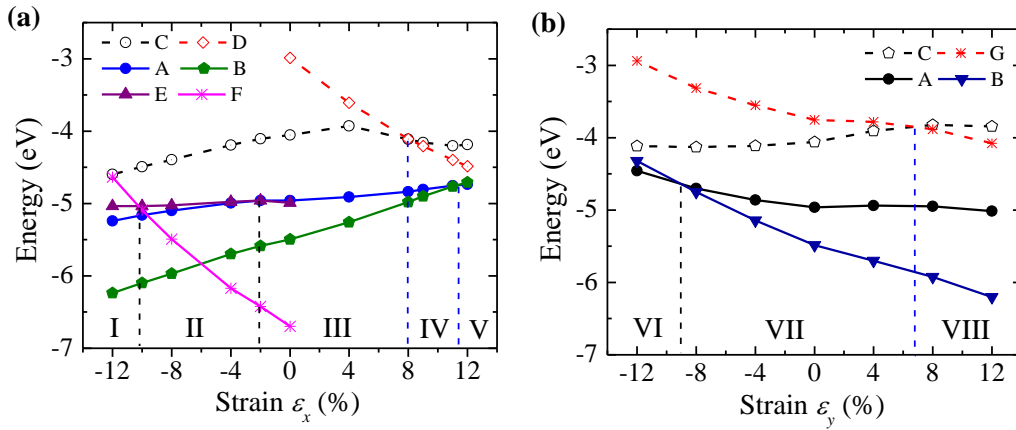
Figure III.6. The energies of the near-edge states A - G as a function of strain applied in the zigzag (left) and armchair (right) direction, respectively. The critical strains for the direct-indirect gap transition are determined by the energy crossover of competing states. In (a), the energy crossover of the competing VB states A, E, and F occurs at $\varepsilon_x = -2\%$, -10.2%, and +11.3% strains. The energies of the competing CB states C and D are equal at $\varepsilon_x = +8\%$ strain. In (b), the energies of the VB states A and B crosses at $\varepsilon_y = -9\%$, and two CB states C and G meets at $\varepsilon_y = +6.8\%$. Strain zones I-VIII are also labeled.

In Figure III.7, the conduction states were represented by hollow-dashed lines while valence states are given by solid lines. In Figure III.7 (a), state C represents the CBM

44

from -12% strain up to +8%, at which the energy of state D equals state C energy. From +8% to +12% strain, D has a lower energy than C, thus D represents the CBM. The energy crossover of these two states gives the critical strain +8% for the direct-indirect band gap transition.

For the valence bands, the two states A and B compete for the VBM at the positive strain, while three states A, E and F battle at compression. State A represents the VBM for positive strain up to +11.3%, where C catches up and becomes the VBM. For the negative strain, the energy of A was first exceeded by E at -2% strain and E becomes the VBM in the strain range from -2% to -10.2%. At -10.2% strain, F catches up and represents the VBM for compression higher than -10.2%.

In the case of strain ε_y in Figure III.7 (b), the energy crossover of two conduction states C and G occurs at +6.8% strain and that of two valence states A and B at -9%. In order to understand the different trends of states A-G in Figure III.7, their electronic orbitals, including charge distribution and wavefunction, were explored. The wavefunction character was examined by projecting the wavefunction onto s-, p-, and d-orbitals at each ionic site. It was found that states A and E are p_z-orbitals; B is p_y; C is dominated by p_z (86%) mixed with p_y; State D is dominated by p_y (56%) with a mixture of s-orbital; F is p_x; and G is dominated by p_x (59%) mixed with s-orbital. Their electron density contour plots and wavefunction character are presented in Figure III.8.

A general mechanism[92] was developed to explain the different energy shifts with strain based on the Heitler-London's exchange energy model (also mentioned in the introduction).[114] The different energy shifts with strain were found to be closely related to the bonding/anti-bonding nature of the orbitals.[92] In the Heitler-London model, the

energies of the bonding and antibonding states are given by the equations I.14 and I.15. Based upon the reasoning provided in the introduction, the exchange integral term H may be playing a dominant role in determining the different energy variation behaviors with strain in the bonding and antibonding situation. The exchange H is given by I.16 where the exchange H is contributed from either non-classical electron-electron (i.e. $\frac{1}{r_{12}}$, positive) or electron-ion interaction (i.e. $-\frac{1}{r_{2a}} - \frac{1}{r_{1b}}$, negative). For s-orbitals or any mixed orbitals in which electron density are not extremely localized, the contribution of the electron-ion interaction is dominated by the electron-electron interaction in the exchange H. As the atomic distance increases (corresponding to a positive tensile strain), the energy contributed from the electron-ion interaction increases more rapidly compared to the energy reduction of the electron-electron contribution (see equation (I.16)), which results in an increased value for H. An increased H value causes the bonding energy $E_{bonding}$ to increase and the antibonding energy $E_{antibonding}$ to decrease based in equations I.14 and I.15. These trends are represented by the schematic in Figure III.8 (h). For the case of non-bonding, in which the wavefunction overlap is minimal, the energy is expected to be insensitive to strain.
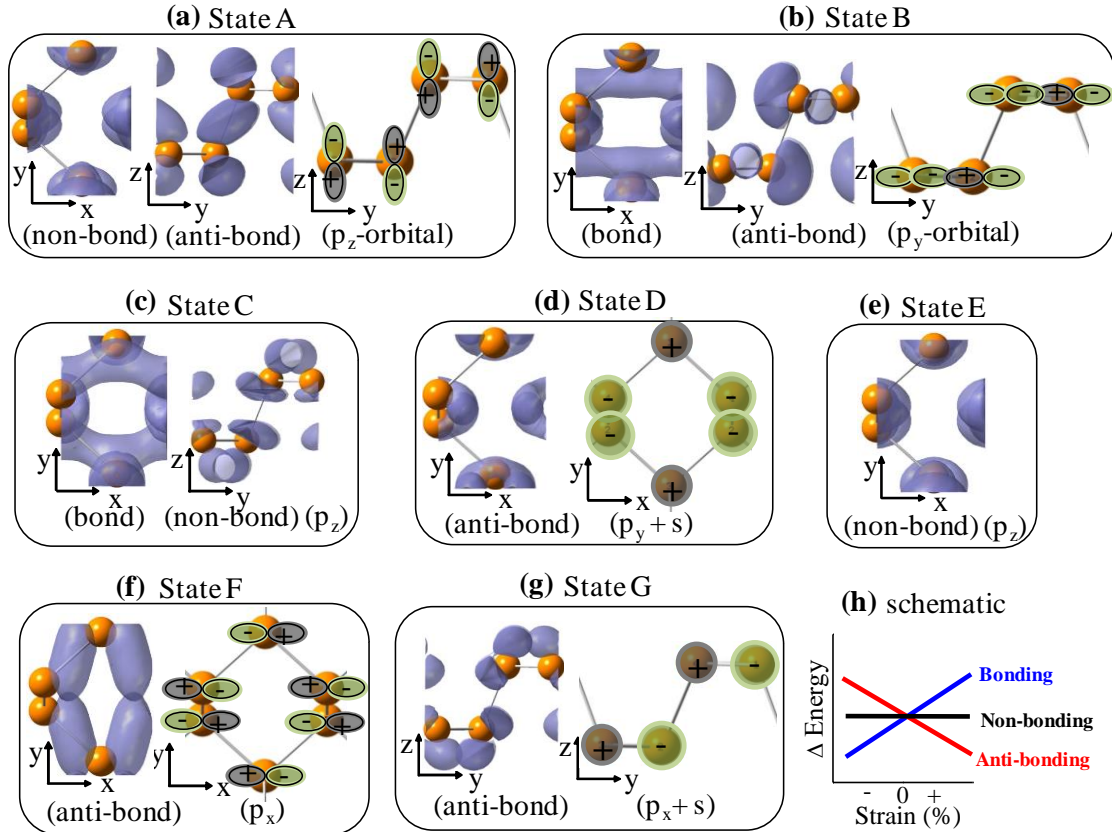
Figure III.7. (a)-(g) The electron density contour plots and schematic of the wave function character (i.e. the projected major orbital and sign of phase factor) of the near-band-edge states A - G in 2D phosphorene. Their dominant orbitals and bond status (in the horizontal axis) were listed at the bottom of each state. (h) Schematic of energy response to axial strain for three typical cases of bonding, non-bonding, and anti-bonding.

The bond nature of the electron density contour plots and wavefunction character in Figure III.8 is examined next. State A in Figure III.8 (a) suggests non-bonding in the x-direction and an anti-bonding character in the y-direction based on its sign of phase factor along the y direction. B is bonding in the x-direction while displaying anti-bonding in the y-direction. State C, which is dominated by p_z-orbital, illustrates a bonding nature in the x-direction while non-bonding in the y-direction. States D, E and F demonstrate anti-bonding, non-bonding and anti-bonding, respectively, in the x axis. State G is anti-bonding in the y-direction. State D is a mixture of p_y and s-orbitals. Since the overlap of the p_y orbital in the x direction is small, the s-orbital is plotted in Figure III.8 (d) to

47

determine its bonding/anti-bonding status in the x direction. The same case is applied to State G in Figure III.8 (g).

The bond nature of these seven states combined with the schematic in Figure III.8 (h) can be used to explain their energy variation in Figure III.7. For example, D is anti-bonding in the x direction and expected to decrease with tensile strain from Figure III.8 (h). This is in agreement with the curve of D in Figure III.7 (a). B is bonding in the x while anti-bonding in the y direction. According to Figure III.8 (h), its energy is expected to increase with ε_x while decrease with ε_y, which is consistent with Figure III.7. Other curves in Figure III.7 can be explained in the same manner.

The effective masses of the electron and hole can be readily calculated according to the formula $m^* = \hbar^2 \left(\frac{d^2E}{dk^2}\right)^{-1}$ (equation I.13) from the band structure. For relaxed phosphorene, the effective mass of the electron is predicted to be 1.24 m_e in the zigzag and 0.16 m_e in the armchair direction. The effective mass of the hole is 4.92 m_e in the zigzag and 0.15 m_e in the armchair direction. These calculated effective masses are in agreement with other theoretical work.[89, 90] The significantly smaller effective masses in the armchair direction suggest that charge carriers prefer transport in that direction.

The effective masses of the electron and hole as a function of both strains ε_x and ε_y are presented in Figure III.9. The effective masses of the electron and hole can be dramatically tuned by strain. In addition, it was found that the sudden jump (drop) in the effective masses occurs around the strain zone boundaries (i.e. critical strains) for the direct-indirect band gap transition. For example, in Figure III.9 (a), the effective mass of the electron in the zigzag direction is an order of magnitude bigger than that along the

armchair direction in Zones I, II, and III. At the zone boundary of III and IV, the effective

mass in the zigzag direction drops sharply while in the armchair direction jumps

suddenly. This sharp transition suggests the zigzag direction is favored for electron

transport.[89] Figure III.9 (b) shows that the hole prefers transport in the armchair direction

in Zones II-V. However, in Zone I, it favors the zigzag direction.
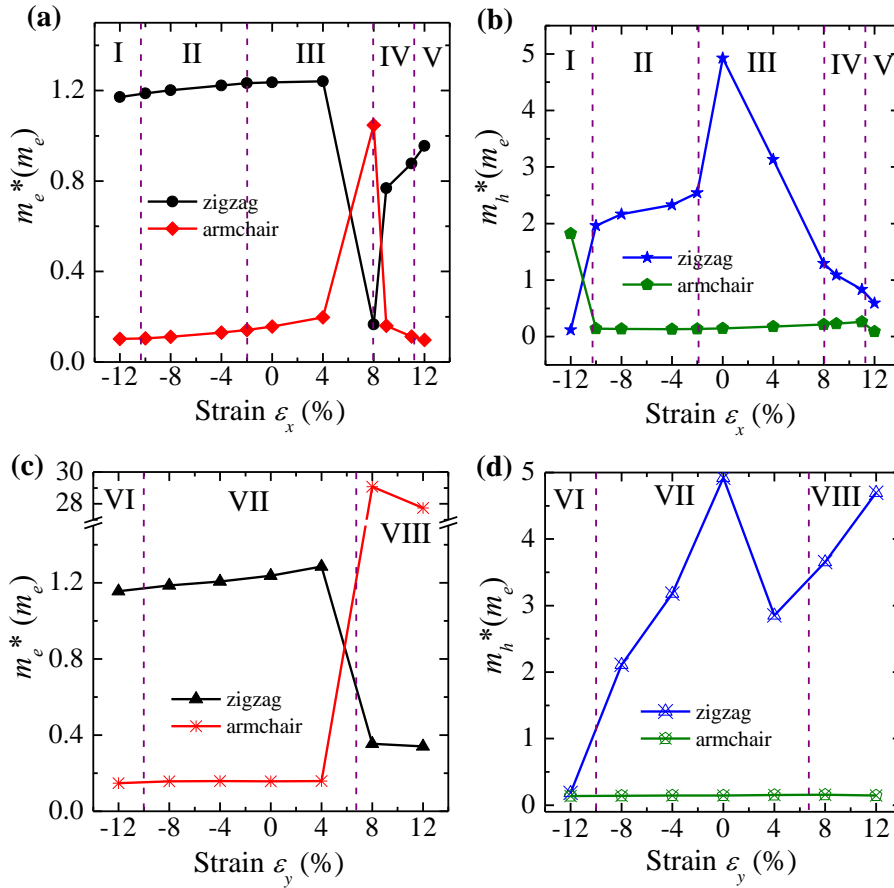
Figure III.8. Effective masses of the electron (left) and hole (right) as a function of strain ε_x (top) and ε_y (bottom). Five (three) strain zones for ε_x (ε_y) are also labeled. The sharp shift in effective masses occurs around the zone boundaries for the direct-indirect gap transition.

For the case of strain applied in the y direction, Figure III.9 (c) suggests the armchair

direction is favored for the electron transport in Zones VI and VII, while the situation

becomes opposite in Zone VIII. For the hole in Figure III.9 (d), the effective mass in the

armchair direction is insensitive to strain, while in the zigzag direction it experiences a

dramatic shift. The much smaller value of effective mass in the armchair direction

indicates the hole predominately prefers transport in the armchair direction in Zone VII

and VIII. However, the sharp reduction of the effective mass in the zigzag direction at

Zone VI makes this axis competitive with the armchair direction for the hole transport.

The effective mass presented in Figure III.9 is a direct consequence of the strain

effect on the band structure in Figures III.3 and III.4. In particular, the sharp change in

the effective masses results from the direct-indirect band gap transition. For example, to

understand the sudden shift of the effective mass at $\varepsilon_x = +8\%$ in Figure III.9(a), please

refer to the band structure of Figure III.3(h) along Γ to Y. Compared to +4% strain in

Figure III.3(g), the downward shift of state D at +8% strain largely reduces the band

dispersion at state C, thus increasing the effective mass of the electron dramatically at ε_x

$= +8\%$. When ε_x is bigger than +8%, the CBM is shifted away from C to D, thus the

effective mass of the electron was calculated from D, which has a much smaller effective

mass resulting from the more dispersive band structure. Another sharp shift in the

effective mass of the hole occurs at $\varepsilon_x = -12\%$ in Figure III.9 (b), which is a direct

consequence of Figure III.3 (a). At $\varepsilon_x = -12\%$, the energy of sub VB state F exceeds E

and becomes the VBM. The effective mass along the x direction is now calculated based

on this new state F instead of E. Similarly for the case of ε_y strain, the striking transition

of the effective mass of the electron from +4% to +8% strain in Figure III.9(c) results

from the +6.8% critical strain.

Using *ab initio* calculations, this work provided a detailed analysis of strain effects on

the electronic band structure of 2D phosphorene. This work observed that (1)

phosphorene can withstand a tensile stress and strain up to 10 N/m and 30%, respectively.

(2) The band gap of 2D phosphorene has direct-indirect-direct transitions with axial strain. (3) Five strain zones with distinct electronic band structure were identified and the critical strains for the zone boundaries were determined. (4) Although the DFT method is known to underestimate the band gap of semiconductors, it was proven to correctly predict the strain effect on the electronic properties with verification via the hybrid functional method. (5) The origin of the gap transition was revealed and a general mechanism was developed to explain the near-band-edge energy shifts according to the bond nature of their electronic orbitals. (6) In relaxed phosphorene, effective masses of the electron and hole in the armchair direction are an order of magnitude smaller than that of the zigzag direction suggesting that the armchair direction is favored for carrier transport. (7) Effective masses can be dramatically tuned by strain. (8) The sharp jump/drop in the effective masses occurs at the zone boundaries of direct-indirect gap transition.

Phosphorene has demonstrated superior mechanical flexibility and can hold a large tensile strain of 30%, which opens doors for applications in flexible displays. Having a direct band gap is essential for materials in optical applications. This work shows that a moderate -2% stain in the zigzag direction can trigger the direct-to-indirect band gap transition. Predicted strain Zones II, IV, VI, and VIII should be avoided for optical applications, due to the indirect band gap in the material within these strain zones. Carrier mobility is an essential parameter to determine performance of electronics and it is inversely dependent on the effective masses. This work demonstrated that strain can dramatically tune the effective masses, thus can be used to modify carrier mobility of phosphorene in electronics applications.

This work was a collaboration of Xihong Peng, Qun Wei, and Andrew Copple. The author of this dissertation was mostly responsible for the verification of strain effects on the band gap in the armchair and zigzag directions.

B. Edge Effects On Phosphorene Nanoribbons

Recently fabricated two dimension (2D) few-layer black phosphorus[68,] has drawn immediate attention to the society of material science.[15, 75, 88-89, 115-122] This material is chemically inert and has promising transport properties. It has carrier mobility up to 1000 cm^2/V·s and an on/off ratio up to 10^4 was achieved for the phosphorene transistors at room temperature.[67, 68] In addition, this material shows a finite direct band gap at the Γ point of the Brillouin zone[15, 67-68, 73-75] (in contrast to the vanishing gap in 2D graphene sheet), which creates potential for additional applications in optoelectronics.

Tailoring electronic properties of semiconductors has been critical for applications in electronics. A series of strategies were explored to engineer the band gap of phosphorene, for example, by utilizing multilayer structures,[68, 75] applying mechanical strains,[15, 89] forming nanoribbons [116, 118-120] or nanotubes.[116] For the phosphorene nanoribbons (PNRs), their electronic properties are dependent on the crystal orientation of the ribbons. For example, two typical crystal directions were generally explored, namely the armchair-PNRs (APNRs) and the zigzag-PNRs (ZPNRs). Tran and Yang[118] reported that the PNRs with the edge phosphorus atoms passivated using H are direct-gap semiconductors and their band gaps are a strong function of the ribbon width due to the quantum confinement effect. However, Guo *et al.*[116] found that the pristine ZPNRs are metals regardless of the ribbon width, while the pristine APNRs are semiconductors with

indirect band gaps. These distinct conclusions imply that the edges of the ribbons play a critical role on their electronic properties. Therefore, it is important to systematically study the edge effects on the PNRs, in particular, with several common chemical groups, such as -OH, -O, -S. In this work, we present detailed systematic analysis of the edge effects on the electronic band structure and density of states (DOS) of both APNRs and ZPNRs for a series of ribbon widths up to 3.5 nm. Our results suggest that the APNRs are semiconductors with either direct or indirect band gap depending on the edge functionalization groups, and the ZPNRs demonstrate either semiconductor or metallic behavior with different edge passivation.

The theoretical calculations were carried out using first principles density functional theory (DFT).[13] The Perdew-Burke-Ernzerhof (PBE) exchange-correlation functional[101] and the projector-augmented wave (PAW) potentials [102, 103] were employed. The calculations were performed using the Vienna Ab-initio Simulation Package (VASP).[50, 51] The kinetic energy cutoff for the plane wave basis set was chosen to be 500 eV. The energy convergence criteria for electronic and ionic iterations were set to be 10^{-5} eV and 10^{-4} eV, respectively. The reciprocal space was meshed at $14 \times 1 \times 1$ for the ZPNRs and $1 \times 10 \times 1$ for the APNRs using Monkhorst Pack meshes centered at Γ point. 21 K-points were included in band structure calculations from Γ to X for the ZPNRs and from Γ to Y for the APNRs. To simulate a ribbon, a unit cell with periodic boundary condition was used. A vacuum space of at least 20 Å was included in the unit cell to minimize the interaction between the system and its replicas resulting from the periodic boundary condition.
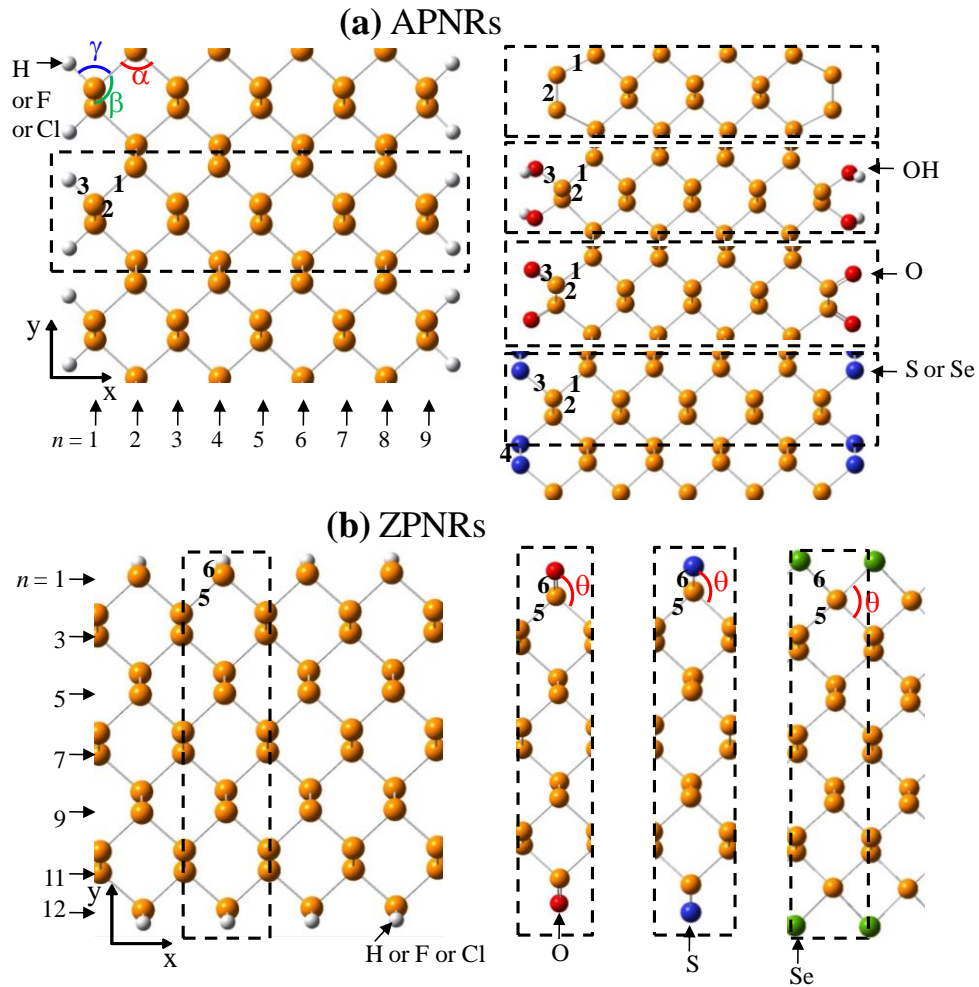
Figure III.10 Images of the APNRs and ZPNRs with different edge functionalization groups. (a) 9L-APNR with edge P atoms saturated using H (F or Cl), and hydroxyl group, double-bonded O, and bridge-bonded S (Se) atoms, respectively. (b) 12L-ZPNR with edge functionalized by H (F or Cl), double bonded O, S, and bridge-bonded Se atoms, respectively. The dashed rectangles indicate the unit cells.

The initial structures of monolayer phosphorene were obtained from bulk black phosphorus.[107] The 2D phosphorene has a puckered honeycomb structure with each phosphorus atom covalently bonded with three adjacent atoms. Our calculated lattice constants for bulk black phosphorus are $a = 3.307$ Å, $b = 4.547$Å, and $c = 11.210$ Å, and are in good agreement with experimental values[107] and other theoretical calculations.[68, 90] The relaxed lattice constants for monolayer phosphorene are $a = 3.295$ Å and $b = 4.618$ Å.

The APNRs and ZPNRs with different ribbon widths up to 35 Å were truncated from monolayer phosphorene along the y- and x-directions, respectively, as shown in Figure III.10. The width of a ribbon nL is referring to the number n of P atoms in the direction perpendicular to the ribbon direction (see Figure III.10). As an example, Figure III.10 demonstrates the snapshots of 9L-APNRs and 12L-ZPNRs. The edges of the PNRs were treated in eight different scenarios: no passivation (pristine) or bonded with H, F, Cl, OH, O, S or Se chemical species.

Table III.I The bond lengths b1-b6 and bond angles α-θ at the edges of the PNRs with different edge chemical groups. The bond lengths and angles were denoted in Figure III.10. As a reference, the corresponding bond lengths/angles in monolayer phosphorene were also listed.

system	9L-APNR							12L-ZPNR		
	b1 (Å)	b2 (Å)	b3 (Å)	b4 (Å)	α (°)	β (°)	γ (°)	b5 (Å)	b6 (Å)	θ (°)
monolayer	2.22	2.26	n/a	n/a	95.9	104.1	n/a	2.22	n/a	104.1
pristine	2.23	2.07	n/a	n/a	111.1	119.1	n/a	2.14	n/a	n/a
H	2.22	2.25	1.44	n/a	95.7	103.2	93.1	2.23	1.44	99.3
F	2.23	2.25	1.63	n/a	94.9	98.3	98.3	2.22	1.64	106.0
Cl	2.24	2.26	2.08	n/a	92.7	95.9	101.1	2.23	2.08	107.3
OH	2.23	2.24	1.68	n/a	94.9	99.0	100.1	2.22	1.68	110.7
O	2.27	2.25	1.49	n/a	99.5	106.7	109.2	2.25	1.50	116.4
S	2.23	2.25	2.11	2.10	97.0	105.0	99.5	2.28	2.00	106.3
Se	2.23	2.24	2.28	2.38	95.3	102.9	100.0	2.29	2.39	89.3

We explored the structural configuration at the edges for the PNRs. For example, six bond lengths labeled as b1 – b6 and four bond angles indicated as α, β, γ and θ in Figure III.10 were calculated and reported in Table III.I. There is negligible change in the bond length b1 (between the two P atoms near the edge of the 9L-APNR) for all eight different edge groups, indicating that the distinct edge functionalization groups only affect the

55

geometry on the very edge of the ribbons. The P-P bond b2 on the very edge for the pristine case experiences a considerable reduction from 2.26 Å (of the 2D phosphorene) to 2.07 Å, due to its edge dangling-bond reconstruction. The variation in the bond length b3 between the P atoms and the edge species is expected: larger edge chemical species yields a longer bond length. The bond b3 is sufficiently large for the edge S (Se) case, such that two S (Se) atoms in the neighbored simulation cell form a bond, labeled as b4 in Figure III.10 (a). The bond angles α and β both increase largely for the pristine case due to the reconstruction of the edge P-P bond.

For the ZPNRs, the bond lengths b5 and b6 show similar variations with the edge functionalization groups as the b2 and b3 in the APNRs, respectively. The significantly reduced bond angle θ in the Se case from 104.1° (of the 2D phosphorene) to 89.3° results from the special bridge-bonding configuration as shown in Figure III.10 (b). We also checked this bridge-bonding arrangement for both O and S edges and found that these two species prefer to bond to one P atom rather than the bridge-bond to two P atoms, as shown in Figure III.10 (b). This gives much shorter bond length b6, 1.50 Å and 2.00 Å for the O and S cases, respectively, comparing to 2.39 Å in the Se edge.
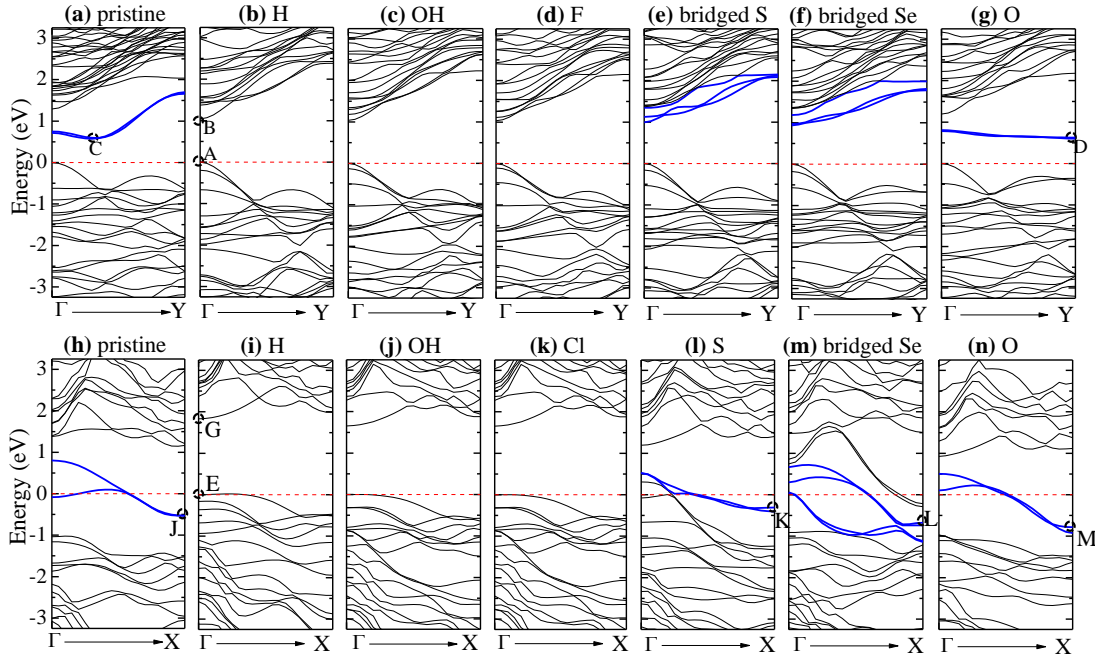
Figure III.11 Band structures of the APNRs and ZPNRs with different edge chemical groups. Top is for the 9L-APNRs and bottom for the 12L-ZPNR. The Fermi level is aligned at zero. The states brought by the edge P, O, S, and Se atoms within the band gap are indicated in blue color.

The band structures of the PNRs with the eight different edge functionlization groups were calculated. As an example, Figure III.11 presents the band structures of the 9L-APNRs and 12L-ZPNRs. Since the edge groups F and Cl show similar effects on the band structure, we only plot the F-edge case for the APNR and the Cl case for the ZPNR in Figure III.11. It is clear that the APNR is a semiconductor. The band gap is defined as the energy difference between the conduction band minimum (CMB) and valence band maximum (VBM). For the pristine and O-edge cases, the APNR shows an indirect band gap, while other functionalization groups demonstrate a direct band gap. For the pristine and O-edge cases, the CBM, which is contributed from the edge P and O atoms, respectively (see below Figure III.12), is not located at the Γ point, while the VBM is at Γ, which gives an indirect gap. However, for the cases with the edge H, OH, F(Cl), both the CBM and VBM are contributed by the non-edge P atoms (i.e. intrinsic states) in the

ribbon and located at Γ, which gives a direct band gap. A slightly different situation

occurs for the APNRs with the edge S (Se) atoms, in which the conduction bands are

mainly contributed by the edge S (Se), while the CBM is still located at Γ and results in a

direct band gap.
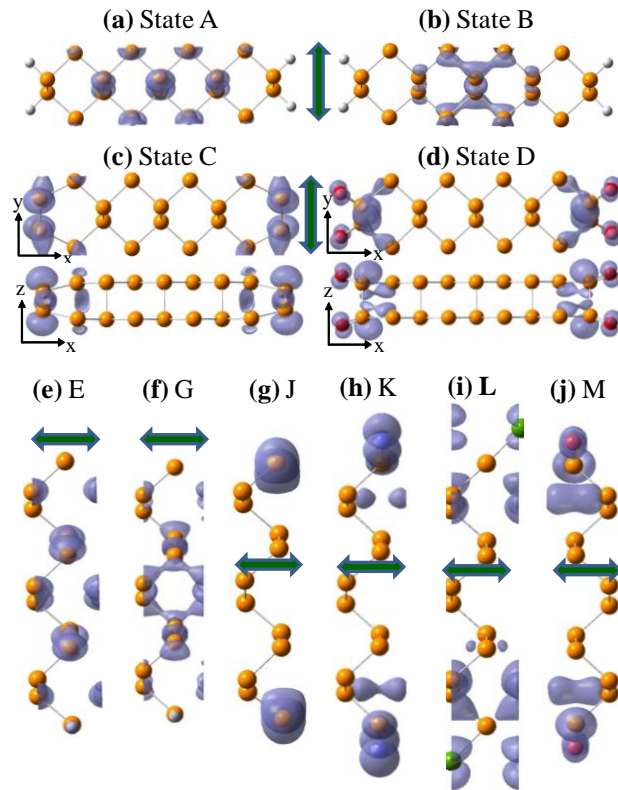
Figure III.12 The electron density contour plots of near-Fermi-level states A-M. The vertical and horizontal arrows indicate the armchair and zigzag ribbon directions (periodic boundary), respectively.

On the other hand, the ZPNR shows a dissimilar behavior. The ribbon demonstrates

either semiconductor or metallic behavior as shown in Figure III.11 (h)-(n), in

dependence on the edge functionalization groups. The edge chemical groups can be

classified into two distinct families. Family 1 includes the H, OH, F and Cl edges and

Family 2 consists of the pristine, O, S and Se cases. For Family 1 edges, the ZPNRs are

semiconductors with a direct band gap at Γ. Their CBM and VBM are the intrinsic states

from the non-edge P atoms in the ribbon (see below Figure III.12). However, for Family

2 edges, the ribbon shows metallic behavior. The electronic states contributed by the edge atoms are located around the Fermi level and close up the band gap.
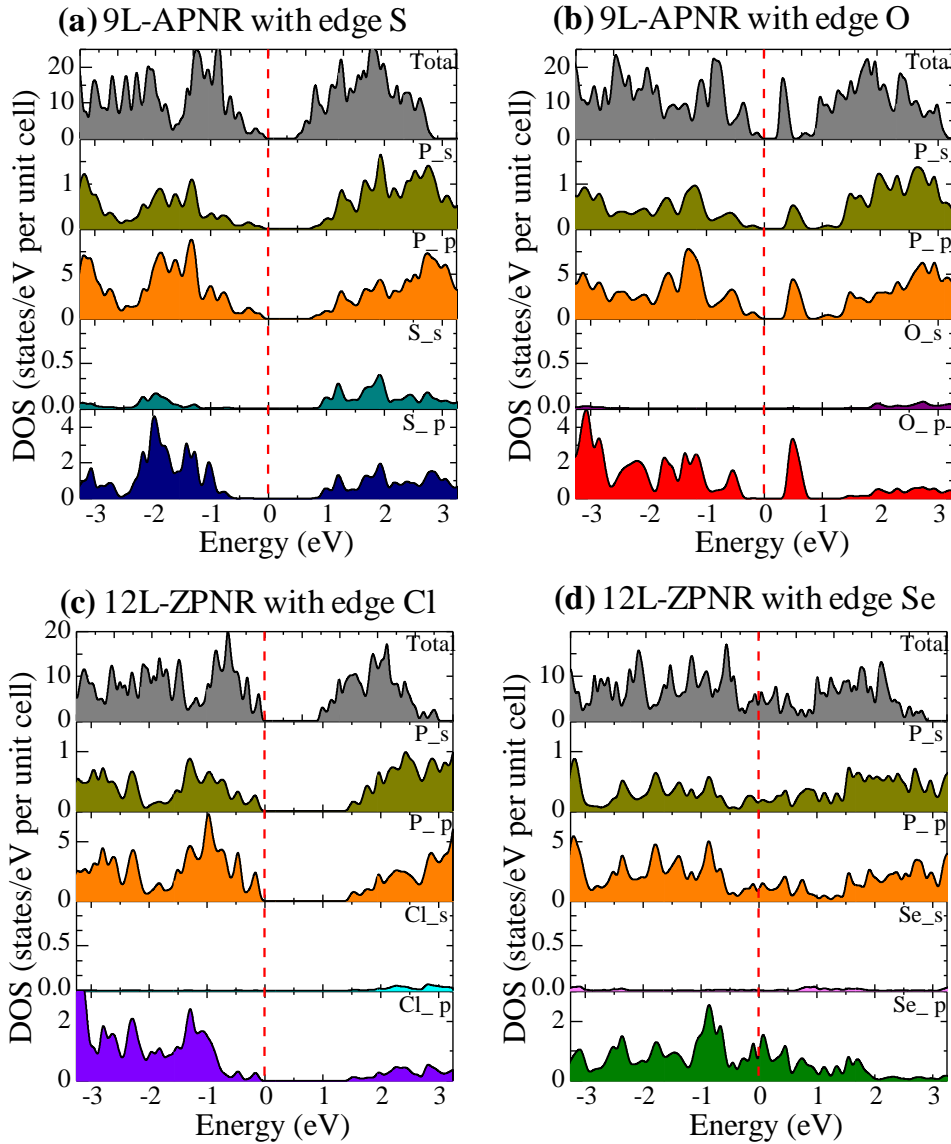
Figure III.13 The total, s- and p-orbital projected density of states. The DOS of the 9L-APNR with the edge functionalized by (a) S and (b) O atoms. The DOS of the 12L-ZPNR with the edge saturated by (c) Cl and (d) bridge bonded Se atoms. The Fermi level is aligned at zero.

The DOS of the studied PNRs was also calculated. As an example, Figure III.12 presents the total, s- and p-orbital projected DOS of the 9L-APNRs and 12L-ZPNRs. The DOS of the 9L-APNR with the edge S (O) passivation in Figure III.13 suggests that the ribbons are semiconductors, in which the conduction band (CB) was mainly contributed

by the p-orbitals of the edge P and S (O) atoms while the VBM is located at the p-orbitals of the P atoms in the ribbons. For the 12L-ZPNR with the edge Cl in Figure III.13 (c), the band gap of the ribbon is determined by the intrinsic states of P and the Cl states being far away from the band gap. In the metallic 12L-ZPNR with the bridge-bonded Se in Figure III.12 (d), the p-orbitals of the Se and P atoms form bonds which close up the gap.

The near-band-edge states A – M (labeled in Figure III.11) were explored and their electron density contour plots are presented in Figure III.13. States A and B are the VBM and CBM of the 9L-APNR with the edge H atoms. The wave function of states A and B are primarily located in the phosphorus atoms within the ribbon and the edge P and H atoms have little contribution. It was found that State A and B also represent the VBM and CBM of the 9L-APNR with other edges in Family 1 (i.e. F, Cl and OH). State C is the CBM of the pristine 9L-APNR. From the electron density contour plot in Figure III.12 (c), it is clear that the charge is primarily located at the edge P atoms. State D is the CBM of the 9L-APNR with the edge O and the charge is distributed mainly on the edge P and O atoms. Similar edge states within the band gap were also found for the S and Se cases.

In the 12L-ZPNRs, the electronic states E and G are denoted as the VBM and CBM with the edge H atoms and they are intrinsic states contributed by the non-edge P atoms. It was found that the VBM and CBM with other Family 1 edges are the same State E and G, respectively. However, for the pristine, S, Se and O cases (Family 2), the charges of states J, K, L and M are primarily located on the edge P and chemical groups.

To understand why Family 2 structures bring edge states within the band gap while Family 1 edges do not, we examined the characteristics of the electronic orbitals of the

near-gap states. Family 1 edge species form a saturated bond with the P atoms and the energy associated with this saturated bond is far below the Fermi level. For example, the energy associated with the P-F bond in the 9L-APNR is 4.12 eV below the Fermi energy and that of the P-O bond in the case of edge OH group is 2.09 eV below the Fermi level. However, in Family 2 cases, the P atoms do not form a saturated bond with the edge species. Moreover, these unsaturated bonds are particularly weak due to their special electronic orbital orientations. For instance, the edge reconstructed P-P bond in the pristine ribbon is nearly in the ribbon plane (i. e. the xy-plane). However, the p-orbitals of the two P atoms are along the z-direction (i.e. p_z-orbital). And the p_z-orbitals form a relatively weak P-P bond in the xy-plane due to a minimal overlap of the wavefunction. A similar situation was found for the O, S and Se cases. For example, in Figure III.13 (d) the p_z-orbitals of the edge O and P atoms cause a weak P-O bond in the ribbon plane (i.e. the xy-plane). These weak unsaturated bonds bring the edge states within the band gap for Family 2 cases. It is interesting to note that the bridge-bonded Se atoms in the ZPNR appear to form a saturated bond with two P atoms. However, their p_z-orbitals make these P-Se-P bonds in the ribbon plane relatively weak, and such weak bonds brings edge states within the band gap to close the gap.
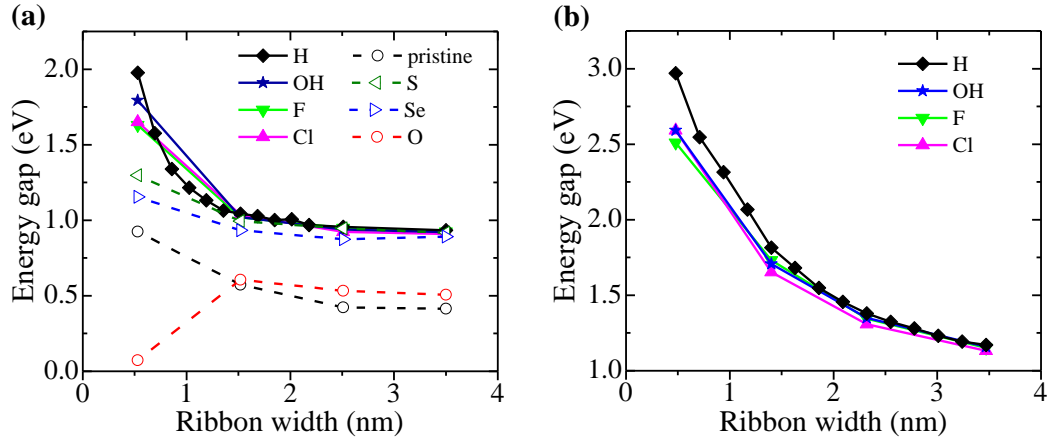
Figure III.14 The band gap of the (a) APNRs and (b) ZPNRs as a function of ribbon width. Family 1 edges are plotted using solid lines while Family 2 edges are denoted with dashed lines.

The band gap of the APNRs and semiconducting ZPNRs with the ribbon width up to 35 Å were calculated and presented in Figure III.14. For the APNRs in Figure III.14 (a), the band gap of Family 1 cases increases rapidly with reducing width of the ribbon. Note from the above discussion, the band gap of Family 1 is determined by the intrinsic electronic states of phosphorus atoms. The scaling of the band gap with the ribbon width d obeys the usual $1/d^2$ relation according to quantum confinement, which is consistent with literature.[118] Given the same ribbon width, the band gap of Family 2 ribbons is generally smaller than that of Family 1. This is because Family 2 cases bring edge states within the band gap, thus largely reducing the gap. The significantly smaller band gap of the 3L-APNR with the edge O results from a structural distortion of this ultra-narrow ribbon. For the ZPNRs in Figure III.14(b), the four Family 1 ribbons have very similar behavior, and the gap scaled as $1/d$, in agreement with Tran and Yang's prediction.[118] Family 2 ZPNRs show metallic behavior, thus the gap is zero.

In summary, we employed first principles DFT calculations to study electronic properties of the phosphorene nanoribbons with the edge functionalization using different chemical groups. It was found that the APNRs are semiconductors for all edge groups

considered in this work. However, the ZPNRs demonstrate either semiconducting or metallic behavior. The CBM and VBM of the APNRs and ZPNRs with the edge H, F, Cl, and OH groups (Family 1 edges) are contributed by the intrinsic electronic states of non-edge phosphorus atoms, and the edge species have negligible contribution to the wavefunctions of the CBM and VBM. Therefore, the ribbons in this family are semiconductors with a direct band gap. However, the APNRs and ZPNRs in the pristine, O, S and Se cases (Family 2 edges) display edge states within the band gap, which cause a reduced band gap in the APNRs and metallic behavior in the ZPNRs. These edge states in Family 2 ribbons originate from their weak unsaturated bond with the P atoms.

This work was a collaboration between Xihong Peng, Andrew Copple, and Qun Wei. The author of this dissertation was mostly responsible for some verification of strain effects on the band gap APNRs and ZPNRs, as well as observing any significant structural changes to the PNRs with strain.

Chemical Scissors Effect and Future Work. While working on these studies, passivation of the armchair phosphorene nanoribbons with certain edge elements (most notably H) created a splitting effect in the relaxation phase of calculations. Upon further study of this phenomenon, it became apparent that the chemical addition of certain elements could be intentionally used to cut sheets of phosphorene along the armchair direction, producing ZPNRs.[123] This work was also confirmed in these studies. Future studies of PNRs could include few-layer PNRs, defects, larger supercells for greater relaxation of the system, as well as substrate interface behavior or non-uniform strain application. However, some of these studies might be easier to complete outside of DFT. The next material presented in this work begins with the study of III-V nanowires.

Chapter IV. III-V NANOWIRES

A. Size And Strain Engineering Band Gap

Experimental studies have shown that while GaAs naturally exists in the Zinc-Blende structure, when creating nanowires of sufficiently small size, the wurtzite structure can also be observed.[9, 124, 125] This particular part of the study is focused on the unique behavior of wurtzite GaAs nanowires, as well as their Zinc-Blende and InAs counterparts. The research from both GaAs nanowire publications is presented below[91, 92] and results for InAs were similar and thus unreported.

One dimensional nanostructures, such as nanowires, of group III-V semiconductors have drawn extensive research interests in recent years. They are expected to play important roles as functional components[126] in future nanoscale field effect transistors,[127] high efficiency photo detectors,[1, 2] light emitting diodes,[128] photovoltaic cells,[129] medicine sensors,[130] etc. In particular, GaAs has been considered as a promising channel material for the high speed NMOS beyond Si based technology. GaAs has two different crystal structures zinc blende (ZB) and wurtzite (WZ) phases. In bulk GaAs, ZB phase is energetically more favorable than WZ. In nanoscale, however, WZ phase was observed more often experimentally. Theoretical work,[124] including *ab-initio* calculations, has shown that at small size WZ structure is energetically more favorable,[9, 124, 125] and the interface energy may also facilitate the growth of WZ structure.[131] Recent experiments have shown it is possible to grow GaAs nanowires in ZB,[132] WZ,[133] and mixed crystal phases.[134]

While bulk GaAs (both ZB and WZ) has a direct band gap, GaAs nanowires may demonstrate an indirect gap when the diameter of nanowire is sufficiently small.[135, 136]

This band gap transition could fundamentally alter the electronic properties of nanowires. In addition to size, strain has become a routine factor to engineer band gaps of semiconductors in the field of microelectronics. Researchers have theoretically demonstrated the modulated band gap by external strains in a variety of systems such as pure Si[11] and Ge[10] and Si/Ge Core-shell nanowires.[97] It would be very interesting to investigate strain effects on the band structure of WZ GaAs nanowires and examine if the direct-indirect band gap transition can be engineered for applications.

The *ab-initio* density functional theory (DFT)[13] calculations were carried out using VASP code[50, 51]. The DFT local density approximation and the projector-augmented wave potentials[102, 103] were used along with plane wave basis sets. The kinetic energy cutoff for the plane wave basis set was chosen to be 300.0 eV. The energy convergence criteria for electronic and ionic iterations are 10^{-4} eV and 0.03 eV/Å, respectively. The GaAs nanowires were generated along the [0001] direction (i.e. *z*-axis) from bulk WZ GaAs with different diameters in the wire cross section (see Figure IV.1). The dangling bonds on the wire surface are saturated by hydrogen atoms. The Ga 3d, 4s, 4p, As 4s, 4p and H 1s electrons are treated as valence electrons. The reciprocal space of a nanowire is sampled at 1×1×6 using Monkhorst Pack meshes. In band structure calculations, a total of 21 k-points were included along the K vector direction Γ (0, 0, 0) to X (0, 0, 0.5). The initial axial lattice constant in GaAs nanowires is set to be 6.5083 Å, taken from the relaxed lattice constant *c* of bulk WZ GaAs. In addition to the axial lattice constant, the lateral length of the simulation cell is chosen so that the distance between the wire and its replica (due to periodic boundary conditions) is more than 15 Å to minimize the interactions between the wire and its replica. The axial lattice constant in a WZ GaAs

wire is optimized through the technique of total energy minimization. Once the optimized geometry of a wire is obtained, we applied uniaxial tensile/compressive (i.e. positive/negative) strain to the wire by scaling the axial lattice constant of the wire. For a wire under each strain, the lateral x and y coordinates are further optimized through energy minimization. The band gap of a nanowire is defined by the energy difference between the conduction band minimum (CBM) and the valence band maximum (VBM).
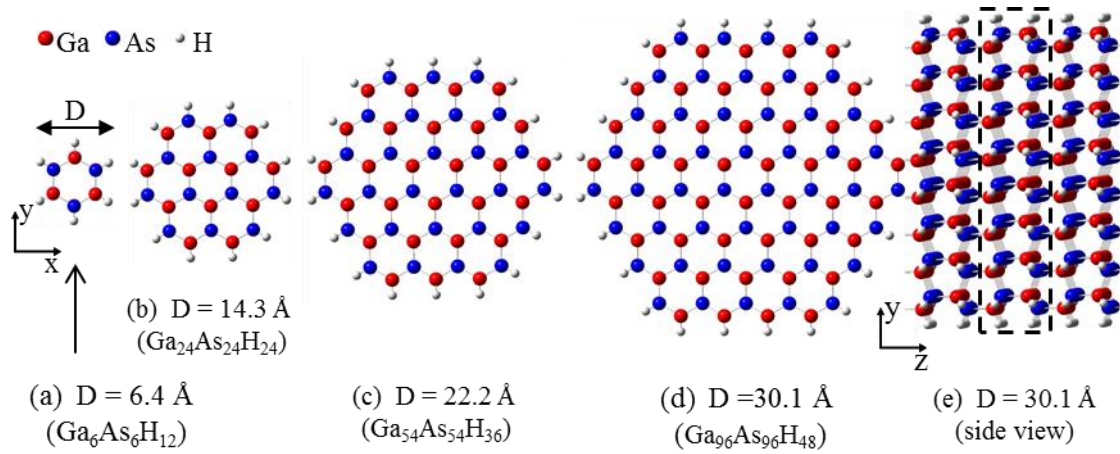
Figure IV.1 Images of simulated GaAs wurtzite nanowires. The diameter and composition of each wire in a unit cell is given at the bottom. The dashed rectangle in (e) indicates a unit cell.

Four different sizes of WZ GaAs nanowires in the [0001] direction with a hexagonal cross section were studied and the corresponding diameters are 6.4 Å, 14.3 Å, 22.2 Å and 30.1 Å, as shown in Figure IV.1. It was found that the optimized axial lattice constant of the nanowires are the same as its bulk lattice constant (c=6.5083 Å), except for the smallest wire. For the smallest wire, the lattice constant is 6.4933 Å, implying a very slight contraction of 0.23% compared to the bulk value.

It is known that bulk WZ GaAs has a direct band gap[124, 137] with both VBM and CBM located at Γ. However, our calculated band structures of thin WZ GaAs nanowires demonstrate an indirect band gap, shown in Figure IV.2 (a)-(c). VBM of the three smaller nanowires are all at Γ and CBM are located at the CB valley along the Γ-X direction.

This CB valley could be related to M-L valleys of bulk WZ GaAs.[124] For the larger

nanowire with a diameter of 30.1 Å, the band structure demonstrates a direct band gap

with both VBM and CBM located at Γ, shown in Figure IV.2 (d). The indirect-direct

band gap transition in the WZ GaAs nanowires occurs in the size range 22 ~ 30 Å. From

Figure IV.2, one also can find that the band gap of the nanowires increases with the

reduction of the wire diameter, which is mainly due to quantum confinement effects.
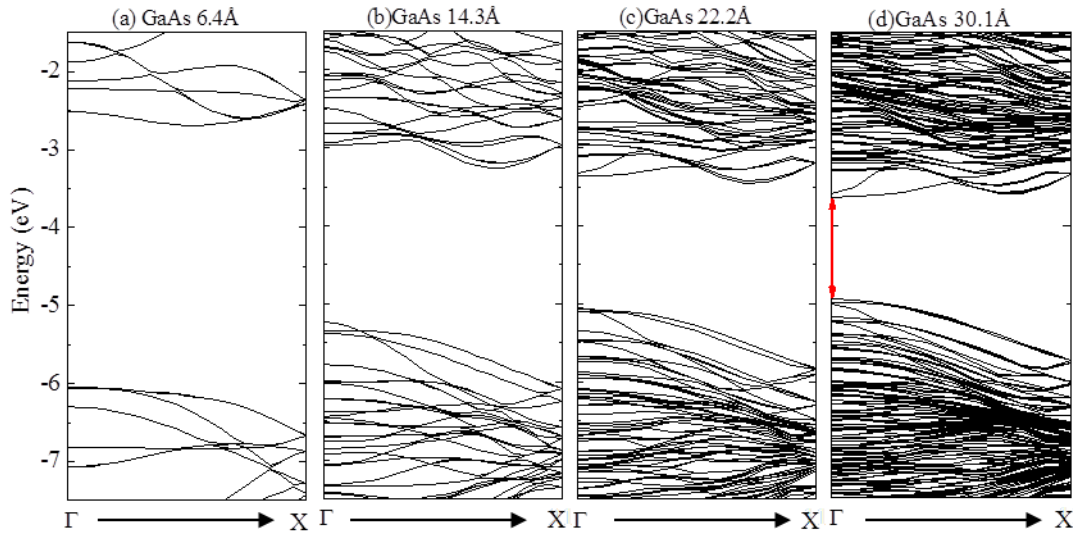
Figure IV.2 Band structures of geometrically optimized wurtzite GaAs nanowires with various diameters. Energies are referenced to vacuum level. There is a conduction band valley away from Γ in all nanowires.

To further estimate the size of the nanowire in which the indirect-to-direct-gap

transition occurs, we plotted energies of three states, namely VBM, conduction band

(CB) at Γ and CB at the valley, as a function of the diameter of the wires, presented in

Figure IV.3 (a). It's shown that the energy of VBM (E_{VBM}) increases while both energies

of CB at Γ ($E_{CB-\Gamma}$) and at the valley (E_{CB-v}) reduce with increasing size of the nanowires.

For the three smaller wires, the energy of CB at the valley (E_{CB-v}) is lower than the

energy of CB at Γ ($E_{CB-\Gamma}$), indicating an indirect band gap. However, for the largest wire,

$E_{CB-\Gamma}$ becomes lower, therefore having a direct band gap. The indirect-to-direct-gap

68

transition size was estimated to be ~28 Å, from the crossover of $E_{CB-\Gamma}$ and E_{CB-v} in Figure IV.3 (a). This critical lateral size to trigger the direct-indirect band gap transition in WZ GaAs nanowires is smaller than that of the ZB nanowires (~40 Å) reported by Persson and Xu, using tight-binding calculations.[135]
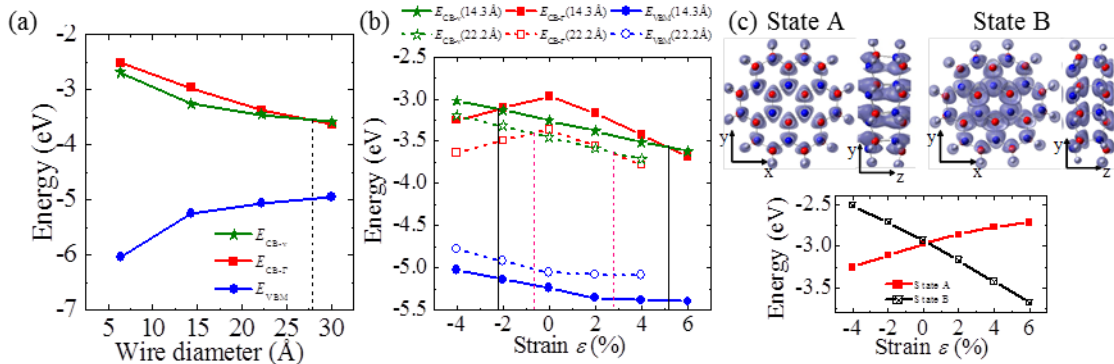
Figure IV.3 The calculated energies for the valence band (VB) at Γ (i.e. VBM), conduction band (CB) at Γ and the CB valley, as a function of (a) the size of the nanowires and (b) the uniaxial strain. (c) The two competitive states (A and B) for CB at Γ and their energy trends with strain. The nanowires are along the z-direction.

Effects of uniaxial strain on the band structures of WZ GaAs nanowires were further studied. It was found that the band gap can be significantly tuned by uniaxial strain. For the thin nanowires with an indirect band gap, a suitable uniaxial strain can tune the gap into a direct band gap. Taking an example of the nanowire with a diameter of 14.3 Å, the effect of uniaxial strain on the band structures were presented in Figure IV.3. Without strain, the wire has an indirect band gap with CBM located at the valley in Figure IV.3 (c). The indirect/direct band gap nature is determined by the values of $E_{CB-\Gamma}$ and E_{CB-v}. With a tensile uniaxial strain, both $E_{CB-\Gamma}$ and E_{CB-v} decrease. However, the downward shift of $E_{CB-\Gamma}$ is larger than that of E_{CB-v}, as shown in Figure IV.4 (d)-(f). For example, when a tensile strain of 6% was applied to the wire, $E_{CB-\Gamma}$ is lower than E_{CB-v}, suggesting a direct band gap. On the other hand, when a compressive strain was applied, $E_{CB-\Gamma}$ experiences a downward shift while E_{CB-v} increases, as shown in Figure IV.4 (a) and (b).

The band gap becomes direct when $E_{CB-\Gamma}$ is lower than E_{CB-v}, for example, with a -4% strain.
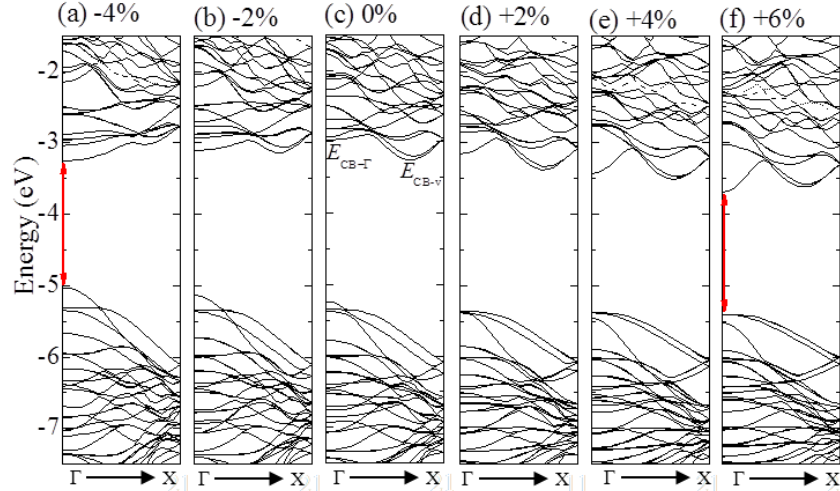
Figure IV.4 Band Structure of wurtzite GaAs nanowire with a diameter of 14.3 Å under uniaxial strain. Positive and negative values of strain refer to tensile and compressive strain, respectively. Energies are referenced to vacuum level. Indirect-to-direct band gap transition occurs when expansion beyond 4% and compression larger than 2%. $E_{CB-\Gamma}$ and E_{CB-V} are energies of the conduction band at Γ and at the valley, respectively.

This indirect-to-direct band gap transition manipulated by strain was also observed for the nanowire with a diameter of 22.2 Å. However, the critical strain to trigger the band gap transition for the 22.2 Å nanowire is smaller than that of the 14.3 Å wire. To illustrate this, three energies E_{VBM}, $E_{CB-\Gamma}$ and E_{CB-v} are plotted as a function of strain for these two nanowires and presented in Figure IV.3 (b). Generally for both wires, E_{CB-v} changes linearly with strain, decreasing with tensile strain while increasing with compression. However, $E_{CB-\Gamma}$ has its maximized value at 0% strain and drops with both tensile and compressive strain. The crossover of these two energies $E_{CB-\Gamma}$ and E_{CB-v} is the critical strain for the indirect-to-direct band gap transition. It is clear, from Figure IV.3 (b), the critical strains are roughly -2.2% and +5.2% for the nanowire with a diameter of 14.3 Å. For the larger wire with a diameter of 22.2 Å, the critical strain to trigger the indirect-direct gap transition is approximately -0.8% and +2.8%. For the thinnest

nanowire with a diameter of 6.4 Å, no indirect-to-direct band gap transition was found within the uniaxial strain of ±6% considered in this work.

As shown in Figure IV.3 (b), the nearly *linear* shift of E_{CB-v} and E_{VBM} with strain was also observed in other semiconducting nanostructures.[10, 11, 84, 94, 95, 138] More interesting in Figure IV.3 (b) is the $E_{CB-\Gamma}$ shift with strain, which is maximized at 0% strain and drops at both tensile and compressive uniaxial strains, demonstrating a *non-linear* behavior. To understand this unique behavior which essentially determines the band gap transition, we further explored the detailed wavefunction and electron density of the state CB at Γ with different values of strain. We found that CB at Γ does not correspond to the same state under different strains. It is a result of a competition between two conduction band states (A and B). To illustrate this, we take the wire with a diameter of 14.3Å as an example (note that the following general conclusions are also valid for the larger wire with a diameter of 22.2 Å). Figure IV.3 (c) displays the electron density contour plots of these two competitive states A and B and their energy shifts with strain. Both energy shifts of states A and B show a *linear* behavior with strain, in which the energy of state A increases with tensile strain while state B demonstrates an opposite trend. It's clear that, without strain and under negative strain, the energy of state A is lower than that of state B, thus state A represents the conduction band at Γ. However, with a tensile strain, state A has a higher energy than B; therefore state B is the conduction band.

To further understand the two distinct *linear* trends of state A and B in Figure IV.4 (c), their wavefunctions were projected onto *s*, *p*, and *d* orbitals and it was found that both states are dominated by the *s*-orbital (>90%). However, the bonds along the *z*-direction show distinct bonding and anti-bonding characteristics for state A and B, respectively

71

(see the electron contour plots). For state A, compressive uniaxial strain along the z-direction makes these bonding lengths shorter and makes the electron cloud more effectively shared by nuclei, thus decreasing the electron-nuclei Coulomb potential energy.[95] In contrast, tensile uniaxial strain moves electron cloud farther away from the nuclei and increases the Coulomb potential energy. This explains the linear relation of the energy of state A with strain in Figure IV.3 (c). For state B, the anti-bonding characteristics makes the Coulomb energy between the electron and the nuclei less sensitive to uniaxial strain.[95] However, the anti-bonding characteristics suggests that the nodal surfaces of the positive and negative values of the wavefunction are perpendicular to the z-direction and a compressive uniaxial strain reduces the distance between the nodal surfaces, therefore kinetic energy associated with the electron transportation between atoms increases.[138-140] In contrast, a tensile strain increases the nodal surfaces thus reducing the associated kinetic energy.

In summary, thin wurtzite GaAs nanowires along the [0001] direction with a diameter up to 30 Å were studied using DFT calculations. It was found that (1) the band gap of the GaAs nanowire increases when the size of the nanowire decreases due to the quantum confinement; (2) the band gap of the WZ GaAs nanowires experiences a transition from direct to indirect when the diameter of the nanowire is smaller than 28 Å; (3) uniaxial strain can significantly tune the band structure of the nanowires; (4) the indirect band gap of the ultrathin nanowire can be tuned to a direct band gap with an appropriate tensile/compressive uniaxial strain; (5) thinner nanowires require a larger critical strain to trigger the indirect-to-direct band gap transition.

This work was a collaboration between Xihong Peng and Andrew Copple. The author of this dissertation was responsible for the majority of the simulation work present in this section B of chapter IV. After the success with the first study on III-V nanowires, additional work expanded into zinc-blende nanowires and applied strain in directions that were not uniaxial.

B. Exploring the Direct-Indirect Band Gap Transition

Tailoring electronic properties of semiconductor nanostructures has been critical for nanoscale applications.[1, 2, 91, 127-130, 141, 142] Among various tailoring methods, size and surface passivation/functionalization are most commonly adopted. Recently, mechanical strain[10, 11, 82, 100] was also found to have great potential to tune electronic properties of nanoscale semiconductors and is receiving an increased attention. Adventitious strain is almost unavoidable experimentally, but a more interesting case comes from intentionally introduced and controlled strains. One of the most prominent examples is the greatly enhanced mobility in the strained Si nanochannel.[143, 144]

Recently, it was demonstrated that band gaps of semiconductor nanostructures can be modulated effectively under moderate strain.[10, 11, 84, 91, 100, 138, 145, 146] The approaches introducing strain include lattice mismatch, functional wrapping,[78, 79] material doping,[80, 81] and direct mechanical application.[82] It was also found that nanostructures maintain integrity under a much higher strain than their bulk counterpart,[83, 84] which dramatically expands the strength of applicable strain to nanostructures.

One dimensional (1D) nanostructures, such as nanowires, of group III-V semiconductors have drawn extensive research interests in recent years. They are

expected to play important roles as functional components in future nanoscale transistors,[127] optical devices,[1, 128] photovoltaic cells,[129] biosensors,[130] etc. In particular, GaAs has been considered as a promising channel material for high speed NMOS beyond Si based technology.

GaAs has two different crystal structures – zinc blende (ZB) and wurtzite (WZ). In bulk, ZB phase is energetically more favorable than WZ phase. In nanoscale, however, WZ phase was observed more often experimentally. Theoretical and experimental work has shown that at small size both WZ and ZB structures can be formed.[9, 124, 131-134, 147]

While bulk GaAs (both ZB and WZ) has a direct band gap, a GaAs nanowire may demonstrate an indirect gap if its diameter is sufficiently small.[92, 135, 136] This band gap transition could fundamentally alter the electronic properties of GaAs nanowires, and thereby affects the function of the material. Recently, Copple and Peng[1] found that by applying uniaxial strain, WZ GaAs nanowires experience an interesting direct-indirect band gap transition. Strain is demonstrated as an alternative approach for band engineering to fit a particular application purpose.

To demonstrate a full potential of strain engineering, in this work, we have extended our study to both WZ and ZB nanowires and explore a variety of strain scenarios. We found that whether a strain can trigger the direct-indirect band gap transition in GaAs nanowires depends strongly on the type of applied strain. In addition, the origination of the direct-indirect band gap transition was discussed through a detailed examination of the near-gap band states. Depending on the symmetry and bonding/antibonding nature of specific electronic orbitals, the associated energy can respond very differently to an applied strain, essentially resulting in the observed direct-indirect band gap transition.

74

The first principles density functional theory (DFT)[13] calculations were carried out using Vienna *Ab-initio* Simulation Package (VASP).[50, 51] The DFT local density approximation and the projector-augmented wave potentials[102, 103] were used along with plane wave basis sets. The kinetic energy cutoff for the plane wave basis set was chosen to be 300.0 eV. The energy convergence criteria for electronic and ionic iterations were set to be 10^{-4} eV and 0.03 eV/Å, respectively. The Ga 3d, 4s, 4p, As 4s, 4p and H 1s electrons were treated as valence electrons. The reciprocal space of a nanowire was sampled at $1 \times 1 \times 6$ using Monkhorst-Pack meshes. In band structure calculations, a total of 21 K-points were included along the K vector path from Γ (0, 0, 0) to X (0, 0, 0.5).

Figure IV.5 Images of the studied WZ and ZB GaAs nanowires. The diameter and composition of each wire in a unit cell are given on top. Dashed rectangles in the side views indicate the unit cell. The red, blue, and white dots represent Ga, As, and H atoms, respectively.

The 1D WZ GaAs nanowire was generated along the [0001] direction (i.e. the z-axis) from the bulk WZ GaAs. The diameter of the WZ nanowire is 22.2 Å, constituted by 54 Ga and 54 As atoms (see Figure IV.5) in the unit cell. The ZB GaAs nanowire were obtained along the [111] direction from the bulk ZB phase GaAs. The diameter of the ZB nanowire is 17.0 Å, formed by 37 Ga and 37 As atoms in the unit cell. The dangling bonds on the surface of the nanowires were saturated by hydrogen atoms to maintain the tetrahedral network of Ga/As atoms.

75

The initial axial lattice constant in the WZ and ZB nanowires were set to be 6.51 Å and 9.72 Å, respectively, which were taken from the relaxed lattice constant of the bulk WZ and ZB GaAs, respectively. In addition to the axial lattice constant, the lateral length of the simulation cell was chosen so that the distance between the wire and its replica (due to periodic boundary conditions) is more than 14 Å to minimize the interactions between the nanowire and its replica. The axial lattice constant in the GaAs wires was optimized through the technique of total energy minimization. The optimized lattice constants in the WZ and ZB nanowires are 6.51 Å and 9.67 Å, respectively.

Once the optimized geometry of a nanowire was obtained, a series of different types of strain were applied to the nanowire. The studied strain includes uniaxial strain, radial strain, strain along a specific crystalline direction, and shear stain, as shown in Figure IV.6.
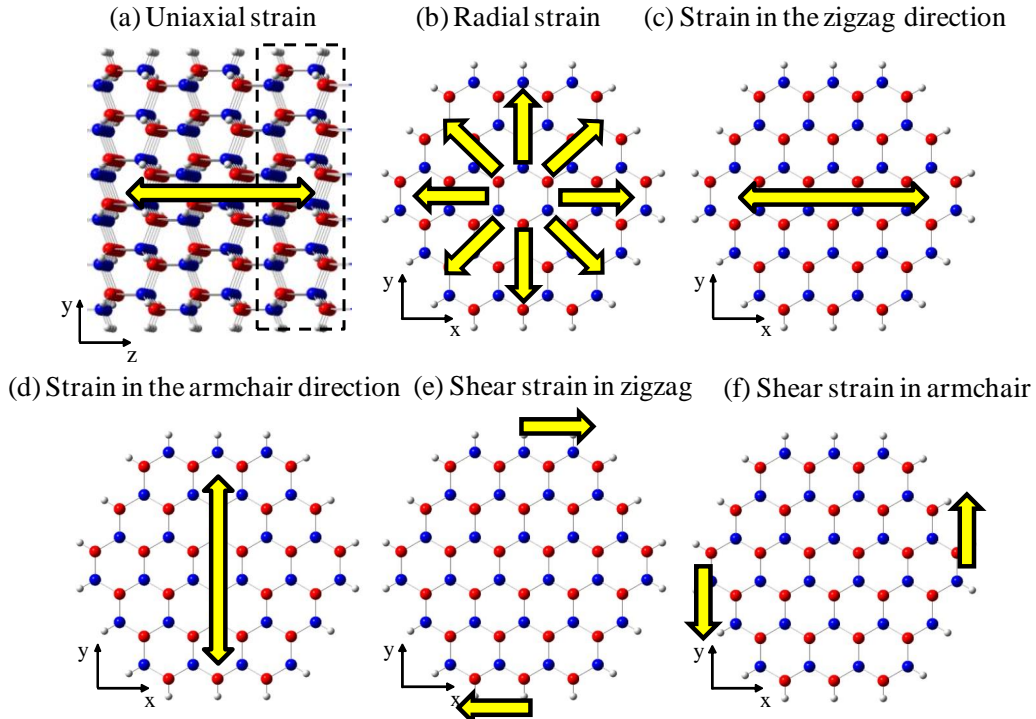
Figure IV.6 Schematics of the studied strains (a) uniaxial strain along the axial direction (i.e. the z-axis), (b) radial strain in the cross section, (c) strain along the zigzag direction (i.e. the x-axis), (d) strain along the armchair direction (i.e. the y-axis), and shear strain in (e) the zigzag and (f) the armchair directions.

The uniaxial strain was applied by rescaling the axial lattice constant of the wire in the z-direction. For example, a +2% tensile strain was applied by rescaling the axial lattice constant to 102% of its optimized value; while a -2% compressive strain was to scale the lattice constant to 98% of its optimized value. Under each given uniaxial strain, the coordinates of the atoms in the nanowires were fully relaxed via the technique of total energy minimization.

In the case of radial strain, strain was isotropically applied to the cross section (i.e. xy-plane) of the wires. For each applied radial strain, the axial lattice constant and z-coordinates of the wire were fully relaxed to reach the total energy minimum.

We also applied strain along a particular crystalline direction in the cross section of the nanowires. Two particular directions were chosen, namely the zigzag (i.e. x-axis) and the armchair (i.e. y-axis), shown in Figure IV.6. In these two cases, strain was only

applied to the x (or y) coordinates of the atoms, while all other coordinates including the axial lattice constant were fully relaxed.

The definition of shear strain at nanoscale is not unique. In this work, simple shear strain is mathematically defined as

$$\tan\theta = \frac{d}{l} \qquad (IV.1)$$

where l is the original length of a given line, d is the amount of deformation perpendicular to that given line, and θ is the angle the sheared line makes with its original orientation. For example, in our study of shear strain in the zigzag-direction (see Figure IV.6 (e)), l is taken as the y coordinate of the atoms and d is the displacement of the atoms along the x-direction. Similarly, we also applied shear strain to the y-direction. For each strain, the coordinates which held the strain were kept fixed while all other coordinates including the lattice constant were optimized through total energy minimization.

Note that the strain extremes considered in this work are beyond the elastic limit in bulk GaAs. However the nucleation of defects such as dislocations may become energetically unfavorable, especially in the small size nanowires. As shown in a recent experimental work done by Wang et al.[148], the GaAs nanowires can hold a significantly higher strain than 1%. To obtain a practical feeling for applying strain, we estimated the stress which might be required. For example, to apply +2% tensile uniaxial strain to the WZ GaAs nanowire, a calculated stress of 2.5 GPa may be required.

The band gap of a semiconductor is defined as the energy difference between the conduction band minimum (CBM) and the valence band maximum (VBM). If CBM and VBM are vertically aligned at the same K-point in its band structure, the band gap is

direct, otherwise it is called indirect. It is known that bulk WZ and ZB GaAs have a direct band gap[124, 137] with both VBM and CBM located at Γ.
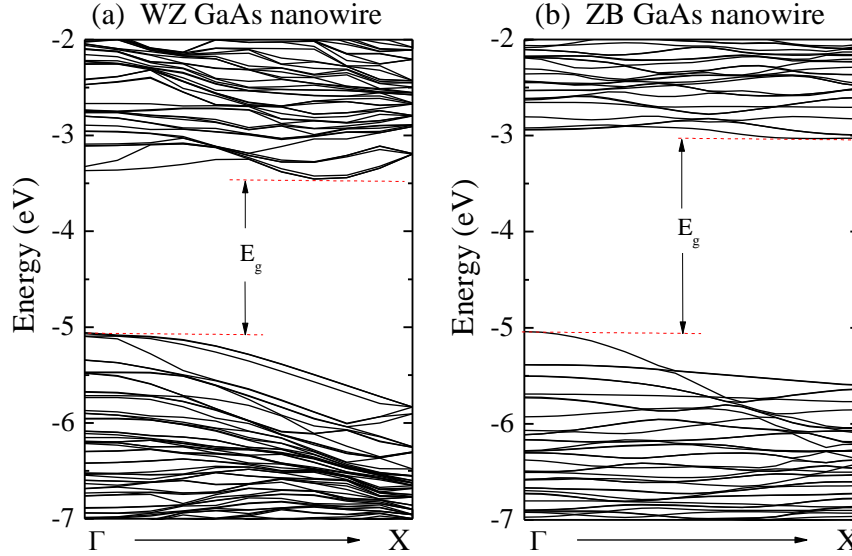
Figure IV.7 Band structures of the geometry-optimized WZ and ZB GaAs nanowires. Both demonstrate an indirect band gap. Energies are referenced at the vacuum level.

However, our calculated band structures of the 1D WZ and ZB GaAs nanowires demonstrate an indirect band gap, as shown in Figure IV.7. VBM of both nanowires are located at Γ, however CBM is not at Γ. For the WZ nanowire, CBM is located at the conduction band valley near X, while for the ZB nanowire, CBM is located at X. Previous work reported a similar indirect band gap for small sized GaAs nanowires. Copple and Peng[92] reported that, for the WZ GaAs nanowires, the critical nanowire size for the direct-indirect band gap transition is ~ 28 Å, estimated from DFT calculations. WZ nanowires with a diameter smaller than this critical size demonstrate an indirect band gap while wires larger than the critical size show a direct band gap.[91] In the case of ZB GaAs nanowires, the critical size for the band gap transition was ~ 40 Å, reported by Persson and Xu using tight-binding calculations.[135] The diameters of our studied WZ and ZB GaAs nanowires in this work are 22.2 Å and 17.0 Å, respectively, which are both

79

smaller than their threshold size. The indirect band gap predicted in our work is consistent with literature.

The calculated band gap for the WZ and ZB GaAs nanowires are 1.603 eV and 2.008 eV, respectively. It is well known that DFT underestimates band gap of semiconductors, and advanced GW methods[149-151] can provide improved predictions in the band gap. However, for the size of the nanowires investigated in the present work, GW is not applicable due to its extremely high demand on computing resources. The present work is mainly focused on the variation of electronic properties such as energy levels with strain. Previous studies[95] on Si nanoclusters showed that the energy gap calculated by DFT obeys a similar strain-dependency as the optical gap predicted by advanced configuration interaction (CI) method and the quasi-particle gap (defined as the difference of ionization potential and electron affinity). In addition, DFT gap predicts a similar size-dependency as the optical gap obtained using GW and quantum Monte Carlo methods.[152, 153] Therefore, we expect that our reported general trends with strain variation for the electronic band structure and near-gap band states in the GaAs nanowires are correct. In the following we will present the effects of various strains on the band structure and the near-gap band states in the WZ and ZB GaAs nanowires.

(a) Uniaxial strain. The effect of the uniaxial strain on the band structure of the WZ and ZB GaAs nanowire is plotted in Figure IV.8. As mentioned before, without strain the WZ nanowire demonstrates an indirect band gap with CBM located at the conduction band valley near X (labeled as $E_{\text{CB-v}}$ in Figure IV.8 (c)). With uniaxial compression of -2% or -4%, CBM is shifted to Γ, demonstrating a direct band gap as shown in Figure IV.8 (a) and (b). When the nanowire is under +4% uniaxial tensile strain, it also shows a

direct band gap at Γ. In the case of the ZB nanowire, CBM is located at X for the relaxed

wire. Tensile uniaxial strain as large as +4.5% can convert the gap to be direct.

From Figure IV.8, it was also observed that the value of the band gap can be tuned by

the strain. For example, the gap shrinks under both positive and negative strains in the

WZ nanowire. The DFT predicted gap for the relaxed WZ nanowire is 1.603 eV. And the

gap shrinks to 1.133 eV and 1.308 eV for -4% and +4% strain, respectively.
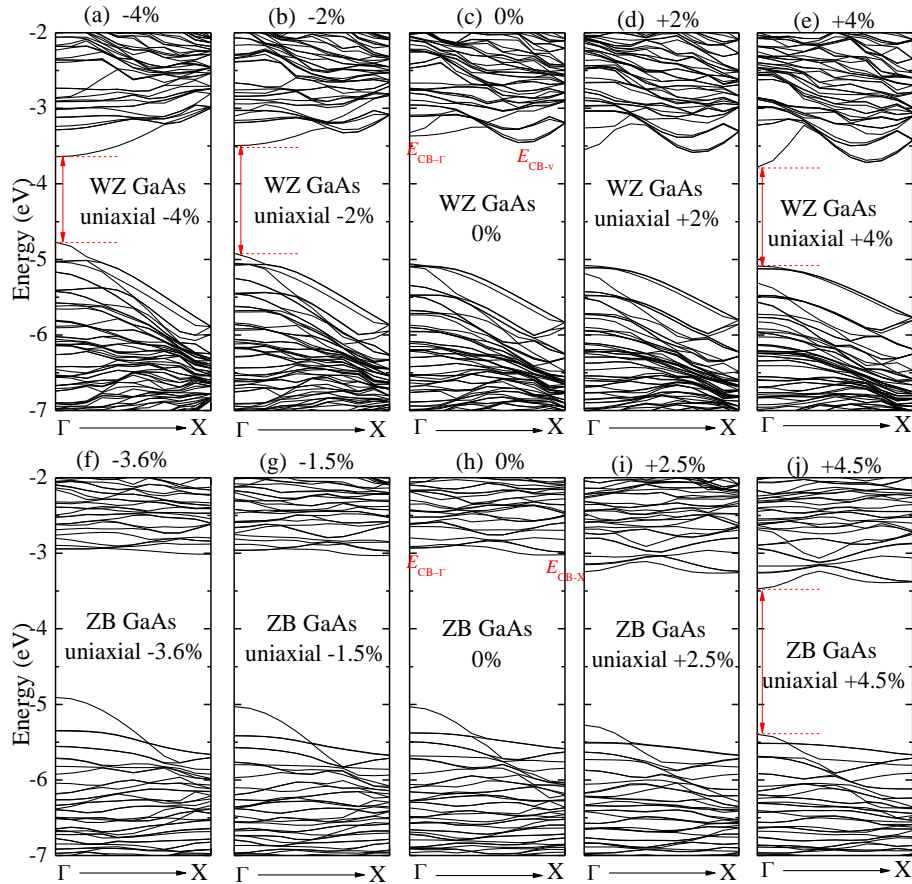
Figure IV.8 The effect of the uniaxial strain on the band structure of (a)-(e) the WZ GaAs nanowire and (f)-(j) the ZB nanowire. Positive and negative values of strain refer to the tensile and compressive uniaxial strains, respectively. Energies are referenced at the vacuum level. A direct band gap was found at +4%, -2%, and -4% in the WZ nanowire, and at +4.5% for the ZB nanowire. For the relaxed WZ and ZB wires, labels $E_{CB-\Gamma}$, E_{CB-V}, and E_{CB-X} represent the energies of the conduction bands at Γ, at the conduction band valley, and at X, respectively.

As can be seen from Figure IV.8, the direct/indirect band gap in the WZ nanowire is

the result of the energy competition of the two conduction band (CB) states $E_{CB-\Gamma}$ and

E_{CB-v}. The nanowire yields a direct band gap if $E_{CB-\Gamma}$ is lower than E_{CB-v}, otherwise it has

an indirect band gap. For the ZB nanowire, the direct/indirect band gap is determined by the energy competition of $E_{CB-\Gamma}$ and E_{CB-X}.

In order to determine the critical strain in which the direct-indirect band gap transition occurs, we plotted the energies of the two competing CB states $E_{CB-\Gamma}$ and E_{CB-v} as a function of strain. As an example, Figure IV.9 (a) shows the plots for the WZ nanowire. The energy of the VBM at Γ E_{VBM} is also plotted in Figure IV.9 (a) for comparison. Examination of the curves of two conduction bands $E_{CB-\Gamma}$ and E_{CB-v} in Figure IV.9 (a) reveals two crossovers. One is estimated to be ~ +2.8% and the other -0.8%, indicated by the dashed vertical lines, which are the critical strain for the direct-indirect band gap transition in the WZ nanowire. The WZ GaAs nanowire transitions to a direct band gap with a positive strain higher than +2.8% or a negative strain lower than -0.8%.
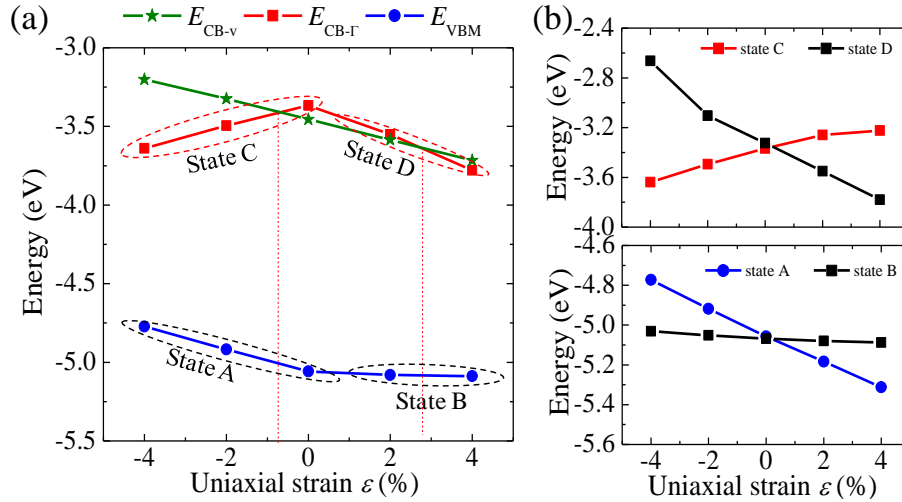
Figure IV.9 (a) The calculated energies for the VBM (E_{VBM}), the conduction bands at Γ ($E_{CB-\Gamma}$), and the valley (E_{CB-V}) as a function of the uniaxial strain in the WZ GaAs nanowire. The direct-indirect band gap transition occurs at about +2.8% and -0.8%, indicated by the dashed vertical lines. The VBM is the result of competition between the two states A and B, and the conduction band at Γ is the result of competition between states C and D. (b) The energy variation with strain for states A-D is plotted. All energies are referenced at the vacuum level.

It was also found that, in Figure IV.9 (a), the energy variation with strain displays a different trend for a different band state. E_{CB-v} shows a *linear* behavior – the energy decreases with a positive strain while increasing with a negative strain. However, the

82

other two states $E_{\text{CB-}\Gamma}$ and E_{VBM} demonstrate a *non-linear* relationship with strain. The energy of the VBM increases with a negative strain while it remains flat with a positive strain. $E_{\text{CB-}\Gamma}$ drops at both negative and positive strains.

In order to understand the *non-linear* behavior, the electronic states $E_{\text{VBM}}, E_{\text{CB-}\Gamma}$ and $E_{\text{CB-v}}$ at each strain were examined. It was found that the CB at the valley ($E_{\text{CB-v}}$) corresponds to the same electronic state at different strain, which yields the *linear* curve of $E_{\text{CB-v}}$. However, the VBM (or the CB at Γ) does not correspond to the same electronic state at different strain. For example, two states – A and B – compete for the VBM. To better understand this, the energies of states A and B as a function of strain is plotted in Figure IV.9 (b). These two curves experience a crossover. With a negative strain, the energy of state A is higher than that of B, thus state A represents the VBM. When applying a positive strain, the energy of state B is higher than that of A, therefore state B represents the VBM. The curve of E_{VBM} in Figure IV.9 (a) is the result of the energy competition between states A and B.

Similarly, the curve of $E_{\text{CB-}\Gamma}$ in Figure IV.9 (a) is the result of the energy competition between states C and D. The energies of states C and D as a function of strain were also plotted in Figure IV.9 (b), and they also demonstrate a crossover. Under a negative strain, state C has a lower energy compared to state D, thus state C represents the CB at Γ. However, with a tensile strain, state C has a higher energy than state D, therefore state D is the CB at Γ.

It was clear that the energies of the states A-D and $E_{\text{CB-v}}$ are nearly *linearly* shifted with the uniaxial strain in Figure IV.9. For states A, D and $E_{\text{CB-v}}$, their energies decrease with a positive tensile strain while increasing with a negative compression. In contrast,

83

state C shows an opposite trend – energy increases with a positive strain and decreases with a negative compression. State B is relatively independent on the uniaxial strain and its energy remains flat with strain. This *linear* shift of energy levels with strain is not unique to the studied GaAs nanowires. It is also observed in other semiconducting nanostructures.[10, 11, 84, 94, 95, 138]

In order to understand the linear trends for states A-D and E_{CB-v} in Figure IV.9, their electronic states, such as electron charge distribution and wavefunction, were examined. The wavefunction character was examined by projecting the wavefunction onto s-, p-, and d-orbitals at each ionic site. It was found that state A is dominated by p_z-orbitals at the sites of Ga and As; state B is dominated by partial p_x- and partial p_y-orbitals, and states C, D and E_{CB-v} are all dominated by s-orbitals. Figure IV.10 presents their electron density contour plots and schematics of the wavefunction character.
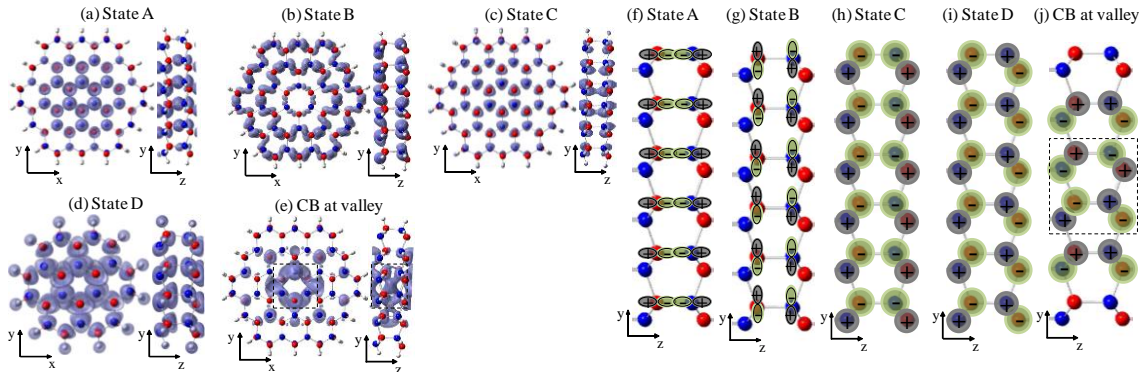
Figure IV.10 (a)-(e) The electron-density contour plots and (f)-(j) schematics of the wavefunction character (i.e. the projected major orbitals and signs of the phase factor) of near-gap states in the WZ GaAs. State A is dominated by bonding p_z orbitals at the sites of Ga and As. State B is dominated by partial p_x and partial p_y orbitals. States C, D, and the CB at the valley are all dominated by s orbitals. The red, blue, and white dots represent Ga, As, and H atoms, respectively. To emphasize the wavefunction character on the sites of Ga and As, H atoms were not shown in (f)-(j). The atoms inside the rectangle in (j) are those inside the rectangles in (e).

Although states C and D are dominated by s-orbitals, the phase factor of their wavefunctions shows a distinct difference. In state C, the four atomic layers of atoms (As, Ga, As, Ga) which are perpendicular to the z-axis demonstrate a phase order of +, -,

-, +, as shown in Figure IV.10 (h). However, in state D, that phase order is +, -, +, -.

Therefore, the Ga-As bonds along the z-direction (formed by the middle two atomic

layers) shows a *bonding* character in state C, while displaying an *antibonding* character in

state D (also see their electron density contour plots).

As speculated in literature,[95, 138-140] such different energy trends with respect to strain

may be due to the different strain response from involved energy components. Here

through the exchange energy model (Heitler–London),[114] we further demonstrated that

this different energy response to strain can be originated from the bonding and

antibonding nature of orbitals. Although this model was originally developed for the

hydrogen molecule, it may still give us useful physical insight as long as the exchange

integral is mainly considered from the nearest neighbored atoms.

In this model of hydrogen molecule, the energies of its bonding and antibonding

states are given by the equations I.14 and I.15 from the introduction to the dissertation.

Therefore, the exchange integral term H may be playing a dominant role in determining

the different energy variation behaviors with strain in the bonding and antibonding

situation. From equation I.16, the exchange term H is contributed from either *non-*

classical electron-electron (i.e. $\frac{1}{r_{12}}$, positive) or electron-ion interaction (i.e. $-\frac{1}{r_{2a}} - \frac{1}{r_{1b}}$,

negative). For s-orbitals, the contribution of the electron-ion interaction is dominated

over the electron-electron interaction in the exchange term H. As the atomic distance

increases (corresponds to a positive strain), the energy contributed from the electron-ion

interaction is increased more rapidly compared to the energy reduction of the electron-

electron contribution (see equation I.16), which results in an increased value for H. And

an increased H value causes the bonding energy $E_{bonding}$ to increase and the antibonding

energy $E_{antibonding}$ to decrease based on equations I.14 and I.15. This could be the reason for the different trends for states C (bonding s-orbital) and D (antibonding s-orbital) in Figure IV.9 (b).

However, the situation becomes different when the orbital is not an s-orbital. For example, bonding *p-orbitals* demonstrate a different energy trend with strain, compared to bonding *s-orbitals*. As mentioned before, state A is dominated by p_z-orbitals. The phase order of the p_z-orbitals in the middle two atomic layers which are perpendicular to the z-direction are + and -, respectively, as shown in Figure IV.10 (f). This phase order yields a strong bonding character of the p_z-orbitals in the z-direction (also see their electron density contour plots). A positive tensile strain causes the energy of the bonding p_z-orbital of state A to decrease, opposite to that of the bonding s-orbital of state C. This might be due to the spindle shape of the p-orbitals in which the electron density is quite high in the region between atoms. In this case, the contribution of the non-classical electron-electron interaction in the exchange integral in equation I.16 is dominating compared to the electron-ion interaction. As the atomic distance increases (corresponds to a positive strain), the energy contribution of the electron-electron interaction is decreased more significantly compared to the increase of the electron-ion contribution, which gives a reduced value for *H*. And the decreased *H* value results in an energy reduction of the bonding state from equation I.14. This explains the energy trends for state A in Figure IV. 9 (b).

In the case of state B, the wavefunction is dominated by partial p_x- and p_y-orbitals. The phase order of the p_y-orbitals in the middle two atomic layers are + and -, respectively, as shown in Figure IV.10 (g), which yields an antibonding character in the

z-direction (also see the electron density contour plots). However, the spindle shape of p_x- and p_y-orbitals creates a concentration of electrons in the xy-plane. The wavefunction overlapping in the z-direction is expected to be small and gives a non-bonding nature in the z-direction. Applying the uniaxial strain in the z-direction does not affect the electronic orbital of state B much, and its energy is insensitive to the uniaxial strain, which explains the flat curve of state B in Figure IV.9 (b).

For the conduction band at the valley (E_{CB-v}), it is clear that some Ga-As bonds along the z-direction show a bonding character while others display an antibonding character from its phase factor in Figure IV.10 (j). However, the electron contour plot in Figure IV.10 (e) reveals that the electron cloud is mostly concentrated on the center atoms. Therefore its bonding/antibonding character should be determined by the center atoms. From the phase factor of the center atoms inside the dashed rectangle in Figure IV.10 (j), it shows an antibonding character. Thus, the energy variation trends with strain for this state should follow the same trends as state D which is also dominated by antibonding s-orbitals. This conclusion is consistent with our data for E_{CB-v} in Figure IV.9 (a).

Similar analysis was also applied to the ZB nanowire, and the critical uniaxial strain of the band gap transition was found to be +3%.The energy variation trends with strain for the near-gap states in the ZB nanowire follow the above general conclusions for the WZ nanowire.

(b) Radial strain. Radial strain was applied to the cross section of the WZ and ZB GaAs nanowires. At each given radial strain, the z-coordinates of the atoms and the axial lattice constant of the nanowires are fully relaxed to reach the total energy minimum. The effect of the radial strain on the band structure of the WZ and ZB GaAs nanowire is

presented in Figure IV.11. When looking at the WZ nanowire, the direct band gap only occurs for the positive radial strain at +2% and +4%. Within the strain range studied in this work, no band gap transition occurs for the negative strain. In contrast, for the ZB wire, only a negative strain at -4% can have a direct band gap.
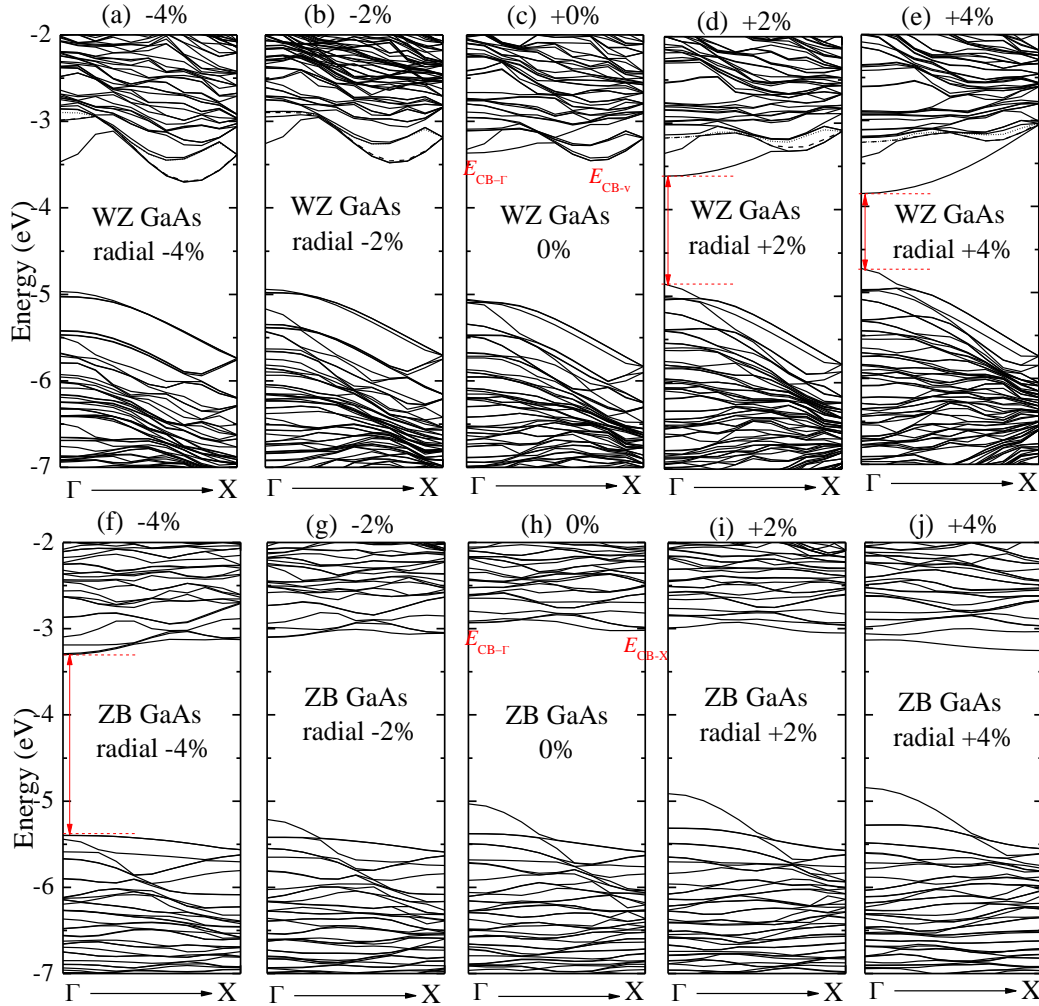
Figure IV.11 The effect of the radial strain on the band structure of (a)-(e) the WZ GaAs nanowire and (f)-(j) the ZB nanowire. A direct band gap was found at +2% and +4% in the WZ nanowire and at -4% for the ZB nanowire.

To estimate the critical radial strain needed to trigger the band gap transition, the energies of three near-gap states, $E_{CB\text{-}\Gamma}$, $E_{CB\text{-}v}$ and E_{VBM}, are plotted as a function of the radial strain. As an example, Figure IV.12 (a) shows the curves for the WZ GaAs

nanowire. From the crossover of the two conduction bands, the critical strain for the direct-indirect gap transition was estimated to be ~+0.4%.
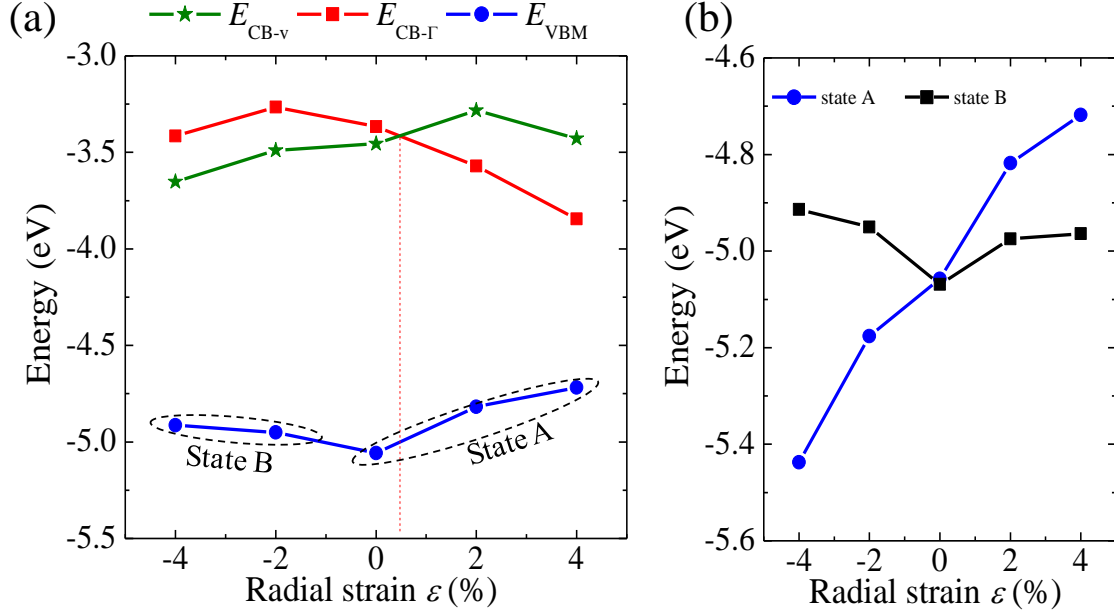
Figure IV.12 (a) The calculated E_{VBM}, $E_{CB-\Gamma}$, and E_{CB-V} as a function of the radial strain in the WZ GaAs nanowire. The direct-indirect band gap transition occurs at about +0.4% radial expansion. (b) The energies of two competing states A and B for the VBM as a function of strain.

Further examination of three near-gap states at different values of radial strain, it was found that the VBM is the result of energy competition of two states A and B, while each conduction band ($E_{\text{CB-}\Gamma}$ or $E_{\text{CB-}v}$) corresponds to the same electronic state at different values of radial strain. State A/B is the same state discussed in the previous section. And $E_{\text{CB-}\Gamma}$ is the previous state C. The energy variation of states A and B as a function of radial strain is presented in Figure IV.12 (b). The energy of state A is more sensitive to the radial strain, compared to that of B. The energy shifts for states A and B in the range of ±4% radial strain are 0.719 eV and 0.155 eV, respectively.

Similar to the case of the uniaxial strain, the energy of state B is insensitive to the radial strain due to its unique electronic structure which is dominated by partial p_x- and p_y-orbitals. It is more interesting to note that the energy variation of state A in Figure

IV.12 (b) is opposite that of the uniaxial strain in Figure IV.9 (b). This could result from the Poisson's effect. When a positive radial strain (i.e. expansion) is applied to the nanowire, the axial lattice constant of the nanowire shrinks, which is correlated to the case of a negative uniaxial compression. For example, when +2% (+4%) radial expansion is applied to the WZ nanowire, the resulting axial lattice constant shrinks to 99.1% (98.2%) of its original value. This corresponds to the case of -0.9% (-1.8%) uniaxial strain. When -2% (-4%) radial compression is applied, the resulting axial lattice constant expands to 101.2% (102.3%) of its original value, which is correlated to the situation of +1.2% (+2.3%) uniaxial strain. This fact yields the opposite energy trends for state A with the radial and uniaxial strains. This situation was also applied to the two conduction bands ($E_{\text{CB-}\Gamma}$ or $E_{\text{CB-}v}$), in which their general energy variation trends in Figure IV.12 (a) are opposite to their counterparts in Figure IV.9, respectively (note $E_{\text{CB-}\Gamma}$ in Figure IV.12 (a) corresponds to state C). Similar analysis was applied to the ZB nanowire and the critical radial strain for the direct-indirect band gap transition was found to be -1.4%.

(c) Strain along a specific crystal direction in the cross system. We applied a strain along a particular crystal direction in the cross section of the GaAs nanowires. Two specific crystal directions are chosen in this study, namely the zigzag and armchair directions, which correspond to the x- and y-axis, respectively. It was found that applying strain in different directions results in different effects on the electronic band structure. For example, applying strain in the armchair direction is easier to trigger the direct-indirect band gap transition than that of the zigzag direction, in terms of the strain energy.

The effect of the strain in the zigzag direction on the band structure of the WZ and ZB GaAs nanowire is plotted in Figure IV.13. Similar to the radial strain, a compressive

strain in the zigzag direction doesn't trigger the gap transition in the WZ wire. A

sufficiently big expansion, such as +4%, can convert the indirect gap to direct. For the ZB

wire, only a negative strain (-4%) can trigger the gap transition in the range of strain that

we examined.
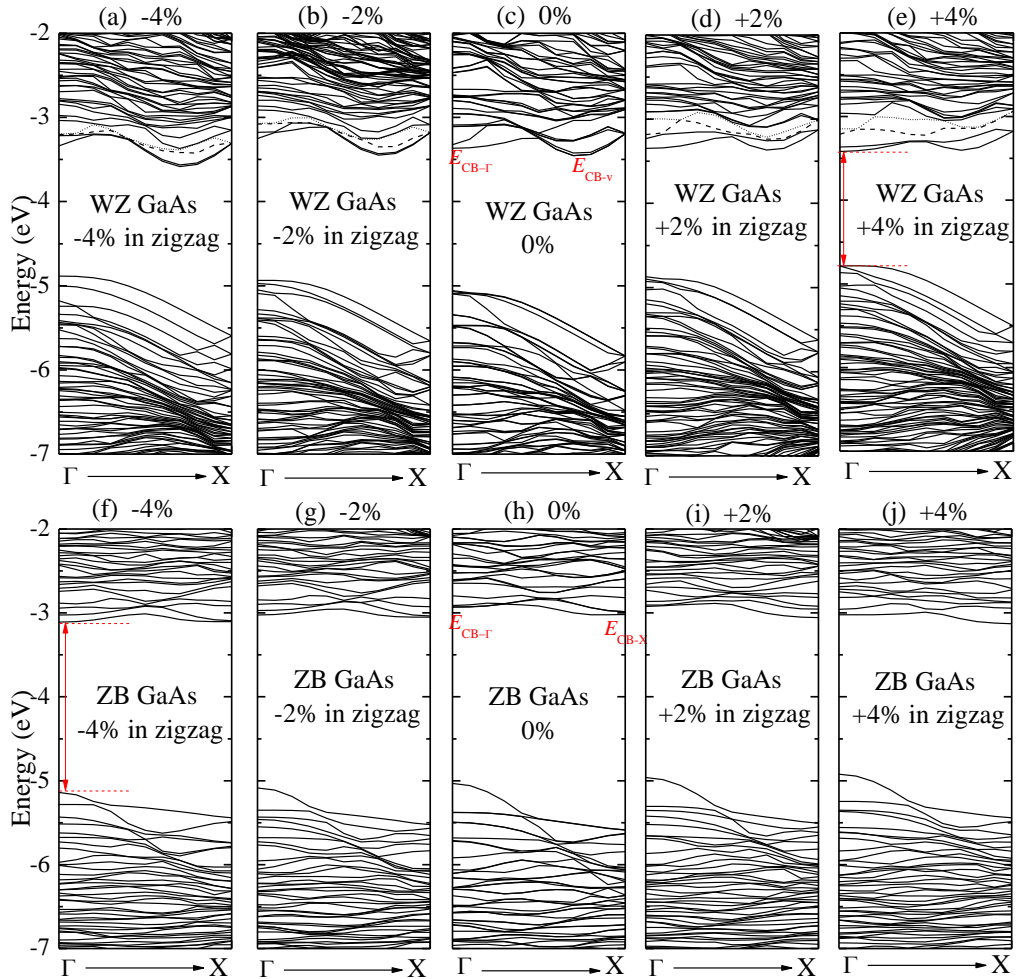
Figure IV.13 The effect of the strain along the zigzag direction on the band structure of (a)-(e) the WZ GaAs nanowire and (f)-(j) the ZB GaAs nanowire. A direct band gap was found at +4% strain in the WZ wire and at -4% in the ZB wire.

The critical strain in the zigzag direction needed to trigger the direct-indirect gap

transition is estimated through the energy crossover of the two competing conduction

bands. As an example, Figure IV.14 (a) displays their energy variation with strain for the

WZ nanowire. The energy crossover of the two conduction bands occurs at +3%. Unlike

91

the cases of the previous uniaxial and radial strains, the zigzag strain shows a less profound effect on tuning the energies of conduction bands. For example, in the range of strain studied in this work, the energy shifts for the conduction band at Γ are 0.412 eV, 0.579 eV and 0.216 eV for the uniaxial, radial and zigzag strains, respectively. And the energy shifts of the conduction band at the valley are 0.515 eV, 0.368 eV and 0.224 eV, for the uniaxial, radial and zigzag strains, respectively.

Figure IV.14 (a) The calculated E_{VBM}, $E_{CB-\Gamma}$, and E_{CB-V} as a function of strain along the zigzag direction in the WZ GaAs nanowire. The direct-indirect band gap transition occurs at about +3% expansion in the zigzag direction. (b) The electron-density contour plot for state E. (d) The sign of the wavefunction phase factor in state E, which is dominated by p_x orbitals. The atoms inside the rectangle in (d) are those inside the rectangle in (c).

The VBM in Figure IV.14 (a) is the result of competition of two states A and E. State A is still the same state shown in Figure IV.10. The strain effect on the energies of A and E is plotted in Figure IV.14 (b). It shows state E experiences an energy increase with a negative zigzag strain. The electron density contour plot of state E is presented in Figure IV.14 (c). Examination of the wavefunction of state E reveals it is dominated by p_x-orbitals. The sign of the wavefunction phase factor shown in Figure IV.14 (d) suggests that state E has a bonding p_x character in the x-direction. According to the above discussion on the bonding p_z-orbital of state A, a negative compressive strain in the z-direction gives an increased energy for state A. Similarly here, a negative stain in the x-

92

direction results in an energy increase for state E, which is consistent with our data in Figure IV.14 (b).

The energy trend of state A with the zigzag strain is very similar to the case of the radial strain, which is not surprising because these two types of strains both are applied in the cross section of the nanowire. A positive strain applied radially or in the zigzag direction results in a shrink of the axial lattice constant of the nanowire, due to the Poisson's effect. For example, applying -4%, -2%, +2%, or +4% strain in the zigzag direction yields the axial lattice constant of the WZ wire to be 100.72%, 100.42%, 99.89%, or 99.45% of its original value, respectively. In addition, the energy trends for the two conduction bands with the zigzag strain are also similar to their counterparts with the radial strain.

For the strain applied in the armchair direction, it was found that it requires a lower value of critical strain to trigger the direct-indirect band gap transition in these GaAs nanowires. From the energy crossover of the two competing conduction bands, the critical strain for the direct-indirect gap transition is estimated to be +1% and -2.2% for the WZ and ZB nanowires, respectively (see Figure IV.15 (a)). Similar to the case of the zigzag strain, the energy shifts with strain for the three near-gap states in Figure IV.15 (a) are relatively small, compared to the previous uniaxial and radial strains. For example, the energy shifts of the conduction band at the valley are 0.515 eV, 0.368 eV, and 0.180 eV, for the uniaxial, radial and armchair strains, respectively.
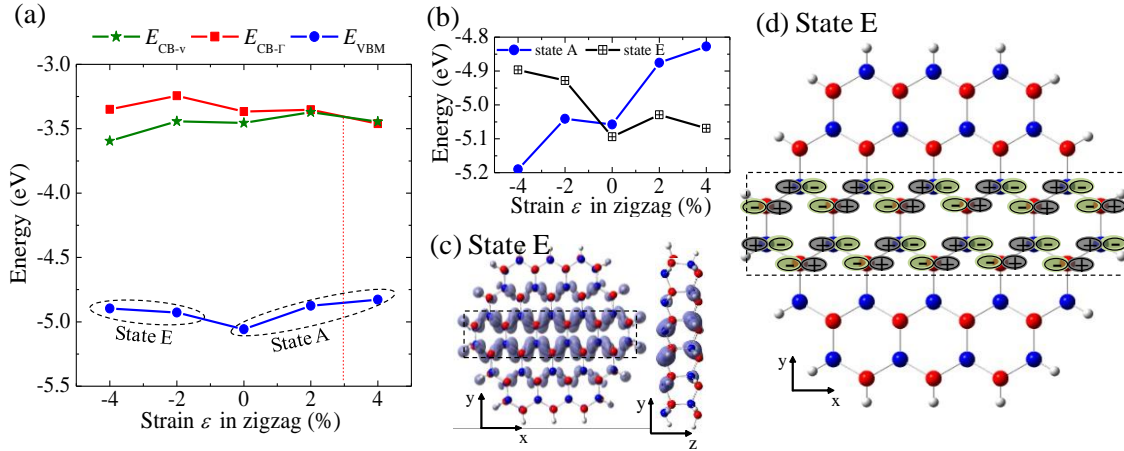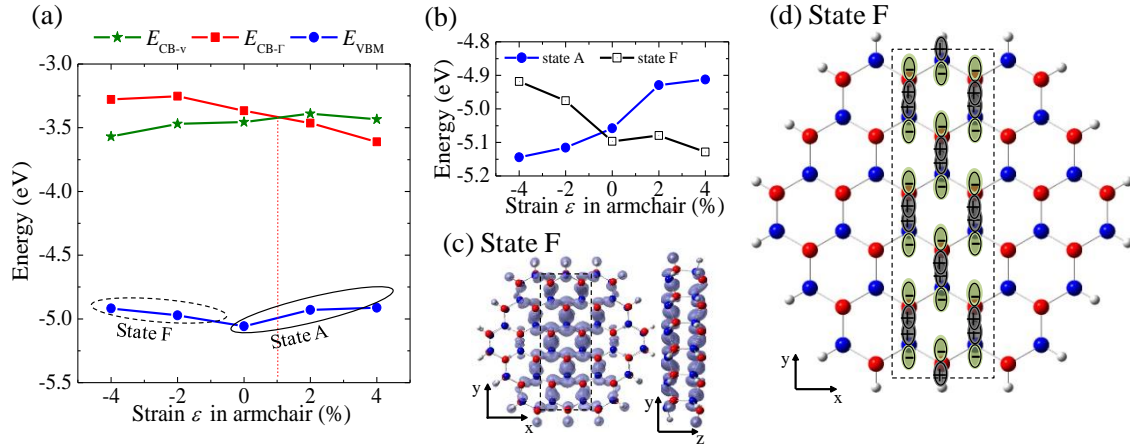
Figure IV.15 (a) The calculated E_{VBM}, $E_{CB-\Gamma}$, and E_{CB-V} as a function of strain along the armchair direction in the WZ GaAs nanowire. The direct-indirect band gap transition occurs at about +1% expansion. (b) The energies of two competing states A and F for the VBM as a function of strain. (c) The electron-density contour plot for state F. (d) The sign of the wavefunction phase factor for state F, which is dominated by p_y orbitals.

In Figure IV.15 (a), the VBM was found to be contributed by two competing states, namely states A and F. Their energies as a function of the armchair strain are plotted in Figure IV.15 (b). The electron charge distribution and wavefunction character of state F is presented in Figure IV.15 (c) and IV.15 (d). The projection of the wavefunction reveals that state F is dominated by p_y-orbitals. The sign of the phase factor suggests that state F shows strong bonding in the y-direction. This unique wavefunction character yields its energy trends with strain in Figure IV.15 (b) (see the above explanation for states E and A). State A is still the same state presented in Figure IV.10, therefore the energy variation trend of state A in Figure IV.15 (b) is similar to that of the zigzag strain in Figure IV.14 (b).

(d) Shear strain along the zigzag or armchair direction. Shear strains along the zigzag and armchair directions were applied to the WZ GaAs nanowire. It was found that no direct-indirect band gap transition occurs with the strain range studied (up to +4%) in this work. The effect of shear strain in the zigzag direction on the band structure of the WZ GaAs nanowire is presented in Figure IV.16 (a)-(c). No negative shear strain is

studied because a negative shear strain causes the same effect as the positive shear strain

due to the symmetry of the nanowire and the definition of shear strain in equation IV.1.
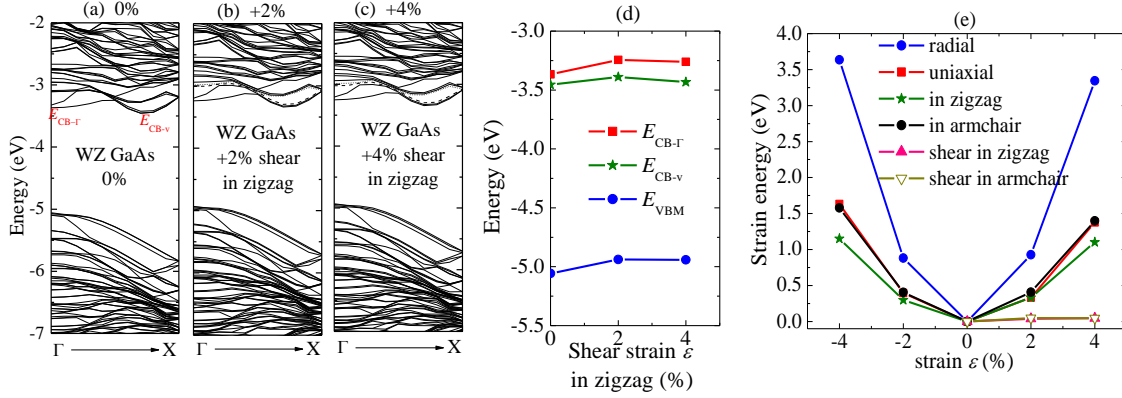
Figure IV.16 (a)-(c) The effect of shear strain along the zigzag direction on the band structure of the WZ GaAs nanowire. No direct-indirect band gap transition occurs within the strain range studied in this work. (d) The calculated E_{VBM}, $E_{CB-\Gamma}$, and E_{CB-V} as a function of shear strain along the zigzag direction. (e) The strain energies to the WZ GaAs nanowire as a function of the strain value for all types of strains.

It is clear that the shear strain plays a negligible effect on tuning the electronic band

structure of the WZ GaAs nanowire. This conclusion is further demonstrated in Figure

IV.16 (d), in which the energies are plotted as a function of shear strain. Within the strain

range, the energy shifts are 0.120 eV, 0.123 eV and 0.112 eV for E_{VBM}, $E_{CB-\Gamma}$ and E_{CB-v},

respectively. These energy shifts are much smaller compared to those of all other strain

types discussed above. There is no energy crossover for the two curves of $E_{CB-\Gamma}$ and E_{CB-v} in Figure IV.16 (d), suggesting no direct-indirect band gap transition. Each state of

E_{VBM}, $E_{CB-\Gamma}$ and E_{CB-v} corresponds to the same electronic orbitals at different values of

shear strain.

Similar behavior is also found in the case of the shear strain along the armchair

direction. It was found that the shear strain in the armchair direction demonstrates an

even smaller effect on turning the band structure. The energy shifts with strain for E_{VBM},

$E_{CB-\Gamma}$ and E_{CB-v} are 0.110 eV, 0.109 eV and 0.097 eV, respectively.

95

The negligible effect of the shear strains on the band structure might be resulting from the much smaller strain energy introduced by the shear strains to the GaAs nanowire. The strain energy is defined as the difference in the total energy between the strained and the relaxed nanowire. As an example, the strain energy as a function of the value of strain is presented in Figure IV.16 (e) for the WZ GaAs nanowire. Clearly, the shear strain energy is negligible compared to other strain types. The shear strain energy is less than 0.045 eV under +4% shear strain either along the zigzag or the armchair direction. The strain energy introduced by the radial strain is the largest given the same value of strain ε among all strain types studied in this work. This is because in the radial strain, two dimensions (both x and y) are strained. The strain energies of the rest of the three strains, namely the uniaxial strain and strain in the zigzag and armchair directions, are close given the same value of strain ε. This is due to the fact that in these three types of strains, only one dimension is under strain.

Table IV.I The critical strain value and strain energy to trigger the direct-indirect band gap transition in the WZ and ZB GaAs nanowires. No band gap transition was found for the shear strains.

GaAs phase	Strain type	critical strain ε (%)	critical strain energy (eV)
WZ	Uniaxial	+2.8, -0.8	0.65, 0.08
	Radial	+0.4	0.05
	In zig-zag	+3	0.64
	In armchair	+1	0.10
	Shear in zig-zag	N/A	N/A
	Shear in armchair	N/A	N/A
ZB	Uniaxial	+3.0	0.41
	Radial	-1.4	0.28
	In zig-zag	-3.2	0.42
	In armchair	-2.2	0.23

In the previous sections, we reported the values of critical strains to trigger the direct-indirect band gap transition. Based on the information in Figure IV.16 (e), one can
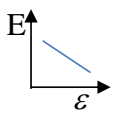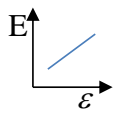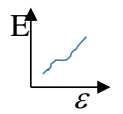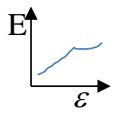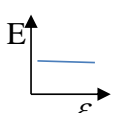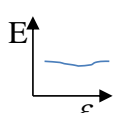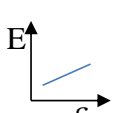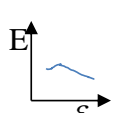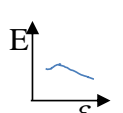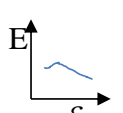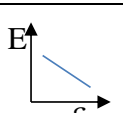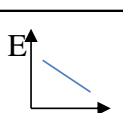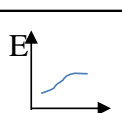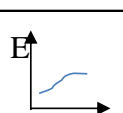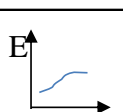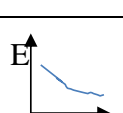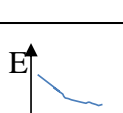
calculate the critical strain energies for the gap transition. The critical strain value and strain energy are listed in Table IV.I. It requires the smallest strain energy as 0.05 eV through applying the radial strain to convert the indirect band gap of the WZ GaAs nanowire to a direct gap. Slightly higher strain energy is needed to realize the gap transition by applying either a uniaxial compression with 0.08 eV strain energy or an expansion along the armchair direction with 0.10 eV strain energy. It demands the highest strain energy as large as 0.64 eV to trigger the band gap transition through applying strain in the zigzag direction.

For the ZB nanowire, it was found it requires less strain energy to convert the gap to direct by applying radial or strain in the armchair direction with the strain energy of 0.28 eV and 0.23 eV, respectively, compared to that of the uniaxial and zigzag strains.

In summary, the origination of the direct-indirect band gap transition in the strained 1D WZ and ZB GaAs nanowires were explored using first principles DFT calculations. It was found that (1) the WZ and ZB GaAs nanowires with a diameter of ~20 Å have an indirect gap, opposite that of their bulk counterparts; (2) the band structure of the nanowires can be significantly tuned by applying an external strain; (3) the indirect band gap of the nanowires can be tuned into a direct gap with an appropriate strain; (4) different types of strain show a different order to trigger the direct-indirect band gap transition in terms of the strain energy. It requires the smallest strain energy to convert the indirect band gap of the WZ nanowire to be direct by applying a radial strain while it needs the largest strain energy through applying strain in the zigzag direction; (5) the origination of the band gap transition in each type of strain was detailed discussed by examining the energy response of their near-gap band states with respect to strain. The

wavefunction character of the near-gap states and their energy response trends with various strains were summarized in Table IV.II.

Table IV.II. Wavefunction character for the near-gap states and schematics representing their energy variation trends with various strains.

State	Dominating orbital	Charater	Schematic of energy trend with strain			
			Uniaxial	Radial	ε in x	ε in y
A	p_z	bonding in z-direction				
B	p_x/p_y	nonbonding in z-direction				
C	s	bonding in z-direction				
D	s	antibonding in z-direction				
CB at valley	s	antibonding in z-direction				
E	p_x	bonding in x-direction				
F	p_y	bonding in y-direction				

This work was a collaboration between Xihong Peng and Andrew Copple. The author of this dissertation was responsible for most of the simulations and all but the competitive state arguments within subsection (c).

(e) Future Work. Future work within the field of III-V nanowires might include applying non-uniform uniaxial strain to the nanowires, as well as simulating larger

nanowires and altering the edge passivation of the material with different elements or groups.

Chapter V. CORE/SHELL NANOWIRES

A. Introduction

The ability to manipulate certain electronic properties of semiconductor nanostructures has produced great development in semiconductor applications. Size, surface passivation, and external strain have all been heavily implemented on semiconductor nanowires in the past.[11, 91, 92, 100, 113] However, recent work[154, 155] has shown that core/shell GaAs-InAs structures are experimentally confirmed. In addition to this, a molecular dynamics study[156] on a large number of core/shell wurtzite and zinc-blende semiconductor nanowires suggested that a core/shell ratio of about 0.5 on GaAs/InAs wurtzite nanowires would create type II semiconductor behavior. In the interest of confirming this and studying additional properties from strain and quantum confinement, this study examined both GaAs core/InAs shell nanowires, and InAs core/GaAs shell wurtzite (WZ) nanowires.

B. Methodology

First principles density functional theory (DFT)[13] calculations were carried out using Vienna *Ab-initio* Simulation Package (VASP).[50-51] The DFT local density approximation (LDA) and the projector-augmented wave potentials[102, 103] were used along with plane wave basis sets. The kinetic energy cutoff for the plane wave basis set was chosen to be 300.0 eV. The energy convergence criteria for electronic and ionic iterations were set to be 10^{-4} eV and 0.03 eV/Å, respectively. The Ga 3d, 4s, 4p, In 4d, 5s, 5p, As 4s, 4p, and H 1s electrons were treated as valence electrons. The reciprocal space of a nanowire was

sampled at 1×1×6 using Monkhorst-Pack meshes. In band structure calculations, a total of 21 K-points were included along the K-vector path from $\Gamma(0, 0, 0)$ to $X(0, 0, 0.5)$.

The WZ core shell nanowires were generated along the [0001] direction from the bulk shell material (InAs bulk WZ or GaAs bulk WZ), as seen in Figure V.1. The diameter of the WZ shell is about 30Å in diameter, and the core inside is about 12Å. The shell material has 72 of each Ga or In atom, and 72 As atoms. The core material consists of 24 In or Ga atoms, with 24 As atoms. The dangling bonds on the sides of the nanowire are fully passivated by 48 Hydrogen atoms. The Hydrogen atoms maintain to good approximation the tetrahedral bonding in the bulk wurtzite structures of InAs and GaAs.
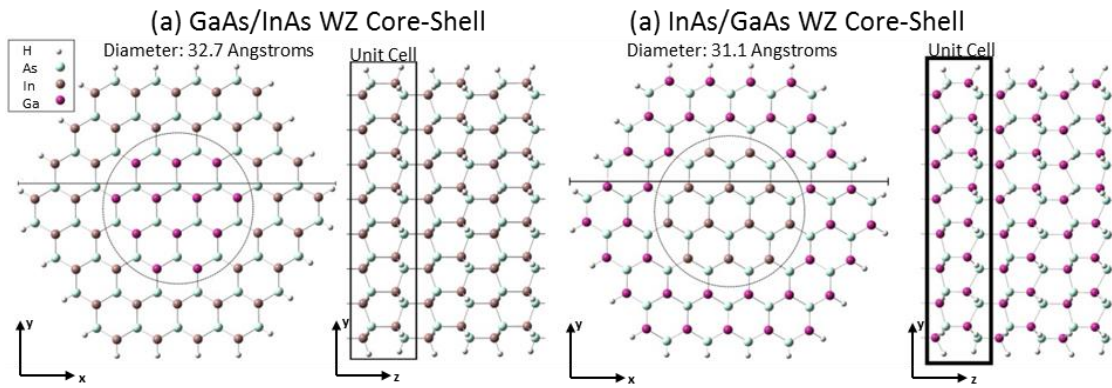
Figure V.1 Images of the studied WZ core/shell III-V nanowires. The diameter of each wire in a unit cell is shown on top. Solid rectangles in the side views indicate the unit cell, and the circle divides the core and shell of the wire in the cross-sectional view. The white, teal, tan, and purple dots represent H, As, In, and Ga, respectively.

A vacuum space greater than 15Å was used in all simulations to reduce interactions between nanowires resulting from to the periodic boundary conditions used in VASP calculations. The axial lattice constant in both core/shell nanowires is optimized through total energy minimization. The optimized lattice constant of the GaAs core/InAs shell nanowire is 6.82Å, and the constant for the InAs-GaAs nanowire is 6.59Å. Most of the structural data is presented in Table V.I below.

Table V.I A list of the studied GaAs/InAs pure and core-shell nanowires. All structures have wurtzite crystal structure. N_{Ga}, N_{In}, N_{As}, and N_H are the number of atoms of Ga, In, As, and H, respectively.

	Diameter (Å)	Lattice Constant c (Å)	N_{Ga}	N_{In}	N_{As}	N_H	Intrinsic Strain of Core (%)	Intrinsic Strain of Shell (%)
Pure GaAs	12	6.51	24	0	24	24	N/A	N/A
	20	6.51	54	0	54	36	N/A	N/A
	28	6.51	96	0	96	48	N/A	N/A
Pure InAs	13	6.97	0	24	24	24	N/A	N/A
	21	6.98	0	54	54	36	N/A	N/A
	30	6.99	0	96	96	48	N/A	N/A
InAs/GaAs	31	6.59	72	24	96	48	-5.72	1.23
GaAs/InAs	33	6.82	24	72	96	48	4.76	-2.43

After relaxing the system and studying the effects of intrinsic strain, external strain was applied to the nanowires along the uniaxial direction. In this study, positive strain indicates tensile (stretching) strain, while compressive strain is denoted by a negative strain value. When each new strain of the nanowire is generated (by displacing atoms in the axial direction accordingly, and expanding the periodic boundary condition in the axial direction), the atoms are allowed to relax again within the new boundary conditions.

The strain presented in this work exceeds the bulk limits of GaAs and InAs. However, it has been shown in previous studies[148, 157, 158] that nanowires can greatly exceed the strain capacity of their bulk equivalents.

C. Results and discussion
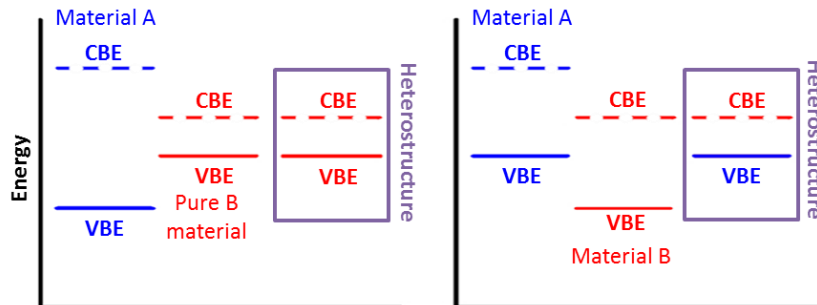
Figure V.2 Illustrated above are the classic type I and type II band structure alignments of heterostructure semiconductors. In type I, only one of the two materials directly influences the band gap, while in type II materials, both materials contribute directly to the band gap, and the band gap is typically smaller than both individual materials.

The band gap of a semiconductor is defined as the energy required to excite an electron from the valence band edge (VBE) to the conduction band edge (CBE). In a composite material, however, the edges of the band structure can be contributed from one or more materials within the semiconductor heterostructure. As seen in Figure V.2, a type I semiconductor only has one of the composite materials contribute both edges of the band structure, whereas in a type II semiconductor, two different materials within the composite structure contribute to the VBM and CBM. It is for this reason that type II semiconductors are sought out for solar cell applications, to give a greater amount of time before electrons and holes recombine by creating physical distance between the two parts of an excitation. In a type III semiconductor, the band gap is "broken" by the alignment of the composite material band gaps, which overlap in such a way to make the material more metallic than semiconductor in behavior. This is obviously not beneficial to semiconductor applications. This work intends to reveal the nature of the semiconductor interfaces between core/shell nanowires of InAs and GaAs.

Table V.II The band gaps and effective masses of all nanowires studied for this work. The band gap of the first core/shell nanowire closely matches the pure InAs 21Å nanowire, while the GaAs/InAs nanowire closely matches the band gap of the pure InAs 30Å nanowire.

System	Diameter (Å)	Bandgap (eV)	m^*_e	m^*_h
GaAs	12	1.98	0.20	0.20
	20	1.60	0.21	0.37
	30	1.32	1.20	1.00
InAs	12	1.49	1.32	5.17
	21	0.92	0.18	2.15
	30	0.65	0.14	0.82
InAs/GaAs	30	1.00	0.98	0.98
GaAs/InAs	30	0.59	0.13	0.84

Figure V.3 A cartoon side view of a core shell nanowire exhibiting intrinsic strain. Due to a lattice mismatch, the blue core creates tensile strain on the red shell, while the red shell causes compressive strain on the blue core. This matches with the first core/shell InAs/GaAs nanowire presented, and is opposite the GaAs/InAs nanowire.

The InAs core/GaAs shell nanowire is examined first. Intrinsic strain was present within the wire, as illustrated in cartoon Figure V.3. With a relaxed lattice constant of 6.59Å, and intrinsic strain on the core of -5.72% and on the shell of 1.23%, the structure

is comparable in size to a pure GaAs nanowire (6.51Å). These results are shown in Table V.I, where the difference between all nanowire sizes illustrates what pure nanowire the core/shell nanowires most closely mimic structurally. The band gap of the material was direct and about 1.00 eV and the effective mass of both the electron and hole are about $0.98m_e$, or 0.98 times the mass of an electron. Most of the electronic properties of both the core/shell nanowires and their related homogenous nanowire equivalents can be found in Table V.II above. In checking for type I or type II behavior in a simulation, the best verification comes from band gap comparisons with pure structures similar to the materials within the heterostructure. If the material exhibits behavior that matches well with pure InAs or GaAs, the core/shell nanowire demonstrates type I band alignment. If the band gap is significantly underestimated for most pure material comparisons, it is more probable that the material is type II. In the calculations, the band gap actually closely matches with that of an InAs nanowire of about 21Å in diameter, although the InAs core diameter is only 12Å. This still suggests that the core/shell nanowire has type I behavior. The most likely explanation for this matchup with a larger pure InAs nanowire is finite quantum well interaction, where it is observed that the electron cloud state exists to some degree beyond the initial finite barrier. To confirm the type I behavior, this study examines the electron cloud states of the core/shell nanowire at the VBE and CBE, illustrated in Figure V.4 below. In addition to checking where the electrons are present, it also gives insight into the nature of the state at the edge, allowing for predictions of strain behavior later in the study. With the confirmation present in Figure V.4, while physically the structure contains a quantum confined 12Å core of InAs behaving as part of a type I semiconductor, the quantum confinement better matches the next size of pure InAs

nanowires, the 21Å nanowire. At this point, the lack of type II behavior pushed this study

to move to the next core/shell nanowire for examination.
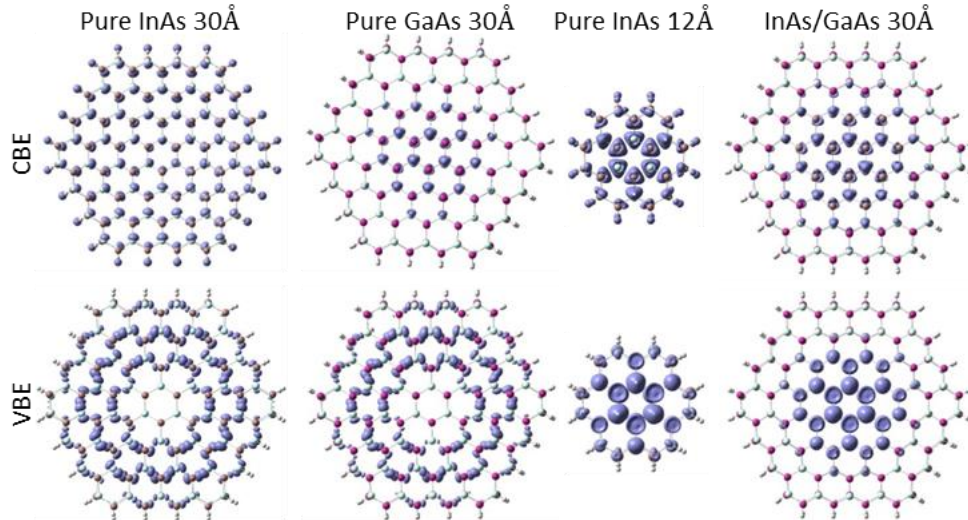
Figure V.4 The electron clouds of the pure nanowire and InAs core/GaAs shell nanowires are presented for their CBE and VBE. The CBE and VBE of the InAs 12Å nanowire seems to match most closely with the core/shell CBE and VBE. Shown also are the pure 30Å nanowires for easy differentiation between their states and the core/shell nanowire states.

The next material studied was a reverse of the previous core/shell structure; the GaAs

core/InAs shell nanowire. This nanowire had a relaxed lattice constant of 6.82Å, and thus

an intrinsic strain on the core/shell of 4.76%/-2.43%, showing that the material

unsurprisingly favored the shell material lattice constant. The direct band gap of this

core/shell nanowire was about 0.59eV, closest to the band gap of the 30Å InAs nanowire,

as seen in Table V.II. The effective mass also seemed to be in good agreement with a 30Å

InAs nanowire, with less than $0.05m_e$ difference from the pure InAs wire. However, upon

examination of the electron cloud contour plots from the VBE and CBE, the verdict

becomes less clear. Rather than observing normal type I behavior in Figure V.5, this

study suggests that the merging of the electron cloud densities in the core/shell edge

states could suggest a new type of mixing band alignment behavior, in addition to the

typical three types I, II, and III mentioned in previous texts. The merging of the electron

cloud states at the edges of the band structure imply that *both* the GaAs and InAs

contribute significantly to at least the CBE, if not the VBE as well. While it is difficult to

discern the contributing material to the electron cloud density of the VBE, it seems clear

that the CBE exhibits behavior from both the GaAs and InAs materials. Further study

should be done to examine the potential applications of such a material, as well as

confirm the existence of it experimentally.
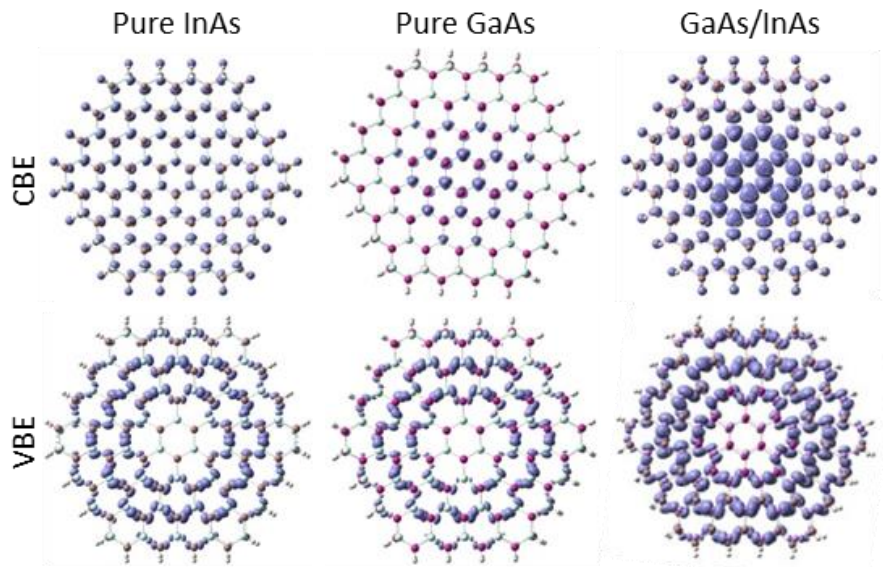
Figure V.5 The electron clouds of the pure nanowire and GaAs core/InAs shell nanowires are presented to the left. The CBE core/shell state seems to be a union of the pure GaAs and InAs nanowires, while the similarity between states in the VBE of the pure GaAs and InAs nanowires makes it difficult to detect which state or if both states are contributing to the core shell state.

After examining the relaxed states of both core/shell nanowires, external strain was

added to the system, to see if more exotic behavior could be found. The goal of this

applied strain was to examine the tunability of the band gap, and see what states arise

from the additional strain, and to see if direct/indirect transitions occurred within the

material. It would also be of interest in future studies to see if adding external strain to the

structure changes the band alignment type present within the semiconductor. Figure V.6

shows the band gap with strain of the two nanowires, showing at least one different VBE

and CBE state for each wire within the ±4% strain applied to both nanowires. No direct-indirect band gap transition was observed in this range of strain. However, significant changes in the linear behavior of the VBE and CBE with strain which coincided with significant changes in the effective mass of the electron and hole, suggested several competing states in both the VBE and CBE. The band structures of the core/shells with strain are shown in Figure V.6 to illustrate these significant shifts in effective mass and dominant states of the VBE and CBE.
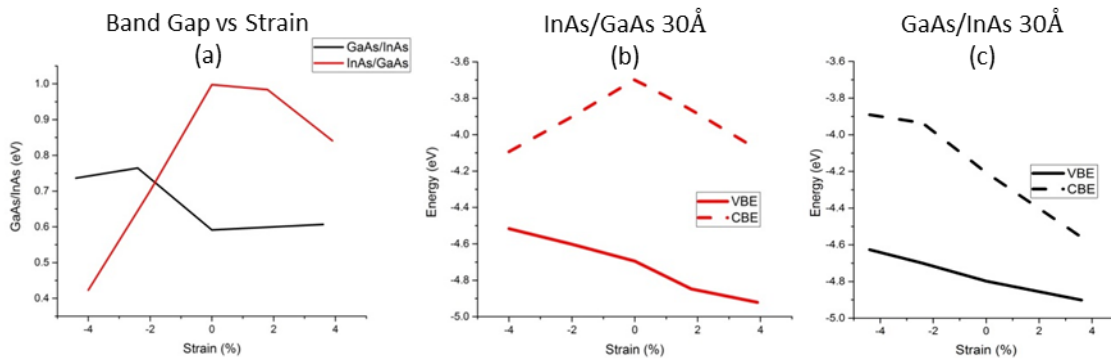
Figure V.6 These figures display the band gap values (a) and energy levels of the CBE and VBE of each core/shell nanowire (b) & (c). The InAs/GaAs nanowire displays greater band gap tunability, a result mostly from the larger shift in CBE behavior.

The dominant states of both core/shells shift with strain, as seen in Figure V.7 below. For the InAs core/GaAs shell, both the CBE and VBE shift to new electronic states with sufficient positive (tensile, <4%) strain. For the GaAs core/InAs shell, only the CBE state clearly shifts dominance at about -4.4% strain. While it appears that sufficiently larger compressive strain would also shift the VBE state of the nanowire, this study did not examine larger than -4.4% strain. Similarly, positive strain for this core/shell nanowire, and negative strain for the InAs core/GaAs shell wire did not seem to have trends suggesting a third state competing for dominance of the VBE and CBE.
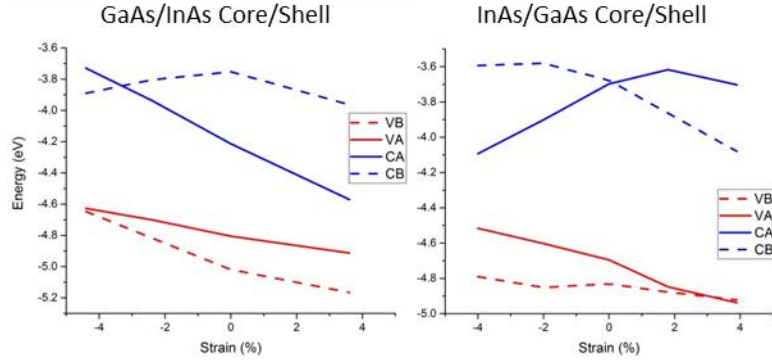
Figure V.7 The figures above show the dominant state of the CBE and VBE of each core/shell nanowire by energy. The solid line states are the dominant states without applied strain, and the dashed line states are the states that either gain dominance within the applied strain, or are most likely (in the case of V_B in GaAs/InAs) to retain dominance near the strains applied.

For the core/shell states of both nanowires, we will refer to the relaxed electron and hole states as C_A and V_A, respectively, and the states that become dominant with strain will be labelled the C_B and V_B. For the InAs core/GaAs shell nanowire, the unstrained system clearly shows type I behavior with both electron and hole edge states dominated by the core, as present in Figure V.4 (d). However, the strained electron state C_B appears to be everywhere on the structure, suggesting neither a core or shell behavior alone. Similarly, the V_B state seems to ignore the core/shell boundaries, instead creating a band of density across the (010) crystal direction. Both states are non-bonding in the z-direction, which means that the relaxation in the xy plane from applied stress in the z-direction seems to be the largest cause of change in dominance with strain. Based upon the relationship with strain (lower energy with greater compression in the xy plane), it is suggested that there is normal bonding in the xy plane direction for the C_B and V_B states of this core/shell.

For the C_B state of the GaAs core/InAs shell nanowire, the only state to gain dominance with applied strain has a very similar state to the C_A of the InAs core/GaAs shell nanowire. This state is almost entirely contained within the GaAs core of the

108

nanowire, the first state of *any* of the states to be dominant in only the GaAs material of the core/shell nanowires studied. The shift in dominance of this CBE has more to do with the increase in energy of the C_A state, than with significant change in energy of the C_B state. The C_A state appears to have an anti-bonding relationship in the z-direction of this material, creating the large dependence in energy with strain of this state.

D. Conclusion

In summary, the InAs/GaAs core/shell nanowire was found to have type I behavior with finite quantum confinement effects manipulating the band gap. The band gap was found to be about 0.98eV on the relaxed nanowire, most closely matching the 21Å pure InAs nanowire, as seen in Table V.II. It is hypothesized that the same crystal structure and sharing of As atoms between the two composite materials allows for this behavior. Additional strain to this nanowire yielded a tunability of about 0.45-0.98eV, and several different dominant states were shown to occupy the VBE and CBE at different values of strain. For the GaAs/InAs core/shell nanowire, it was found that type I-like behavior existed, with closer study suggesting a new type of mixing band alignment behavior instead. The band gap matched very closely with a pure 30Å InAs nanowire, at a value of about 0.59eV. The effective masses were also a great match to the pure InAs nanowire. The electron cloud densities of the edge states most clearly showed the possibility of this new mixing type behavior. With additional strain, the band gap of this nanowire was seen to fluctuate between the range of 0.59eV and about 0.76eV. Future studies for this work might include a third ring of III-V material around some type I materials to compare more readily to experimental nanowires that need different passivation methods. Additionally, non-uniform uniaxial strain could be considered, and different nanowire

sizes and different core/shell ratios, as well as different edge passivation should be considered. Defects within the nanowire, larger supercells along the uniaxial direction, surface defects, and band bending studies could also be simulated for these core/shell structures and single material nanowires.

REFERENCES

1   E. M. Gallo, G. Chen, M. Currie, T. McGuckin, P. Prete, N. Lovergine, B. Nabet, and J. E. Spanier, Appl. Phys. Lett. **98**, 241113–241113 (2011).

2   C. Soci, A. Zhang, X. Y. Bao, H. Kim, Y. Lo, and D. L. Wang, J. Nanosci. Nanotechnol. **10**, 1430–1449 (2010).

3   K. Tomioka, J. Motohisa, S. Hara, K. Hiruma, and T. Fukui, Nano Lett. **10**, 1639-1644 (2010).

4   D. Saxena, S. Mokkapati, P. Parkinson, N. Jiang, Q. Gao, H. H. Tan, and C. Jagadish, Nature Photon. **7**, 963-968 (2013).

5   P. D. Yang, R. X. Yan, and M. Fardy, Nano Lett. **10**, 1529-1536 (2010).

6   A. I. Hochbaum and P. D. Yang, Chem. Rev. **110**, 527-546 (2010).

7   O. Gunnarsson and R. O. Jones, Physica Scripta **21**, 3-4 (1980).

8   F. Liu, P. M. Ling, and J. Li, Phys. Rev. B **76**, 064120 (2007).

9   M. Galicka, M. Bukala, R. Buckzo, and P Kacman, J. Phys: Condens. Matter **20**, 454226 (2008).

10   P. Logan and X. H. Peng, Phys. Rev. B **80**, 115322 (2009).

11   X. H. Peng, A. Alizadeh, S. K. Kumar, and S. K. Nayak, Int. J. Appl. Mech. **1** 483-499 (2009).

12   A. Szabo and N. S. Ostlund, Modern Quantum Chemistry; Introduction to Advanced Electronic Structure Theory (Dover Publications, Inc. Mineola, New York, 1996).

13   W. Kohn and L. J. Sham, Phys. Rev. **140**, A1133-A1138 (1965).

14   P. Hohenberg and W. Kohn, Phys. Rev. **136**, B864-B871 (1964).

15   X. H. Peng, Q. Wei, and A. Copple, Phys. Rev. B **90**, 085402 (2014).

16   Huang M., Wu Y., Chandra B., Yan H., Shan Y., Heinz T. F., and Hone J., Phys. Rev. Lett. **100**, 136803 (2008).

17   K. S. Novoselov, A. K. Geim, S. V. Morozov, D. Jiang, M. I. Katsnelson, I. V. Grigorieva, S. V. Dubonos, and A. A. Firsov, Nature **438**, 197-200 (2005).

18   X. H. Peng, F. Tang, A. Copple, J. Phys.: Condens. Matter **24**, 075501 (2012).

19   K. S. Novoselov, A. K. Geim, S. V. Morozov, D. Jiang, M. I. Katsnelson, I. V. Grigorieva, S. V. Dubonos, and A. A. Firsov, Science **306**, 1379 (2004).

20   B. Wang, S. Gunther, J. Wintterlin, and M. L. Bocquet, New Journal of Physics **12**, 043041 (2010).

21   Y. Shi, K. K. Kim, A. Reina, M. Hofmann, L.-J. Li, and J. Kong ACS Nano **4**, 2689-2694 (2010).

22   G. Giovannetti, P. A. Khomyakov, G. Brocks, V. M. Karpan, J. van den Brink, and P. J. Kelly, Phys. Rev. Lett. **101**, 026803 (2008).

23   P. A. Khomyakov, G. Giovannetti, P. C. Rusu, G. Brocks, J. van den Brink, and P. J. Kelly, Phys. Rev. B **79**, 195425 (2009).

24   G. Jo, S. I. Na, S. H. O, S. Lee, T. S. Kim, G. Wang, M. Choe, W. Park, J. Yoon, D. Y. Kim, Y. H. Kahng, and T. Lee, Appl. Phys. Lett. **97**, 213301(2010).

25   M. Cox, A. Gorodetsky, B. Kim, K. S. Kim, Z. Jia, P. Kim, C. Nuckolls, and I. Kymissis, Appl. Phys. Lett. **98**, 123303 (2011)

26   G. Eda, H. E. Unalan, N. Rupesinghe, G. A. J. Amaratunga, and M. Chhowalla, Appl. Phys. Lett. **93**, 233502 (2008).

27   Y.-J. Yu, Y. Zhao, S. Ryu, L. E. Brus, K. S. Kim, and P. Kim Nano Lett. **9**, 3430 (2009).

28   A. Benayad, H.-J. Shin, H. K. Park, S.-M. Yoon, K. K. Kim, M. H. Jin, H.-K. Jeong, J. C. Lee, J.-Y. Choi, and Y. H. Lee, Chemical Physics Letters **475**, 91-95 (2009).

29   Y. Murata, E. Starodub, B. B. Kappes, C. V. Ciobanu, N. C. Bartelt, K. F. McCarty, and S. Kodambaka, Appl. Phys. Lett. **97**, 143114 (2010).

30   J. Park, W. H. Lee, S. Huh, S. H. Sim, S. B. Kim, K. Cho, B. H. Hong, and K. S. Kim, The Journal of Physical Chemistry Letters **2**, 841 (2011).

31   Y. Yi, W. M. Cho, Y. H. Kim, J. W. Kim, and S. J. Kang S J, Appl. Phys. Lett. **98**, 013505 (2011).

32   Y. Q. Cai, A. H. Zhang, Y. P. Feng, C. Zhang, H. F. Teoh, and G. W. Ho, J. Chem. Phys. **131** 224701 (2009).

33 Y. D. Wang, N. Lu, H. B. Xu, G. Shi, M. J. Xu, X. W. Lin, H. B. Li, W. T. Wang, D. P. Qi, Y. Q. Lu, and L. F. Chi, Nano Res. **3**, 520 (2010).

34 K. S. Kim, Y. Zhao, H. Jang, S. Y. Lee, J. M. Kim, K. S. Kim, J.-H. Ahn, P. Kim, J.-Y. Choi, and B. H. Hong, Nature **457**, 706 (2009).

35 S.-M. Choi, S.-H. Jhi, and Y.-W. Son, Phys. Rev. B **81**, 081407 (2010).

36 G. Gui, J. Li, and J. X. Zhong, Phys. Rev. B **78**, 075435 (2008).

37 Y. Li, X. W. Jiang, Z. F. Liu, and Z. R. Liu, Nano Res. **3**, 545 (2010).

38 Y. Lu and J. Guo, 2010 Nano Res. **3**, 189 (2010).

39 V. M. Pereira and A. H. C. Neto, Phys. Rev. Lett. **103**, 046801 (2009).

40 L. Sun, Q. X. Li, H. Ren, H. B. Su, Q. W. Shi, and J. L. Yang, J. Chem. Phys. **129**, 074704 (2008).

41 X. H. Peng and S. Velasquez, Appl. Phys. Lett. **98** 023112 (2011).

42 M. Neek-Amal and F. M. Peeters, J. Phy. Condens. Matter **23**, 243201 (2011).

43 D. Yu and F. Liu, Nano Lett. **7**, 3046 (2007).

44 N. Jung, A. C. Crowther, N. Kim, P. Kim, and L. Brus, ACS Nano **4**, 7005 (2010).

45 M. I. Rojas and E. P. M. Leiva, Phys. Rev. B **76**, 155415 (2007).

46 V. M. Bermudez and J. T. Robinson, Langmuir **27**, 11026 (2011).

47 O. Leenaerts, H. Peelaers, A. D. Hernández-Nieves, B. Partoens and F. M. Peeters, Phys. Rev. B **82**, 195436 (2010).

48 J. O. Sofo, A. S. Chaudhari and G. D. Barber, Phys. Rev. B **75**, 153401 (2007).

49 D. W. Boukhvalov and M. I. Katsnelson, J. Phys. Condens. Matter **21**, 344205 (2009).

50 G. Kresse and J. Furthmuller, Comput. Mater. Sci. **6**, 15 (1996).

51 G. Kresse and J. Furthmuller, Phys. Rev. B **54**, 11169 (1996).

52 J. P. Perdew, J. A. Chevary, S. H. Vosko, K. A. Jackson, M. R. Pederson, D. J. Singh, and C. Fiolhais, Phys. Rev. B **46**, 6671 (1992).

[53] C. Oshima and A. Nagashima, J. Phys. Condens. Matter **9**, 1 (1997).

[54] D. Vanderbilt, Phys. Rev. B **41**, 7892 (1990).

[55] H. J. Monkhorst and J. D. Pack, Phys. Rev. B **13,** 5188 (1976).

[56] K. Nakada, M. Fujita, G. Dresselhaus, and M. S. Dresselhaus, Phys. Rev. B **54**, 17954 (1996).

[57] Y. W. Son, M. L. Cohen, and S. G. Louie, Phys. Rev. Lett. **97**, 216803 (2006).

[58] B. Shan and K. Cho, Phys. Rev. Lett. **94**, 236602 (2005).

[59] H. R. Gong, Y. Nishi, and K. Cho, Appl. Phys. Lett. **91**, 242105 (2007).

[60] P. S. Bagus, F. Illas, G. Pacchioni, and F. Parmigiani, J. Electron Spectrosc. Relat. Phenom. **100**, 215 (1999).

[61] B. Richter, H. Kuhlenbeck, H. J. Freund, and P. S. Bagus, Phys. Rev. Lett. **93**, 026805 (2004).

[62] R. W. Grant, J. R. Waldrop, E. A. Kraut, and W. A. Harrison, J. Vac. Sci. Technol., B **8**, 736 (1990).

[63] O. T. Hofmann, D. A. Egger, and E. Zojer, Nano Lett. **10**, 4369 (2010).

[64] P. C. Rusu, G. Giovannetti, C. Weijtens, R. Coehoorn, and G. Brocks, J. Phys. Chem. C **113**, 9974 (2009).

[65] X. Crispin, V. Geskin, A. Crispin, J. Cornil, R. Lazzaroni, W. R. Salaneck, and J.-L. Brédas, JACS **124**, 8131 (2002).

[66] C. C. Fulton, G. Lucovsky, and R. J. Nemanich, Appl. Phys. Lett. **84**, 580 (2004).

[67] Likai Li, Yijun Yu, Guo Jun Ye, Qingqin Ge, Xuedong Ou, Hua Wu, Donglai Feng, Xian Hui Chen and Yuanbo Zhang, Nat Nanotechnol **9**, 372-377 (2014).

[68] H. Liu, A. T. Neal, Z. Zhu, Z. Luo, X. Xu, D. Tománek and P. D. Ye, Acs Nano **8** (4), 4033-4041 (2014).

[69] E. S. Reich, Nature **506**, 19 (2014).

[70] F. Xia, H. Wang and Y. and Jia, arXiv:1402.0270 (2014).

71 Y. B. Zhang, Y. W. Tan, H. L. Stormer and P. Kim, Nature **438** (7065), 201-204 (2005).

72 B. Radisavljevic, A. Radenovic, J. Brivio, V. Giacometti and A. Kis, Nat Nanotechnol **6** (3), 147-150 (2011).

73 A. S. Rodin, A. Carvalho and A. H. Castro Neto, Phys. Rev. Lett. **112**, 176801 (2014).

74 Y. Takao and A. Morita, Physica B & C **105** (1-3), 93-98 (1981).

75 Vy Tran, Ryan Soklaski, Yufeng Liang, and Li Yang, Phys. Rev. B **89** (23), 235319 (2014).

76 R. S. Jacobsen, K. N. Andersen, P. I. Borel, J. Fage-Pedersen, L. H. Frandsen, O. Hansen, M. Kristensen, A. V. Lavrinenko, G. Moulin, H. Ou, C. Peucheret, B. Zsigri and A. Bjarklev, Nature **441** (7090), 199-202 (2006).

77 M. R. Falvo, G. J. Clary, R. M. Taylor, V. Chi, F. P. Brooks, S. Washburn and R. Superfine, Nature **389** (6651), 582-584 (1997).

78 A. Thean and J. P. Leburton, Applied Physics Letters **79** (7), 1030-1032 (2001).

79 X. L. Wu and F. S. Xue, Applied Physics Letters **84** (15), 2808-2810 (2004).

80 L. Seravalli, M. Minelli, P. Frigeri, P. Allegri, V. Avanzini and S. Franchi, Applied Physics Letters **82** (14), 2341-2343 (2003).

81 S. Mazzucato, D. Nardin, M. Capizzi, A. Polimeni, A. Frova, L. Seravalli and S. Franchi, Materials Science and Engineering: C **25** (5–8), 830-834 (2005).

82 Y. G. Wang, Q. L. Zhang, T. H. Wang, W. Han and S. X. Zhou, Journal of Physics D: Applied Physics **44** (12), 125301 (2011).

83 A. I. Hochbaum and P. D. Yang, Chemical Reviews **110** (1), 527-546 (2010).

84 X. H. Peng and P. Logan, Applied Physics Letters **96** (14), 143119 (2010).

85 K. S. Kim, Y. Zhao, H. Jang, S. Y. Lee, J. M. Kim, K. S. Kim, J.-H. Ahn, P. Kim, J.-Y. Choi and B. H. Hong, Nature **457** (7230), 706-710 (2009).

86 C. Lee, X. D. Wei, J. W. Kysar and J. Hone, Science **321** (5887), 385-388 (2008).

87 A. Castellanos-Gomez, M. Poot, G. A. Steele, H. S. J. van der Zant, N. Agrait and G. Rubio-Bollinger, Nanoscale Research Letters **7**, 1-4 (2012).

88 Q. Wei and X. Peng, Appl. Phys. Lett. **104**, 251915 (2014).

89 Ruixiang Fei and Li Yang, Nano Lett. **14** (5), 2884-2889 (2014).

90 Jingsi Qiao, Xianghua Kong, Zhi-Xin Hu, Feng Yang and Wei Ji, Nature Communications **5**, 4475 (2014).

91 A. Copple, N. Ralston and X. Peng, Applied Physics Letters **100** (19), 193108-193104 (2012).

92 X. Peng and A. Copple, Physical Review B **87** (11), 115308 (2013).

93 G. Signorello, E. Lörtscher, P. A. Khomyakov, S. Karg, D. L. Dheeraj, B. Gotsmann, H. Weman and H. Riel, Nature Communications **5**, 3655 (2014).

94 X. H. Peng, A. Alizadeh, N. Bhate, K. K. Varanasi, S. K. Kumar and S. K. Nayak, Journal of Physics: Condensed Matter **19** (26), 266212 (2007).

95 X. H. Peng, S. Ganti, A. Alizadeh, P. Sharma, S. K. Kumar and S. K. Nayak, Phys. Rev. B **74** (3), 035339-035343 (2006).

96 S. Sreekala, X. H. Peng, P. M. Ajayan and S. K. Nayak, Physical Review B **77** (15), 155434 (2008).

97 P. Logan and X. H. Peng, Physical Review B **80** (11), 115322 (2009).

98 X. H. Peng, A. Alizadeh, S. K. Kumar and S. K. Nayak, Int. J. of Applied Mechanics **1**, 483-499 (2009).

99 X. H. Peng and S. Velasquez, Applied Physics Letters **98** (2), 023112 (2011).

100 X.-H. Peng, F. Tang and P. Logan, Journal of Physics: Condensed Matter **23** (11), 115502 (2011).

101 J. P. Perdew, K. Burke and M. Ernzerhof, Physical Review Letters **77** (18), 3865-3868 (1996).

102 P. E. Blochl, Physical Review B **50** (24), 17953-17979 (1994).

103 G. Kresse and D. Joubert, Physical Review B **59** (3), 1758-1775 (1999).

104 J. Heyd, G. E. Scuseria and M. Ernzerhof, The Journal of Chemical Physics **118** (18), 8207-8215 (2003).

105 J. Heyd, G. E. Scuseria and M. Ernzerhof, The Journal of Chemical Physics **124** (21), 219906-219901 (2006).

[106] Allan Brown and Stig Rundqvist, Acta Cryst. **19**, 684 (1965).

[107] J. B. Hudson, Surface Science. (John Wiley & Sons, Inc., New York, 1998).

[108] D. Roundy and M. L. Cohen, Physical Review B **64** (21), 212103 (2001).

[109] W. Luo, D. Roundy, M. L. Cohen and J. W. Morris, Physical Review B **66** (9), 094110 (2002).

[110] M. Zhou, Z. Liu, Z. F. Wang, Z. Q. Bai, Y. P. Feng, M. G. Lagally and F. Liu, Physical Review Letters **111** (24) (2013).

[111] S. Huang and L. Yang, Applied Physics Letters **98** (9), (2011).

[112] K.-H. Hong, J.-K. Yoon and P.-R. Cha, Applied Surface Science **253** (5), 2776-2784 (2006).

[113] K.-H. Hong, J. Kim, S.-H. Lee and J. K. Shin, Nano Lett **8** (5), 1335-1340 (2008).

[114] R. M. White, Quantum Theory of Magnetism, 3rd ed. (Springer, New York, 2006).

[115] J. Dai and X. C. Zeng, J. Phys. Chem. Lett. **5** (7), 1289-1293 (2014).

[116] H. Guo, N. Lu, J. Dai, X. Wu and X. C. Zeng, J Phys Chem C **118** (25), 14051-14059 (2014).

[117] W. Lu, H. Nan, J. Hong, Y. Chen, C. Zhu, Z. Liang, X. Ma, Z. Ni, C. Jin and Z. Zhang, Nano Research **7** (6), 853-859 (2014).

[118] V. Tran and L. Yang, Physics Review B **89**, 145407 (2014).

[119] A. Maity, A. Singh and P. Sen, arXiv:1404.2469 (2014).

[120] A. Carvalho, A. S. Rodin and A. H. C. Neto, EPL **108** (4), 47005 (2014).

[121] H. Y. Lv, W. J. Lu, D. F. Shao and Y. P. Sun, arXiv:1404.5171 (2014).

[122] Michele Buscema, Dirk J. Groenendijk, Sofya I. Blanter, Gary A. Steele, Herre S.J. van der Zant and A. Castellanos-Gomez, Nano Lett. **14** (6), 3347-3352 (2014).

[123] X. H. Peng and Q. Wei, Mater. Res. Express **1**, 045041 (2014).

[124] A. De and C. E. Pryor, Phys. Rev. B **81** (15), 155210 (2010).

[125] V. Pankoke, P. Kratzer and S. Sakong, Phys. Rev. B **84** (7), 075455 (2011).

[126] J. Bolinsson, Ph.D. Dissertation, Lund University, 2010.

[127] M. A. Khayer and R. K. Lake, IEEE Transactions on Electron Devices **55** (11), 2939-2945 (2008).

[128] Z. Mi and Y.-L. Chang, Journal of Nanophotonics **3**, 031602-031619 (2009).

[129] J. A. Czaban, D. A. Thompson and R. R. LaPierre, Nano Lett **9** (1), 148-154 (2008).

[130] F. Patolsky, G. Zheng and C. M. Lieber, Nanomedicine **1** (1), 51-65 (2006).

[131] F. Glas, J.-C. Harmand and G. Patriarche, Phys. Rev. Lett. **99** (14), 146101 (2007).

[132] H. Shtrikman, R. Popovitz-Biro, A. Kretinin and M. Heiblum, Nano Lett **9** (1), 215-219 (2008).

[133] M. Koguchi, H. Kakibayashi, M. Yazawa, K. Hiruma and T. Katsuyama, Jpn. J. Appl. Phys. **31** (7), 2061-2065 (1992).

[134] P. Caroff, J. Bolinsson and J. Johansson, Selected Topics in Quantum Electronics, IEEE J. Sel. Top. Quantum Electron. **17** (4), 829-846 (2011).

[135] M. P. Persson and H. Q. Xu, Appl. Phys. Lett. **81** (7), 1309-1311 (2002).

[136] S. Cahangirov and S. Ciraci, Phys. Rev. B **79** (16), 165118 (2009).

[137] T. Cheiwchanchamnangij and W. R. L. Lambrecht, Phys. Rev. B **84** (3), 035203 (2011).

[138] X.-H. Peng, F. Tang and P. Logan, in Nanowires - Fundamental Research, edited by A. Hashim (InTech, 2011).

[139] P. W. Leu, A. Svizhenko and K. Cho, Phys. Rev. B **77** (23), 235305 (2008).

[140] Z. G. Wu, J. B. Neaton and J. C. Grossman, Nano Lett **9** (6), 2418-2422 (2009).

[141] N. Tajik, Z. Peng, P. Kuyanov and R. R. LaPierre, Nanotechnology **22** (22), 225402 (2011).

[142] L. Voon, Y. Zhang, B. Lassen, M. Willatzen, Q. H. Xiong and P. C. Eklund, Journal of Nanoscience and Nanotechnology **8** (1), 1-26 (2008).

[143] T. Tezuka, S. Sugiyama, T. Mizuno, M. Suzuki and S.-i. Takagi, Jpn. J. Appl. Phys. **40**, 2866-2874 (2001).

[144] T. Ghani, M. Armstrong, C. Auth, M. Bost, P. Charvat, G. Glass, T. Hoffmann, K. Johnson, C. Kenyon, J. Klaus, B. McIntyre, K. Mistry, A. Murthy, J. Sandford, M. Silberstein, S. Sivakumar, P. Smith, K. Zawadzki, S. Thompson and M. Bohr, in Electron Devices Meeting, 2003. IEDM '03 Technical Digest. IEEE International (Hillsboro, OR, USA 2003), pp. 11.16.11 - 11.16.13 .

[145] L. Z. Kou, C. Tang, Y. Zhang, T. Heine, C. F. Chen and T. Frauenheim, Journal of Physical Chemistry Letters **3** (20), 2934-2941 (2012).

[146] J. Feng, X. F. Qian, C. W. Huang and J. Li, Nat. Photonics **6** (12), 865-871 (2012).

[147] V. Pankoke, P. Kratzer and S. Sakong, Phys. Rev. B **84** (7), 075455 (2011).

[148] Y. B. Wang, L. F. Wang, H. J. Joyce, Q. A. Gao, X. Z. Liao, Y. W. Mai, H. H. Tan, J. Zou, S. P. Ringer, H. J. Gao and C. Jagadish, Adv. Mater. **23** (11), 1356-1360 (2011).

[149] L. Hedin, Phys. Rev. **139** (3A), A796-A823 (1965).

[150] S. V. Faleev, M. van Schilfgaarde and T. Kotani, Phys. Rev. Lett. **93** (12), 126406-126409 (2004).

[151] F. Bruneval, F. Sottile, V. Olevano, R. Del Sole and L. Reining, Phys. Rev. Lett. **94** (18), 186402-186405 (2005).

[152] A. Puzder, A. J. Williamson, J. C. Grossman and G. Galli, Phys. Rev. Lett. **88** (9), 097401-097404 (2002).

[153] X. Zhao, C. M. Wei, L. Yang and M. Y. Chou, Phys. Rev. Lett. **92** (23), 236805-236808 (2004).

[154] R. Popovitz-Biro, A. Kretinin, P. Von Huth, and H. Shtrikman, Cryst. Growth Des. **11** (9), 3858-3865 (2011).

[155] T. Rieger, M. Luysberg, T. Schapers, D. Grutzmacher, and M. I. Lepsa, Nano Lett. **12** (11), 5559-5564 (2012).

[156] M.-E. Pistol and C. E. Pryor, Phys. Rev. B. **78** (11), 115319 (2008).

[157] M. J. Gordon, T. Baron, F. Dhalluin, P. Gentile, and P. Ferret, Nano Lett. **9** (2), 525-529 (2009).

[158] X. D. Han, K. Zheng, Y. F. Zhang, X. N. Zhang, Z. Zhang, Z. L. Wang, Adv. Mater. **19** (16), 2112 (2007).

[159] X.-H. Peng, A. Copple, and Q. Wei, J. Appl. Phys. **116**, 144301 (2014).